

**A Measurement of the Leptonic Asymmetry
in Top-Quark Pairs Produced in $p\bar{p}$ Collisions
at $\sqrt{s} = 1.96$ TeV**

by

Ryan C. Edgar

A dissertation submitted in partial fulfillment
of the requirements for the degree of
Doctor of Philosophy
(Physics)
in The University of Michigan
2014

Doctoral Committee:

Professor Dante E. Amide, Chair
Professor Ronald M. Gilgenbach
Professor Roberto D. Merlin
Associate Professor Aaron T. Pierce
Assistant Professor Thomas A. Schwarz

© Ryan C. Edgar 2014

All Rights Reserved

To my grandfathers, George Rubin and William Edgar. Wish you were here.



ACKNOWLEDGEMENTS

Just like anyone else, I wouldn't have made it this far without the love and support of a great many family members, friends, and colleagues. The last few years have been pretty frenetic – thanks for sticking with me. I won't name names. You all know who you are.

TABLE OF CONTENTS

DEDICATION	ii
ACKNOWLEDGEMENTS	iii
LIST OF FIGURES	vii
LIST OF TABLES	xii
LIST OF APPENDICES	xv
ABSTRACT	xvi
CHAPTER	
I. Introduction; the Standard Model and the Top Quark	1
1.1 The Standard Model	3
1.2 Properties of the Top Quark	9
1.2.1 Production	9
1.2.2 Mass, Width, and Lifetime	11
1.2.3 Decay	12
1.3 Top Quark Production Asymmetry	15
1.4 The Lepton Asymmetry	19
II. Experimental Apparatus	22
2.1 The Fermilab Accelerator Complex	23
2.1.1 Proton Source and Preaccelerator	23
2.1.2 Linac	24
2.1.3 Booster and Main Injector	25
2.1.4 Antiproton Source, Debuncher, Accumulator	26
2.1.5 Recycler	27
2.1.6 Tevatron	28
2.2 The Collider Detector at Fermilab	29
2.2.1 Coordinate System	30

2.2.2	Tracking	32
2.2.3	Calorimetry	41
2.2.4	Muon Detection	45
2.2.5	Triggers	48
III. Offline Reconstruction and Object Identification		54
3.1	Data Handling	55
3.2	Track Reconstruction	55
3.3	Vertexing	57
3.4	Lepton Identification	59
3.5	Jets	64
3.5.1	Calorimeter Clustering	65
3.5.2	Jet Energy Scales	66
3.5.3	B -Tagging	69
3.6	E_T^{miss} and H_T	76
IV. Signal Selection and Modelling		78
4.1	Definition of the Signal Region	79
4.1.1	W + Jets Selection	80
4.1.2	Signal Region	82
4.2	Background Components	83
4.3	Top-Pair Production Models	85
4.4	Sample Composition	90
4.4.1	Signal Region: Yields and Validation	93
4.5	Asymmetries of the Backgrounds	97
4.5.1	Control Sample I: W +1 Jet	99
4.5.2	Control Sample II: Zero Tag	103
V. The Leptonic Asymmetry in Top-Quark Pairs		106
5.1	Methodology	107
5.1.1	Rapidity Decomposition	107
5.1.2	Bin-by-bin Acceptance Corrections	108
5.1.3	Extrapolation Procedure	110
5.1.4	Summary of the Correction Procedure	113
5.1.5	Validation	114
5.2	Expected Value of A_{FB}^ℓ	115
5.3	Measurement of A_{FB}^ℓ	116
5.3.1	Central Value	116
5.3.2	Uncertainties	119
5.3.3	Consistency Checks	121
VI. Conclusions		123

APPENDICES	124
REFERENCES	137

LIST OF FIGURES

Figure

1.1	The chapter headpiece.	2
1.2	The known fundamental particles of the Standard Model [1]. Three generations of spin-1/2 quarks and leptons interact via the exchange of spin-1 vector gauge bosons. The spin-0 Higgs provides mass to the W and Z , the quarks, and the charged leptons.	3
1.3	The interactions between the Standard Model fermions and bosons [2].	5
1.4	Charged currents involved in the weak decays of quarks. An up-type quark (charge $+2/3$) can decay to a W^+ (charge $+1$) and a lighter down-type quark (charge $-1/3$). Similarly, a down-type quark can decay to a lighter up-type quark via the emission of a W^- . The colors correspond to the probability of a particular decay, and encode the magnitudes of the CKM matrix elements [3].	8
1.5	Leading-order diagrams contributing to top-pair production. Quark-antiquark annihilation (Fig. (a)) contributes 85% of the Tevatron cross-section, while gluon-gluon fusion (Fig. (b), (c), (d)) contributes the remaining 15%. At the Large Hadron Collider, these proportions are approximately reversed.	9
1.6	Summary of LHC and Tevatron measurements of the top-pair production cross-section as a function of the centre-of-mass energy \sqrt{s} . Shown also are the NNLO QCD calculations with NNLL resummation. [4].	11
1.7	The production angle θ^* and the frame-invariant rapidity difference Δy of the $t\bar{t}$ system.	15
1.8	Leading-order diagrams contributing to the top-pair production asymmetry. Figures (a) and (b) interfere at low $p_T^{t\bar{t}}$ to produce a positive asymmetry. Figures (c) and (d) interfere at larger $p_T^{t\bar{t}}$ to produce a negative asymmetry. The dotted lines indicate the color flow in each diagram.	16
1.9	Color flow and QCD radiation in (a) forward events and (b) backward events [5].	16
1.10	The top-quark production asymmetry $A_{\text{FB}}^{\Delta y}$ as a function of $p_T^{t\bar{t}}$, the transverse momentum of the $t\bar{t}$ system. The dependence is shown for several different generators.	17

1.11	A top-quark pair produced at rest with a right-handed polarization in the beamline basis. In Fig. (a), the anti-top quark decays leptonically, sending more negative leptons into the backward region. In Fig. (b), the top quark decays leptonically and preferentially sends positive leptons into the forward region. This produces a forward-backward asymmetry in the charge-weighted lepton rapidity.	20
2.1	The chapter headpiece.	22
2.2	The Fermilab accelerator complex. Protons and antiprotons are accelerated through a sequence of several accelerators, eventually reaching 980 GeV per beam. The protons/antiprotons are then stored as countercirculating beams in the Tevatron, intersecting within the CDF and D0 detectors (location B0 and D0, respectively) [6].	23
2.3	An elevation view of the CDF-II detector, showing the physical arrangement of tracking and calorimetry systems, the solenoidal magnet, shielding, and muon detection [7].	29
2.4	The CDF coordinate system as described in Section 2.2.1	30
2.5	The relationship between the pseudorapidity η and the azimuthal angle θ . The functional dependence of $\theta = \theta(\eta)$ is shown in a, while the rays corresponding to several values of η are illustrated in b	31
2.6	The CDF-II tracking volume. Shown are the superconducting solenoid, Central Outer Tracker, Intermediate Silicon Layers, and Secondary Vertex Detection. Layer 00 is not shown [8].	33
2.7	The east endplate of the Central Outer Tracker. The long slots locate the gold-on-mylar cathode sheets which separate adjacent cells, while the short, keyed slots locate the wire plane of an individual cell [8].	35
2.8	The layout of the CDF silicon tracking system. Layer 00 (L00) is closest to the beampipe, surrounded by the SVX layers and the associated Port Cards. Outside both of these are the Intermediate Silicon Layers (ISL) and the ISL Port Cards. Note that the z -axis is compressed for convenient illustration [9].	37
2.9	The SVX-II bulkhead design. The bulkhead is constructed from precision-machined beryllium, and locates 60 silicon microstrip ‘ladders’ arranged in 12 wedges and 5 layers [8].	39
2.10	The CDF calorimeters. The CEM and PEM calorimeters measure the energy of electromagnetically-interacting particles, while CHA, PHA and WHA measure the energy of strongly-interacting particles [10].	42
2.11	The CDF triggering architecture. Three trigger levels successively reduce the event rate from the 1.7 MHz bunch crossing rate down to the 150 Hz at which events can be written to tape [8, 11]. Shown here are the Level-1 and Level-2 triggering systems. Level-3, which is implemented entirely in software, is not displayed.	49
3.1	The chapter headpiece.	54

3.2	The parametrization used at CDF to describe the helical paths of particles within the inner tracking system. Paths for both positively-charged ($C > 0$, red) and negatively-charged ($C < 0$, blue) are shown, assuming that both have the same origin and opposite initial momenta. The dashed line shows the extrapolated helix common to both. Figure a shows the projection of the helix to the r - ϕ plane, and b to r - z	56
3.3	An illustration of the interactions of different particle types with the major subsystems of the CDF-II detector. The characteristic patterns of interaction allow different particle types to be distinguished in the data [12].	60
3.4	Dijet balance corrections to the jet energy scales. Shown is the ratio $\beta_{\text{dijet}} = p_{\text{T}}^{\text{probe}}/p_{\text{T}}^{\text{trigger}}$ as a function of η , in four separate ranges of the jet p_{T} . This is used to calibrate the η -dependent calorimeter response to that of the central region ($0.2 \leq \eta \leq 0.6$) [13].	68
3.5	A depiction of the parameter L2D used in SECVTX b -tagging. The jet cone is indicated by the shaded wedge, and the jet axis by the dashed line. The displacement vector between the primary and secondary vertices (heavy solid line) is projected onto the jet axis, and the length of the projection is the parameter L2D (heavy dashed line). Figure a shows a ‘positive tag’ ($L2D > 0$) and b shows a ‘negative tag’ ($L2D < 0$).	71
4.1	The chapter headpiece.	78
4.2	A top-quark pair in the ℓ +jets channel. In this illustration, the top (t) decays into a lepton, a neutrino, and a bottom quark which produces a b jet. The anti-top (\bar{t}) produces a second b jet and two light jets.	79
4.3	Divisions of W +jets and their assignment to the signal and control regions. The W +jets sample is separated by trigger (outer column) as well as by the number of tight jets (row) and the number of tagged tight jets (inner column). Gray, crosshatched regions do not exist or are unavailable. Note that additional requirements are imposed on these regions as per Table 4.1.	81
4.4	The distribution of simulated $t\bar{t}$ events as a function of qy_{ℓ} at the production level (Fig. (a)) for several benchmark models. The corresponding asymmetries in each bin are shown in Figure (b). The vertical lines at $ qy_{\ell} = 1.25$ indicate the limits of the lepton acceptance.	87
4.5	Several production-level distributions of simulated $t\bar{t}$ events. Figure (a) shows the distribution of the lepton rapidity y_{ℓ} without charge weighting. Figures b and d respectively show the distribution of the transverse momentum of the lepton, p_{T}^{ℓ} , and the invariant mass of the $t\bar{t}$ system, $M_{t\bar{t}}$. Figure c) shows the rapidity distributions of the leptonically-decaying top quark. All distributions indicate good agreement between the different models.	89
4.6	The transverse energies of the first four jets, where the jets are ranked by descending order in E_{T} . Figure (a) shows the E_{T} of the first jet, (b) the second, (c) the third, and (d) the fourth. In all cases the distribution of the observed CDF data agrees well with the prediction.	95

4.7	Additional validation histograms. Figure (a) and (b) show the distributions of the transverse momentum p_T^ℓ , p_T^ℓ of the lepton and its vertex-corrected pseudorapidity η^ℓ . Figure (c) shows E_T^{miss} , and (d) the distribution of H_T . In both the leptonic variables (p_T^ℓ , η^ℓ) and the macroscopic variables (E_T^{miss} , H_T), good agreement is seen between the measured CDF data and prediction.	96
4.8	The distribution of qy_ℓ for the predicted backgrounds.	97
4.9	Production mechanisms for a positive W boson in association with one jet. Contributions initiated by ug are shown in Figure (a) and (b); analogous processes exist for the other light-quark flavors. Alternatively, a jet may be produced from initial-state radiation (d), (c). Tree-level production of larger jet multiplicities occurs through additional initial- and final-state radiation and gluon-splitting.	99
4.10	Plots of the $W+1$ jet control region. Figure (a) shows the observed and predicted distributions of p_T^ℓ , and Figure (c) of the vertex-corrected η_ℓ . Figure (b) and (d) show the dependence of A_{FB}^ℓ on the lepton p_T^ℓ and η_ℓ respectively. The colored bands around the predicted A_{FB}^ℓ indicate the $\pm 1\sigma$ uncertainties on the prediction, which are dominated by uncertainties on the heavy-flavor fraction. In all cases the observed CDF data agrees with the prediction well within uncertainties. . . .	102
4.11	Comparisons of measured and predicted distributions in the zero-tag control region. Figure (a) shows qy_ℓ , the charge-weighted lepton rapidity. Figure (b) shows the transverse momentum of the lepton, p_T^ℓ	105
5.1	The chapter headpiece.	106
5.2	The symmetric part (a) and asymmetric part (b) of the production-level distribution of qy_ℓ for the benchmark models. Shown also are the best fits to Eq.(5.11). The vertical lines at $ qy_\ell = 1.25$ indicate the limits of the lepton acceptance.	112
5.3	A graphical representation of the correction procedure. Blue and red boxes represent distribution derived from data and simulation, respectively. Un-filled boxes represent operations, and green boxes represent observable asymmetries at different correction levels.	114
5.4	Several key distributions in the signal region. Figure (a) shows the distribution of qy_ℓ in the measured data. Figure (b) shows the same distribution after subtracting the most probable background contribution in each bin. Figure (c) and (d) show the symmetry part $S(qy_\ell)$ and the qy_ℓ -dependent asymmetry $A_{\text{FB}}^\ell(qy_\ell)$ after background-subtraction.	118
5.5	The binned asymmetry $A_{\text{FB}}^\ell(qy_\ell)$ after correcting for acceptance, compared to the NLO QCD prediction of POWHEG. The best fit to Eq. (5.11) for each is shown as the smooth curve of the same color. The dark (light) gray bands indicate the statistical (total) uncertainty on the fit curve to the data.	119
6.1	The chapter headpiece.	123

A.1	Several key distributions, reproduced using only events that contain a positive lepton. Shown are qy_ℓ (a) and p_T^ℓ (b) before background subtraction, along with $S(qy_\ell)$ (c) and $A_{\text{FB}}^\ell(qy_\ell)$ (d) after background-subtraction.	126
A.2	Several key distributions, reproduced using only events that contain a negative lepton. Shown are qy_ℓ (a) and p_T^ℓ (b) before background subtraction, along with $S(qy_\ell)$ (c) and $A_{\text{FB}}^\ell(qy_\ell)$ (d) after background-subtraction.	127
A.3	Several key distributions, reproduced using only events that contain an electron. Shown are qy_ℓ (a) and p_T^ℓ (b) before background subtraction, along with $S(qy_\ell)$ (c) and $A_{\text{FB}}^\ell(qy_\ell)$ (d) after background-subtraction.	128
A.4	Several key distributions, reproduced using only events that contain a muon. Shown are qy_ℓ (a) and p_T^ℓ (b) before background subtraction, along with $S(qy_\ell)$ (c) and $A_{\text{FB}}^\ell(qy_\ell)$ (d) after background-subtraction.	129
A.5	A comparison of the acceptance-correct qy_ℓ fits between several subsamples of the signal region. Figures (a) and (b) show the fit for events with positive and negative leptons, respectively. Figures (c) and (d) show the fit for events with an electron and for events with a muon.	130
A.6	Several key distributions, reproduced using only events that contain four or more tight jets. Shown are qy_ℓ (a) and p_T^ℓ (b) before background subtraction, along with $S(qy_\ell)$ (c) and $A_{\text{FB}}^\ell(qy_\ell)$ (d) after background-subtraction.	131
A.7	Several key distributions, reproduced using only events that contain exactly three tight jets and one loose jet. Shown are qy_ℓ (a) and p_T^ℓ (b) before background subtraction, along with $S(qy_\ell)$ (c) and $A_{\text{FB}}^\ell(qy_\ell)$ (d) after background-subtraction.	132
A.8	A comparison of the acceptance-correct qy_ℓ fits between events with four or more tight jets (b) and events with exactly three tight jets and one loose jet (a).	133

LIST OF TABLES

Table

1.1	The classes of final states that result from the decay of a top-quark pair. Each of the two W bosons can decay either hadronically (as quarks) or leptonically (as a lepton and a neutrino). Final-state quarks evolve into jets of hadrons. The final state of the top-quark pair is <i>hadronic</i> if both W bosons decay hadronically, <i>dilepton</i> if both decay leptonically, and <i>semileptonic</i> if one decays hadronically and the other leptonically. The quoted branching ratios are taken from Ref. [14].	13
1.2	The spin-analysing power h_i of a top quark's decay products [15, 16]. Here, spins are defined in terms of the <i>helicity basis</i> – a right-handed top (antitop) has its spin parallel (antiparallel) to its direction of motion in the top-quark pair rest frame.	14
1.3	Several measurements of the asymmetry in top-quark pair-production at the Tevatron, $A_{\text{FB}}^{\Delta y}$. Note that the lower-luminosity ℓ +jets measurements are conducted on subsets of the full-luminosity data samples.	18
1.4	The asymmetry of leptons produced in the decay of top-quark pairs, as measured in several channels by the CDF and D0 collaborations. Shown also are the combinations of each collaboration's measurements. \star : This result is documented in the present work.	21
2.1	Design parameters for the CDF-II Central Outer Tracker [7].	34
2.2	Design parameters for the CDF-II Secondary VerteX Layers [8].	38
2.3	Design parameters for the CDF-II Intermediate Silicon Layers [8, 9].	40
2.4	Comparison of design parameters for the CDF-II central and plug calorimeters [7].	44
2.5	Design parameters for three of the four CDF-II muon detection subsystems (IMU is not shown). Pion interaction lengths and multiple scattering assume a reference angle of $\theta = 90^\circ$ in CMU and CMP/CSP and an angle of $\theta = 55^\circ$ in CMX [7].	46
3.1	Electron identification requirements [17].	61

3.2	Cuts for muon identification. In this table, x is the <i>local</i> x defined by the drift direction of the chamber. ΔX is the distance between the muon stub and extrapolated track measured in the plane of the module. Fiducial distances are measured between the extrapolated track and the nearest chamber edge [17].	63
3.3	Track selection requirements for the SECVTX algorithm [18].	72
4.1	The selection requirements for events in this analysis. The first section lists cuts applied to all regions. The remaining sections list the additional cuts that are individually applied to the signal and each control region.	82
4.2	Production-level asymmetries and polarizations for the model datasets. Here, the polarization is defined as $P = (N(t_R\bar{t}_R) - N(t_L\bar{t}_L)) / (N(t_R\bar{t}_R) + N(t_L\bar{t}_L))$, with the beamline taken as quantization axis. The statistical uncertainty on the final digit is shown in parenthesis.	86
4.3	The theoretical cross-sections used for top-quark pair production and those background processes whose yields are not derived from data [19].	91
4.4	The estimated yield of processes which produce events in the signal region, compared to the observed number of events.	93
4.5	Asymmetries and yields of the dominant background processes in the signal region. The final column is the relative contribution of that process to the total background asymmetry.	98
4.6	The estimated yield of processes which produce events in the $W+1$ jet control sample, compared to the observed number of events. The overall $W +$ jets normalization is chosen so that the number of predicted and observed events are equal.	100
4.7	The qy_ℓ asymmetry in the $W+1$ jet sample, compared to Standard Model expectations, for small and large lepton p_T^ℓ	101
4.8	The qy_ℓ asymmetry in the $W+1$ jet sample, compared to Standard Model expectations, for small and large $ \eta_\ell $	101
4.9	The estimated yield of processes which produce events in the zero-tag control sample, compared to the observed number of events.	103
4.10	Comparison of the predicted and measured asymmetries in the zero-tag sample. “Signal + backgrounds” is the predicted asymmetry when the A_{FB}^ℓ of the $t\bar{t}$ component is fixed to 0.070.	104
5.1	Bin-by-bin values that are used in the extrapolation procedure. These quantities are measured in simulated events generated by POWHEG. The first column shows the bin range. The second column lists the predicted bin centroids, calculated as a weighted mean. The third column shows the asymmetries of the acceptance $A^C(qy_\ell)$ in each bin.	110
5.2	Best-fit values of the parameter a for the benchmark models (Eq. (5.11); 119 d.f.).	113
5.3	True asymmetries as generated in simulation compared to mean extrapolated results for 10 000 simulated experiments with the yield of the $t\bar{t}$ component as in the data. Uncertainties are negligible.	115
5.4	Uncertainties on the fully-extrapolated measurement.	121

5.5	Table summarizing the resulting asymmetries when the sample is divided by either charge or lepton type. Also included is the inclusive result.	122
B.1	The measured population of the CDF-II data in each bin in qy_ℓ , compared to the prediction of POWHEG and the nominal background model.	135
B.2	The population of each bin in qy_ℓ after the nominal background prediction has been subtracted from the CDF-II data.	135
B.3	The symmetric part $S(qy_\ell)$ of the background-subtracted CDF-II data, compared to the prediction of POWHEG.	136
B.4	The binned asymmetry $A_{\text{FB}}^\ell(qy_\ell)$ of the background-subtracted CDF-II data, compared to the prediction of POWHEG.	136

LIST OF APPENDICES

Appendix

A.	Cross-Checks of the Inclusive Lepton Asymmetry	125
B.	Bin Contents and Binned Asymmetries in the Signal Region	134

ABSTRACT

A Measurement of the Leptonic Asymmetry in Top-Quark Pairs
Produced in $p\bar{p}$ Collisions at $\sqrt{s} = 1.96$ TeV

by

Ryan Edgar

Chair: Professor Dante Amidei

The asymmetry in the charge-weighted lepton rapidity qy_ℓ is measured in semileptonic top-quark-pair decays. The measurement is performed in data recorded with the CDF-II detector using the full Tevatron Run II sample, corresponding to an integrated luminosity of 9.4 fb^{-1} . A new technique is developed to correct the data for the finite acceptance of the detector and recover the production-level asymmetry. The result of $A_{\text{FB}}^\ell = 0.094_{-0.029}^{+0.032}$ is approximately 1.9 standard deviations above the standard model next-to-leading-order prediction of $A_{\text{FB}}^\ell = 0.038 \pm 0.003$.

CHAPTER I

Introduction; the Standard Model and the Top Quark

The Standard Model is the most comprehensive and experimentally well-validated theory of physical phenomena yet proposed. Using the language of relativistic quantum field theories with local gauge invariance, it successfully describes nearly all of the observed behavior of fundamental particles. Since the Standard Model's origin as a cohesive theory in the late 1960s, it has withstood an increasingly exacting suite of experimental tests, culminating most recently in the discovery of the Higgs boson, the final major prediction of the Standard Model to be verified.

Despite its experimental success, the Standard Model is not complete. Many subjects of active investigation fall beyond its reach. The Standard Model does not allow for neutrino mass and oscillations. It does not incorporate gravity, nor does it provide any explanation for dark matter or dark energy. It has many free parameters, some seemingly arbitrary or inexplicable and others unnervingly fine-tuned. Theories of the early universe generally require a period of rapid expansion shortly after the Big Bang, but no mechanism for this is to be found in the Standard Model. It does not explain the excess of matter over antimatter.

Numerous extensions to the Standard Model have been proposed to account for these effects. Many or most of these extensions predict new physical phenomena at

very high energies, often within the reach of current or future colliders. As such, the field of experimental high-energy physics consists of two related programs: direct *searches* for the presence of the new particles usually predicted by these models, and precision *measurements* to simultaneously test the Standard Model and constrain potential new models.

This dissertation presents a measurement: A_{FB}^ℓ , the forward-backward asymmetry of the leptons produced in the semileptonic decays of top-quark pairs. This measurement is particularly motivated by discrepancies observed in the production of top-quark pairs at the Tevatron, as will later be described. However, the surprisingly large mass of the top quark has long induced speculation that it might have some special role, or participate in yet-undiscovered physical interactions. The lepton asymmetry is sensitive to multiple aspects of top-quark pair production, and serves to constrain some of these possibilities.

The remainder of this chapter provides a (very) brief overview of the Standard Model, the experimental status of the top quark, and the context of the present measurement. **Chapter II** describes the Fermilab accelerator complex, the Tevatron, and the CDF-II detector - the origin of the data with which this work was performed. **Chapter III** describes the reconstruction of physics objects from the recorded detector signals. **Chapter IV** documents the criteria for selecting recorded events, describes the models for the signal and backgrounds, and verifies that those models correctly describe the data. Finally, **Chapter V** develops and validates the methodology used to measure A_{FB}^ℓ , applies that method to actual data, and studies the associated uncertainties.



Figure 1.1. The chapter headpiece.

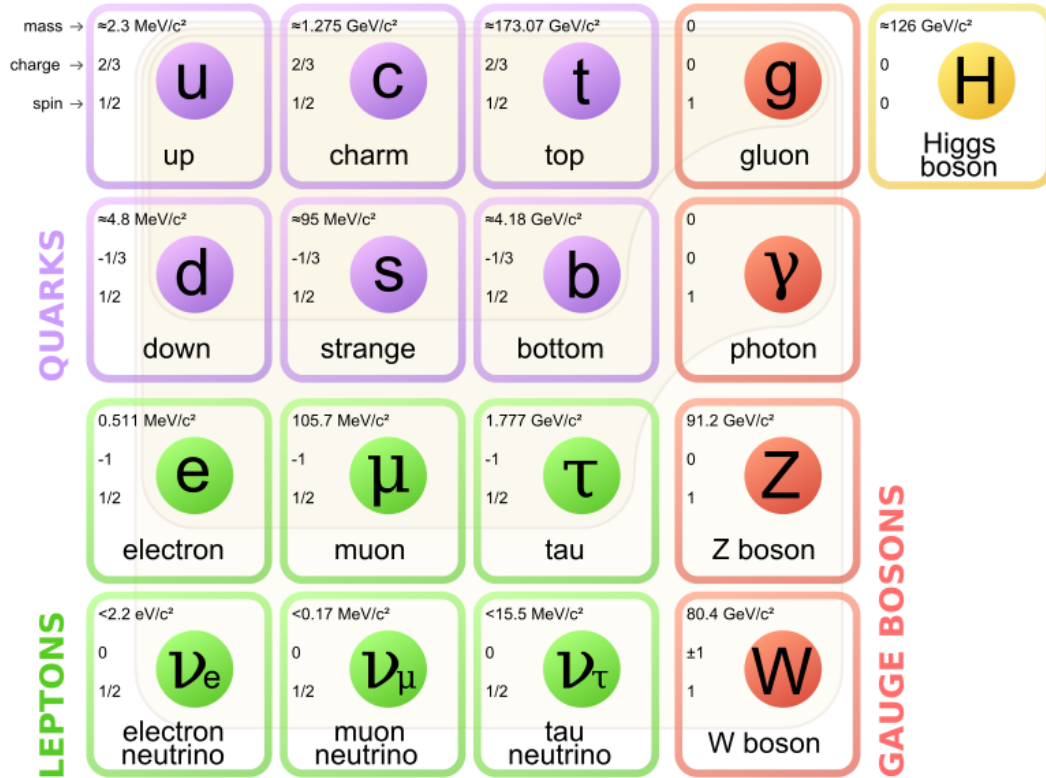


Figure 1.2. The known fundamental particles of the Standard Model [1]. Three generations of spin-1/2 quarks and leptons interact via the exchange of spin-1 vector gauge bosons. The spin-0 Higgs provides mass to the W and Z, the quarks, and the charged leptons.

1.1 The Standard Model

Figure 1.2 illustrates the seventeen known species of fundamental particles. The diagram shows the name of each particle, its mass, electric charge, and intrinsic spin. The twelve spin-1/2 fermions form two categories: the six flavors of *quarks*, which interact via the strong force, and six *leptons*, which do not. Each of these has also an anti-particle counterpart, with all internal quantum numbers opposite its matter partner. The fermions are grouped into three generations, each more massive than the last. Fermions of the first generation – the up and down quarks, and the electron – comprise all ordinary matter.

The Standard Model also includes four families of spin-1 *gauge bosons*, which mediate three of the four known fundamental forces. These are the gluons (g), the

quanta of the strong force; the W and Z , the quanta of the weak force; and the photon (γ), the quanta of electromagnetism. Together with the Higgs boson, the latter two of these forces have been successfully combined as a unified *electroweak* theory. Although outside the strict purview of the Standard Model, theories of quantum gravity generally predict a yet-undiscovered *graviton* as the quanta of the gravitational force.

Each Standard Model force results from a particular *local gauge symmetry* described by a *gauge group*: a continuous set of unitary transformations, each of which nontrivially acts on the theory's fields while leaving observable physical quantities unchanged. These gauge symmetries are *local*: they may be continuous functions of position and the invariance is still expected to hold. Formally, the Standard Model is described by the direct product of three continuous gauge groups:

$$\text{SU}(3)_C \times \text{SU}(2)_L \times \text{U}(1)_Y .$$

Each of these symmetries implies a set of conserved charges, a consequence of Noether's theorem. A fermion with nonzero charge under a given gauge symmetry can interact by emitting or absorbing one of the associated gauge bosons. The allowed interactions in the Standard Model are shown in Figure 1.3. The charged leptons interact through the weak and electromagnetic forces, the neutrinos through the weak force alone, and the quarks through all three forces. The strengths of these interactions, when allowed, are dictated by the *gauge couplings* associated with each force. The three couplings are not specified by the Standard Model and must be determined experimentally.

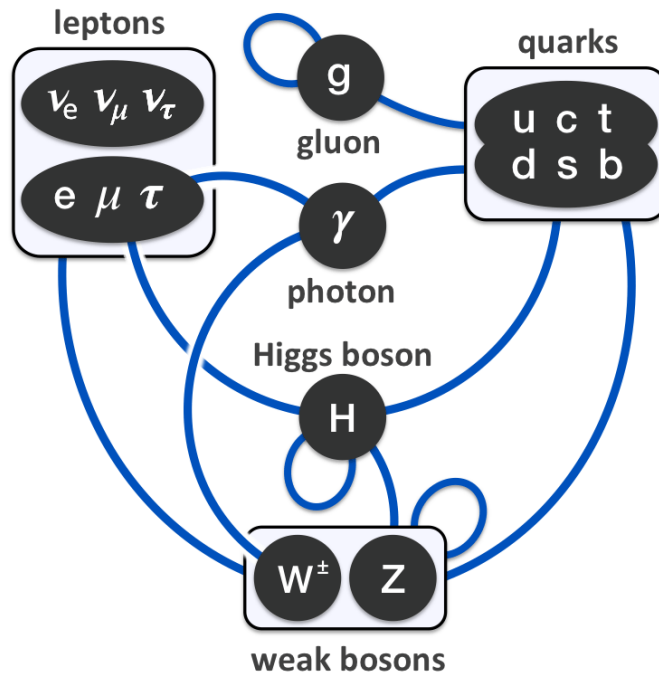


Figure 1.3. The interactions between the Standard Model fermions and bosons [2].

Quantum Chromodynamics

The $SU(3)_C$ part of the Standard Model gauge group – known as Quantum Chromodynamics (QCD) – describes the strong force. At low energies, it binds quarks into hadrons. The hadron’s quantum numbers are determined by its *valence quarks*. Additionally, gluons and short-lived *sea quarks* contribute to a hadron’s structure. The catalog of hadrons is lengthy; it includes as its most well-known elements the proton (uud) and neutron (udd). The attempt to order the hadrons in some way was historically one of the driving factors in the development of QCD.

The charge associated with the strong force, held by both quarks and gluons, is known as color. Quarks have three possible color states: red, green, and blue. Anti-quarks, naturally enough, have three corresponding anti-color states. A gluon has one color along with one anti-color. Of the nine possible color combinations, eight are valid elements of $SU(3)_C$ (the color-singlet state $(r\bar{r} + g\bar{g} + b\bar{b})/\sqrt{3}$ is not).

Because the gluons themselves have color, they are self-interacting. One consequence is *confinement*: the force between two colored particles increases as they move apart. Eventually, it becomes energetically favorable to produce quark-antiquark pairs from the vacuum. For this reason, colored particles can remain unbound only for very short times ($\tau \simeq 5 \times 10^{-24}$ s). When highly energetic quarks are produced by cosmic rays or in colliders, the quark rapidly evolves into a spray of particles known as a *jet*, in a process known as fragmentation or hadronization. The sole exception to this behavior is the top quark, which (as later described) decays before hadronization can occur.

Electroweak Theory

The $SU(2)_L \times U(1)_Y$ gauge groups in the Standard Model correspond to the weak and electromagnetic forces. This correspondance is not direct. In isolation, the $SU(2)_L$ gauge symmetry requires that the associated gauge bosons be massless. This is incompatible with the observed fact that the W and Z are, in fact, quite massive. This deficiency is addressed by the *Higgs mechanism*, a way for the self-interacting spin-zero Higgs field to create apparent masses for the W and Z at low energies through interactions with a space-filling Higgs condensate.

One consequence of the Higgs mechanism is that the photon and Z boson that are observed at low energies are in fact mixtures of the neutral components of the underlying gauge groups. The neutral component W_μ^0 of the $SU(2)_L$ gauge field mixes with the $U(1)_Y$ gauge field B_μ to create the physical photon and Z :

$$\begin{pmatrix} A_\mu \\ Z_\mu \end{pmatrix} = \begin{pmatrix} \cos \theta_w & \sin \theta_w \\ -\sin \theta_w & \cos \theta_w \end{pmatrix} \begin{pmatrix} B_\mu \\ W_\mu^0 \end{pmatrix}, \quad (1.1)$$

where θ_w is the weak mixing angle or ‘Weinberg angle’, which parameterizes the amount of mixing between the neutral components. The weak mixing angle is not

predicted by the Standard Model and must be measured through experiment. It directly impacts numerous Standard Model predictions, including the relative mass of the W and Z bosons, and the degree of parity violation in neutral current interactions. The presently accepted value is $\sin^2 \theta_w (M_Z) = 0.23116(12)$ [14].

Charges are associated with each of the two gauge groups. The charge under the $U(1)_Y$ gauge group is the *weak hypercharge*, Y_W ; under $SU(2)_L$ it is T_3 , the weak isospin. Since the electromagnetic force is a mixture of these two interactions, the electric charge is a mixture of the two charges:

$$Q = \frac{Y_W}{2} + T_3. \quad (1.2)$$

The weak force is unique in several respects. It does not induce the formation of bound states, unlike the other forces. It can change the flavor of a quark or lepton via emission or absorption of a W boson (charged currents; Fig. 1.4). Additionally, it is maximally parity-violating: left-handed fermions participate in weak interactions, while right-handed fermions do not. Parity violation in the Standard Model is implemented by assigning *different* hypercharge and isospin to left- and right-handed fermions. Left-handed fermions have $T_3 \neq 0$ and couple to the W^\pm , the Z , and the photon. Right-handed fermions have $T_3 = 0$ and couple to the photon alone.

Quark Mixing and the CKM Matrix

Nominally, the quarks participate in the weak interaction in the form of three doublets, consisting of the up- and down-type quarks of each generation. In fact, the objects to which the weak interaction couples are *superpositions* of quarks. A consequence is that weak decays which involve the emission of a W can convert quarks of one generation to another. Were this not the case, the lighter quarks of the second and third generation – the s and b – would be stable. The extent of this mixing

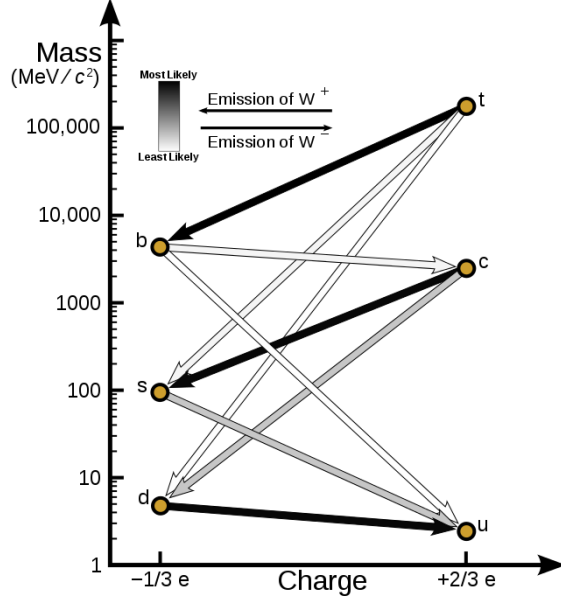


Figure 1.4. Charged currents involved in the weak decays of quarks. An up-type quark (charge $+2/3$) can decay to a W^+ (charge $+1$) and a higher down-type quark (charge $-1/3$). Similarly, a down-type quark can decay to a lighter up-type quark via the emission of a W^- . The colors correspond to the probability of a particular decay, and encode the magnitudes of the CKM matrix elements [3].

in weak decays is encoded as a 3×3 unitary matrix called the Cabibbo-Kobayashi-Maskawa (CKM) matrix.

The contents of this matrix are not specified by the Standard Model. They have been the subject of an extensive program of measurement. From Ref. [14], direct measurements of the magnitudes of each element result in

$$\begin{bmatrix} |V_{ud}| & |V_{us}| & |V_{ub}| \\ |V_{cd}| & |V_{cs}| & |V_{cb}| \\ |V_{td}| & |V_{ts}| & |V_{tb}| \end{bmatrix} = \begin{bmatrix} 0.97425 \pm 0.00022 & 0.02252 \pm 0.0009 & 0.00415 \pm 0.00049 \\ 0.230 \pm 0.011 & 1.006 \pm 0.023 & 0.0409 \pm 0.0011 \\ 0.0084 \pm 0.0006 & 0.0429 \pm 0.0026 & 0.89 \pm 0.07 \end{bmatrix}. \quad (1.3)$$

This is also shown graphically in Figure 1.4. If its unitarity is assumed, then the CKM matrix can be expressed in terms of only four parameters: three mixing angles and one complex phase. These can be better-constrained than the direct measurements shown here; in particular, if the CKM matrix is unitary, then $|V_{tb}| = 0.999146^{+0.000021}_{-0.000046}$ [14].

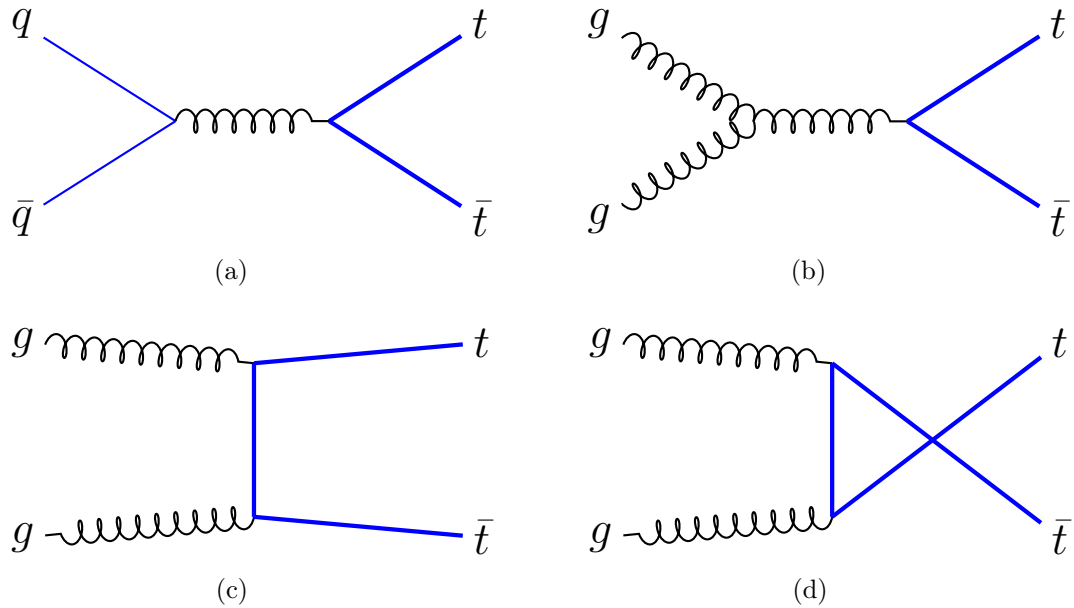


Figure 1.5. Leading-order diagrams contributing to top-pair production. Quark-antiquark annihilation (Fig. (a)) contributes 85% of the Tevatron cross-section, while gluon-gluon fusion (Fig. (b), (c), (d)) contributes the remaining 15%. At the Large Hadron Collider, these proportions are approximately reversed.

1.2 Properties of the Top Quark

The most massive known elementary particle, the top quark has been considered a fertile testing-ground for the Standard Model as well as non-SM effects since its first discovery. Its large mass and short lifetime provide numerous experimental challenges, both in production and analysis.

1.2.1 Production

At the Tevatron, top-quark pairs ($t\bar{t}$) are predominantly produced by quark-antiquark ($q\bar{q}$) annihilation. These events constitute approximately 85% of the total yield. The remaining 15% are produced by gluon-gluon fusion processes. At leading order, a single s -channel $q\bar{q}$ annihilation diagram (Fig. 1.5a) is therefore the dominant contribution to top production.

Because the colliding hadrons that initiate an interaction are composite particles,

the exact center-of-mass energy in a particular collision is unknown. A proton with well-determined momentum has that momentum probabilistically divided amongst its constituent particles, or *partons*. To account for this, theoretical predictions must be integrated over all possible momentum configurations. *Parton distribution functions* (PDFs) parametrize the probability of finding an initiating parton i with momentum fraction x_i for each valence quark, gluon, and sea quark type.

The top-quark pair production cross-section can be written in terms of the parton distribution functions and partonic interaction cross-sections:

$$\sigma_{t\bar{t}} = \sum_{i,j} \int dx_1 dx_2 F_i^{(p)}(x_1; \mu_F) F_j^{(\bar{p})}(x_2; \mu_F) \hat{\sigma}_{ij \rightarrow t\bar{t}}(\hat{s}; \mu_F, \mu_R). \quad (1.4)$$

Here, the sum runs over all possible combinations of initiating partons. The functions $F_i^{(p)}$ and $F_j^{(\bar{p})}$ are the parton-distribution functions for partons of species i and j , and x_1 and x_2 are the momentum fractions of the initiating partons. $\hat{\sigma}$ is the partonic interaction cross-section, $\hat{s} = x_1 x_2 s$ is the square of the partonic center-of-mass energy, and \sqrt{s} is the hadron center-of-mass energy.

There are two free parameters in the above expression. The factorization scale μ_F controls the energy below which dynamics of the initiating partons are expected to be captured by the PDFs. The renormalization scale μ_R determines the energy at which the QCD running coupling $\alpha_S(\mu_R^2)$ is evaluated. Both may be regarded as residual dependences on computational machinery, resulting from nonperturbative effects (μ_F) or truncated perturbative expansions (μ_R). A common choice (also used for the production of the simulated events that will be utilized later) is to set both scales equal to the transverse mass of the top in the rest frame of the initiating partons: $\mu_F = \mu_R = m_t^2 c^4 + p_T^2 c^2$.

The Standard Model prediction for the inclusive top-quark pair-production cross-section has been computed to an ever-increasing degree of precision. Most recently,

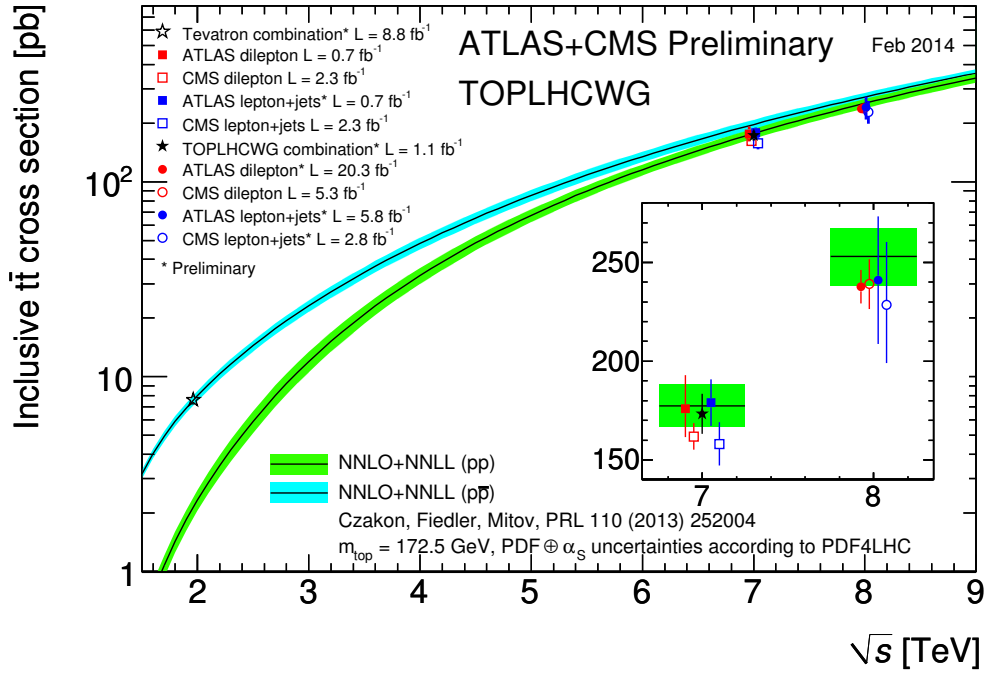


Figure 1.6. Summary of LHC and Tevatron measurements of the top-pair production cross-section as a function of the centre-of-mass energy \sqrt{s} . Shown also are the NNLO QCD calculations with NNLL resummation. [4].

the full next-to-next-to-leading order prediction with soft gluon resummation (NNLO + NLL) has been computed in Ref. [20]. The NNLO + NLL Tevatron cross-section of $7.164^{+0.11+0.17}_{-0.20-0.12}$ pb at $\sqrt{s} = 1.96$ TeV compares well with the combined CDF and D0 result of 7.6 ± 0.41 pb [21]. Similar good agreement is seen between the predicted and measured cross-section at the LHC, both at $\sqrt{s} = 7$ TeV and $\sqrt{s} = 8$ TeV (Fig. 1.6).

1.2.2 Mass, Width, and Lifetime

In the Standard Model, the mass of the top quark m_t is a free parameter. Of all the intrinsic properties of the top quark, it has been subject to the greatest experimental investigation and is now known to a precision of 0.5%, the best precision of any quark mass [14]. The most recent Tevatron combination, $m_t = 173.2 \pm 0.51 \pm 0.71$ GeV [22], is in excellent agreement with the LHC measurement of $m_t = 173.29 \pm 0.23 \pm 0.92$ GeV [23].

The top quark's width, on the other hand, is determined fully in the Standard Model by its mass and couplings. At next-to-leading order in α_S , it is given by

$$\Gamma_{(t \rightarrow Wb)} = \frac{G_F m_t^3}{8\pi\sqrt{2}} |V_{tb}|^2 \left(1 - \frac{M_W^2}{m_t^2}\right)^2 \left(1 + 2\frac{M_W^2}{m_t^2}\right) \left[1 - \frac{2\alpha_S}{3\pi} \left(\frac{2\pi^2}{3} - \frac{5}{2}\right)\right] \quad (1.5)$$

where G_F is the Fermi constant for weak decay, M_W is the mass of the W boson, α_S is the strong coupling constant, and $|V_{tb}|^2$ is the $t \rightarrow Wb$ transition probability [24]. Because $|V_{tb}| \approx 1$, this is by far the dominant contribution to the top quark's width in the Standard Model. With $m_t = 173.3$ GeV and $\alpha_S(M_Z) = 0.118$, this evaluates to $\Gamma_t = 1.35$ GeV [14]. Direct measurements of Γ_t are experimentally challenging; CDF has set a 95%-confidence-level limit of $\Gamma_t \leq 6.38$ GeV using the invariant mass distribution of top quarks in $\ell + \text{Jets}$ events [25]. Indirect measurements from D0, based on the t -channel single-top-quark production cross-section and measured branching ratio $\mathcal{B}(t \rightarrow Wb)$, find $\Gamma_t = 2.00_{-0.43}^{+0.47}$ [26].

These measurements imply that the top quark's lifetime is very short: $\tau < 6 \times 10^{-25}$ s. The characteristic energy scale for quarks to bind into hadrons via the strong force is $\Lambda \approx 170$ MeV, equivalent to about 5×10^{-24} s. Thus, unique amongst the quarks, the top is too unstable to form bound states, decaying instead as a bare quark.

1.2.3 Decay

Because $|V_{tb}| \approx 1$, the top quark decays almost exclusively into a W boson and a bottom quark. The W boson has several decay modes, and so the top quark also has multiple final states. (Tbl. 1.1). This results in an effectively three-body decay with a unique resonance structure. The top quark is narrow ($\Gamma_t/m_t \ll 1$), so its three decay products have an invariant mass around m_t . Since the W boson is both narrow and lighter than m_t ($M_W = 80.385$ GeV [14]), the W boson produced in a top decay

Table 1.1. The classes of final states that result from the decay of a top-quark pair. Each of the two W bosons can decay either hadronically (as quarks) or leptonically (as a lepton and a neutrino). Final-state quarks evolve into jets of hadrons. The final state of the top-quark pair is *hadronic* if both W bosons decay hadronically, *dilepton* if both decay leptonically, and *semileptonic* if one decays hadronically and the other leptonically. The quoted branching ratios are taken from Ref. [14].

Channel	(Anti)Top-Quark Decay	Branching Ratio (Theory)
All-hadronic	$t\bar{t} \longrightarrow W^+b \longrightarrow q\bar{q}'b$	45.7%
	$W^-\bar{b} \longrightarrow \bar{q}''q'''\bar{b}$	
Dilepton	$t\bar{t} \longrightarrow W^+b \longrightarrow \ell^+\nu b$	10.5%
	$W^-\bar{b} \longrightarrow \ell^-\bar{\nu}\bar{b}$	
Semi-leptonic	$t\bar{t} \longrightarrow W^+b \longrightarrow q\bar{q}'b$	43.8%
	$W^-\bar{b} \longrightarrow \ell^-\bar{\nu}\bar{b}$	
	$t\bar{t} \longrightarrow W^+b \longrightarrow \ell^+\nu b$	
	$W^-\bar{b} \longrightarrow \bar{q}q'\bar{b}$	

is *real* – its mass is usually close to M_W . This creates a second resonance within the three top decay products, where the two objects that originated from the W have an invariant mass near M_W .

The top quark decays before strong interactions can dilute the spin state set at production. Because it decays through the parity-violating weak interaction, the angular distributions of the top quark’s decay products are sensitive to the direction of its spin. These angular distributions are given by [15]

$$\frac{dN}{d\cos\theta_i^*} = \frac{1}{2}(1 + h_i \cos\theta_i^*). \quad (1.6)$$

Here, θ_i^* is the angle of fermion i with respect to the momentum of the top-antitop system as measured in the rest frame of the parent quark. The coefficient h_i (Tbl. 1.2) effectively measures the spin-analyzing power of fermion i . It is immediately evident that charged leptons, when produced, are the most powerful probe of the parent top quark’s spin. Unlike the jets produced by final-state quarks, a charged lepton is clearly distinguishable in the detector; furthermore, its spin-analyzing power is maximal.

Table 1.2. The spin-analysing power h_i of a top quark’s decay products [15, 16]. Here, spins are defined in terms of the *helicity basis* – a right-handed top (antitop) has its spin parallel (antiparallel) to its direction of motion in the top-quark pair rest frame.

Fermion	$h_i(t_R, \bar{t}_L)$	$h_i(t_L, \bar{t}_R)$
$\bar{\nu}, u, c$	-0.31	+0.31
ℓ, \bar{d}, \bar{s}	+1	-1
b	-0.41	+0.41
ν, \bar{u}, \bar{c}	+0.31	-0.31
$\bar{\nu}, d, s$	-1	+1
b	+0.41	-0.41

The spin-analyzing power of the lepton may also be understood as a direct consequence of the V-A charged current interaction. The order in which the spinors at the Wtb vertex are contracted is opposite that of the $W\nu\bar{\ell}$ vertex. The magnitude of the matrix element – and thus the probability of the decay – is therefore proportional to the overlap of the spins of the top quark and the lepton. However, the lepton is ultrarelativistic and produced with its spin (anti-)parallel to its direction of motion; the overlap can then be expressed directly in terms of the lepton’s production angle with respect to the top quark’s spin: $|\mathcal{M}| \propto (1 \pm \cos \theta) / 2$.

In the Standard Model, top-quark pairs are produced at the Tevatron with no net polarization. However, because the dominant production mechanism (Fig. 1.5a) produces top-quark pairs in a 3S_1 state with parallel spins, there are observable *spin correlations* between the top and antitop. The Tevatron spin correlation has been observed to be consistent with Standard Model predictions [27–29], though measurements have been limited by the statistical precision of the data. The predicted spin correlation at the LHC is smaller due to differing production mechanisms, but ATLAS [30] and CMS [31] have also found good agreement between the observed value and the Standard Model.

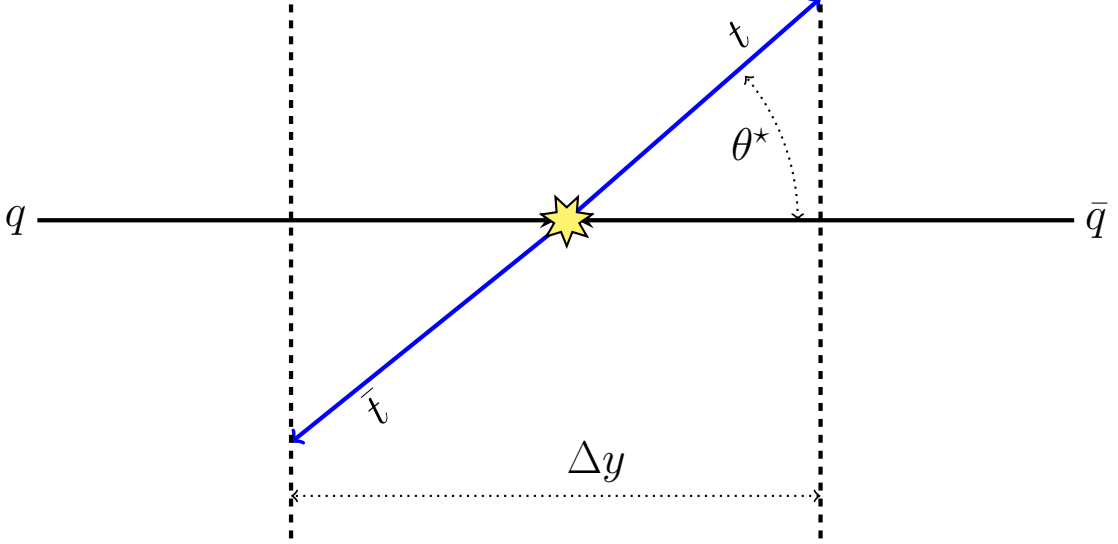


Figure 1.7. The production angle θ^* and the frame-invariant rapidity difference Δy of the $t\bar{t}$ system.

1.3 Top Quark Production Asymmetry

At the Tevatron, the directional distribution of top-quark pair-production is symmetric at leading order ($\mathcal{O}(\alpha_S^2)$, Fig. 1.5). Gluon-initiated diagrams $gg \rightarrow t\bar{t}$ are symmetric at all orders, but an asymmetry in $q\bar{q} \rightarrow t\bar{t}$ appears at $\mathcal{O}(\alpha_S^3)$. A single value, the top-quark pair-production asymmetry, captures the effect:

$$A_{\text{FB}}^{\Delta y} = \frac{N(\Delta y > 0) - N(\Delta y < 0)}{N(\Delta y > 0) + N(\Delta y < 0)}. \quad (1.7)$$

Here $\Delta y = y_t - y_{\bar{t}}$ is the difference in rapidities (see Sec. 2.2.1) between the top and antitop quarks. The rapidity is used as an experimentally-accessible proxy for the top-quark production angle θ^* (Fig. 1.7).

The Standard Model at next-to-leading order (NLO) in QCD predicts that the asymmetry is small. Four diagrams contribute to asymmetric production: the Born and box diagrams (Fig. 1.5a and 1.8b) interfere to produce a positive asymmetry, while initial- and final-state radiation (Fig. 1.8c and Fig. 1.8d) interfere to produce

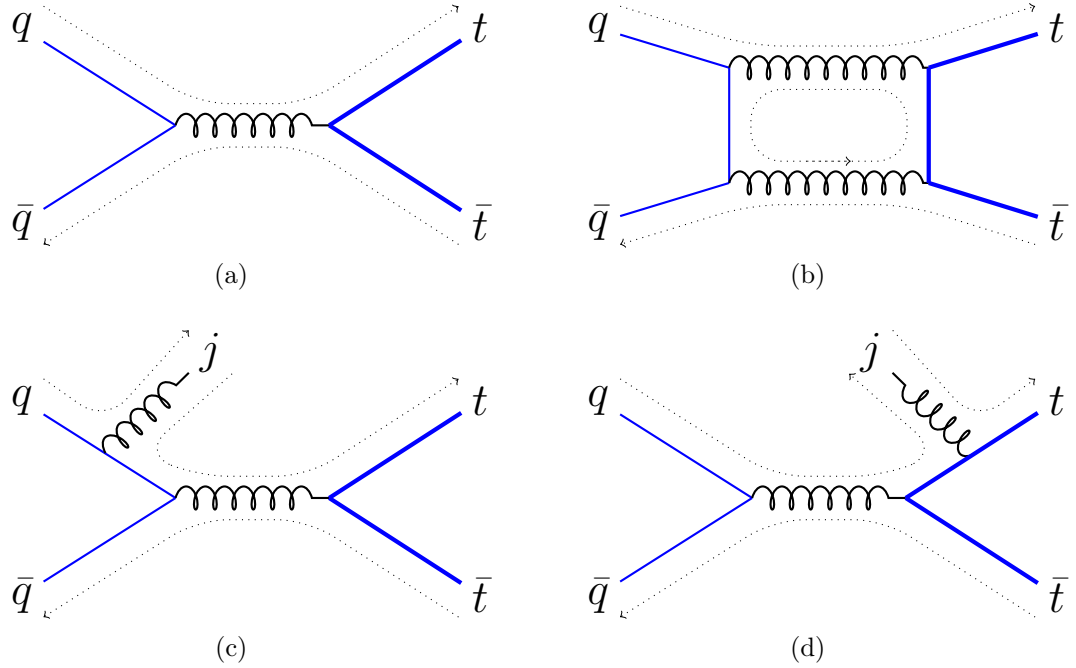


Figure 1.8. Leading-order diagrams contributing to the top-pair production asymmetry. Figures (a) and (b) interfere at low $p_T^{t\bar{t}}$ to produce a positive asymmetry. Figures (c) and (d) interfere at larger $p_T^{t\bar{t}}$ to produce a negative asymmetry. The dotted lines indicate the color flow in each diagram.

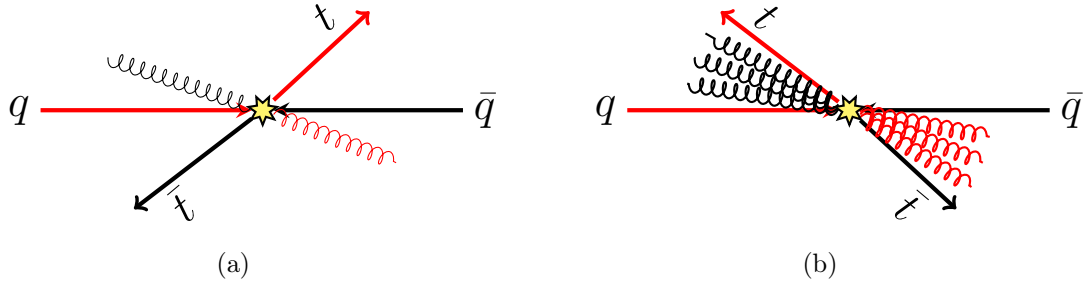


Figure 1.9. Color flow and QCD radiation in (a) forward events and (b) backward events [5].

a negative asymmetry. The inclusive asymmetry is calculated in Ref. [32], including also the contributions of electromagnetic and weak-interaction corrections, where the authors report a predicted asymmetry of $8.8 \pm 0.6\%$.

Since the diagrams that produce negative contributions to the SM asymmetry entail the production of an extra jet, negative asymmetries tend to be associated with top-quark pairs whose transverse momentum ($p_T^{t\bar{t}}$) is substantial. The positive

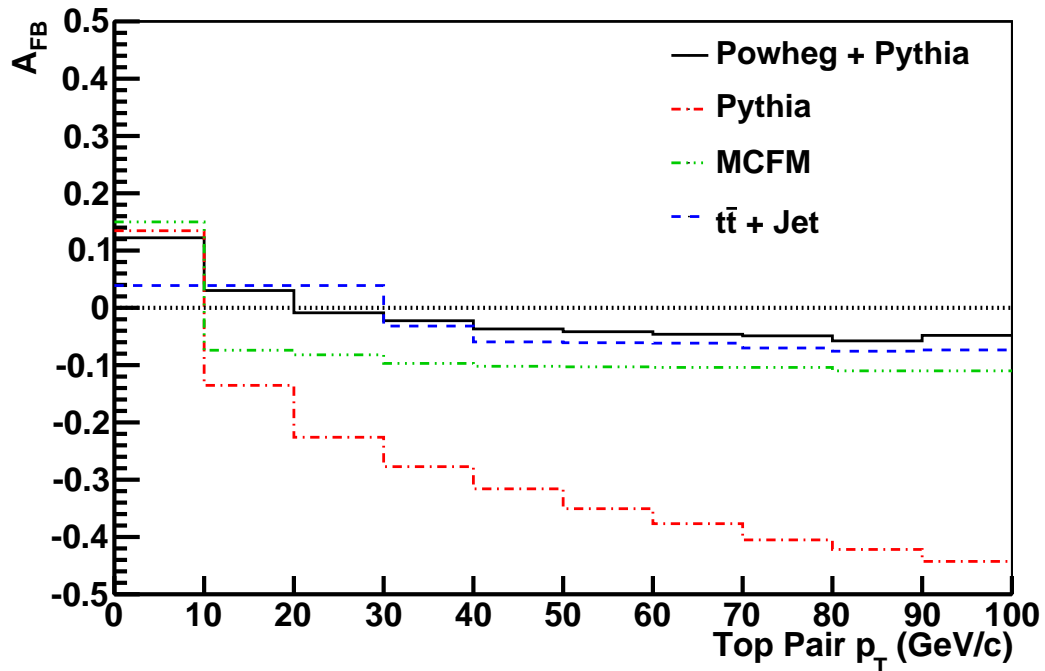


Figure 1.10. The top-quark production asymmetry $A_{\text{FB}}^{\Delta y}$ as a function of $p_{\text{T}}^{t\bar{t}}$, the transverse momentum of the $t\bar{t}$ system. The dependence is shown for several different generators.

contributions, on the other hand, are localized in events with low $p_{\text{T}}^{t\bar{t}}$ (Fig. 1.10). This effect can also be seen as a QCD analogue of Bremsstrahlung. Color predominantly flows from an initiating light quark to an outgoing top quark (and from \bar{q} to \bar{t} ; Fig. 1.8), forming a pair of initial-final color dipoles (Fig. 1.9). When there is a large deflection between the directions of the initiating light quark and the outgoing top quark, color charge is strongly accelerated and tends to greater emission. When the deflection is small (forward events), the induced radiation is similarly small [33].

This effect has been explored in the literature (Refs. [5, 33–35]), where substantial discrepancies between different simulated predictions have been reported. These differences are also evident in Figure 1.10. The impact of this effect on the inclusive asymmetry is generally small. However, the poorly-understood differential behavior will later prove to be an important source of systematic uncertainty.

Through much of the Tevatron’s Run II, both CDF and D0 consistently measured

Table 1.3. Several measurements of the asymmetry in top-quark pair-production at the Tevatron, $A_{\text{FB}}^{\Delta y}$. Note that the lower-luminosity ℓ +jets measurements are conducted on subsets of the full-luminosity data samples.

Measurement		$A_{\text{FB}}^{\Delta y}$
CDF ℓ +Jets [35]	9.4 fb ⁻¹	0.164 ± 0.047
CDF ℓ +Jets [36]	5.3 fb ⁻¹	0.158 ± 0.075
CDF Dilepton [50]	5.1 fb ⁻¹	0.42 ± 0.15 ± 0.05
D0 ℓ +Jets [51]	9.7 fb ⁻¹	0.106 ± 0.03
D0 ℓ +Jets [34]	5.4 fb ⁻¹	0.196 ± 0.065

asymmetries that were larger than the Standard Model prediction. In 5.3 fb⁻¹, CDF reported an asymmetry of 0.158 ± 0.075, which increased with the rapidity difference Δy and invariant mass $M_{t\bar{t}}$ of the $t\bar{t}$ system [36]. In a corresponding measurement using 5.4 fb⁻¹, D0 observed an asymmetry of 0.196 ± 0.065 but no apparent mass- or rapidity-dependence [34]. These results prompted many exotic models with new physical phenomena to explain the observed asymmetries (e.g. [37–48]).

Both measurements were repeated with improved technique in the full Tevatron Run-II sample. In 9.4 fb⁻¹, CDF measures an asymmetry of 0.164 ± 0.047 with approximately linear dependences on Δy and $M_{t\bar{t}}$ [35]. CDF also measures the differential cross-section as a function of the production angle $\cos\theta^*$ by decomposing its distribution into Legendre moments, finding good agreement except in the first (linear) moment, where the measurement of $a_1 = 0.40 \pm 0.12$ exceeds the predicted $a_1 = 0.15_{-0.03}^{+0.07}$ [49]. D0, on the other hand, measures $A_{\text{FB}}^{\Delta y} = 0.106 \pm 0.03$ in 9.7 fb⁻¹, compatible with both the CDF result and the Standard Model predictions. The final interpretation of the Tevatron measurements is therefore ambiguous. These results, both current and previous, are summarized in Table 1.3.

Measurements in pp collisions of the top-quark charge asymmetry A_C , an observable that is distinct from $A_{\text{FB}}^{\Delta y}$ but correlated with it, have found consistency with the Standard Model [52, 53]. However, any observable effect at the LHC is expected to be small, and the nature of the relationship between $A_{\text{FB}}^{\Delta y}$ and A_C is

model-dependent [44, 54–58].

1.4 The Lepton Asymmetry

An asymmetry can be defined for the leptons produced by the decay of a top quark using the lepton’s electric charge q and its rapidity in the lab frame y_ℓ (Sec. 2.2.1). If charge-parity symmetry (CP) is conserved, then for leptons of opposite charge, the asymmetries of the lepton rapidity are equal in magnitude but opposite in sign. They may then be combined by defining a charge-weighted lepton asymmetry,

$$A_{\text{FB}}^\ell = \frac{N(qy_\ell > 0) - N(qy_\ell < 0)}{N(qy_\ell > 0) + N(qy_\ell < 0)}. \quad (1.8)$$

There are two physical contributions to the lepton asymmetry. One is a simple kinematic effect: if a lepton is produced by the decay of a top quark in motion, that lepton inherits part of the momentum of its parent top. If the parent top-quarks are produced with a directional asymmetry, there will therefore be a smaller (but nonzero) asymmetry in the resulting decay products.

The second mechanism for asymmetric lepton production lies in the sensitivity of the lepton’s directional distribution to the spin state of its parent top quark (Table. 1.2). Excesses of right-handed ($t_R\bar{t}_R$) or left-handed ($t_L\bar{t}_L$) top-quark pairs produce significant changes to A_{FB}^ℓ [58–60]. Intuitively, in the case of right-handed production, top-quark pairs preferentially have the spin of both top and antitop quark aligned in the direction of motion of the initiating light quark. The decay of a top(antitop) quark with such a polarization favors the production of leptons with $y_\ell > 0$ ($y_\ell < 0$), producing an additional positive contribution to the asymmetry of qy_ℓ (Fig. 1.11). In the case of left-handed production, the signs are reversed, producing negative contributions to A_{FB}^ℓ .

In the Standard Model, top-quark pairs are produced with no net polarization;

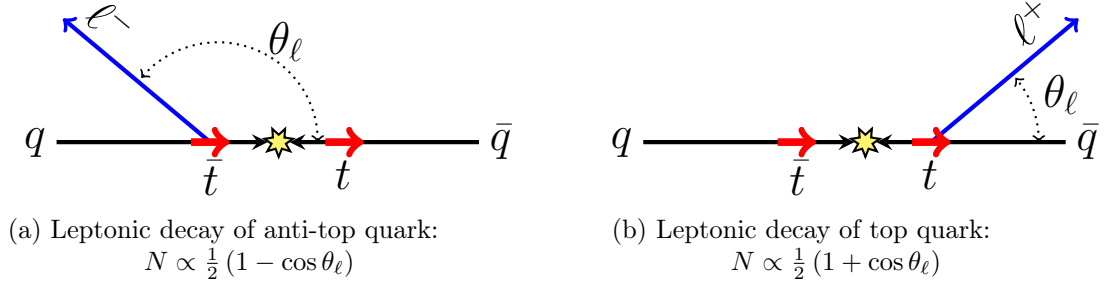


Figure 1.11. A top-quark pair produced at rest with a right-handed polarization in the beamline basis. In Fig. (a), the anti-top quark decays leptonically, sending more negative leptons into the backward region. In Fig. (b), the top quark decays leptonically and preferentially sends positive leptons into the forward region. This produces a forward-backward asymmetry in the charge-weighted lepton rapidity.

the lepton asymmetry is due only to the kinematic correlation with $A_{\text{FB}}^{\Delta y}$. This is calculated to NLO in Ref. [32], resulting in $A_{\text{FB}}^\ell = 0.038 \pm 0.002$.

On the other hand, many of the proposed exotic models for the top production asymmetry invoke mechanisms that would produce polarized top-quark pairs. The lepton asymmetry is therefore an independent observable that provides additional information on top-quark pair production. Furthermore, the measurements of $A_{\text{FB}}^{\Delta y}$ cited above rely on the reconstruction of the top-quark direction in complex final states with leptons, jets, and missing energy. The asymmetry of the lepton is accessible through simpler analysis, and it is therefore useful to investigate if this asymmetry supports the effects previously seen through more complex analysis.

While in principal other decay products are also sensitive to these effects, the lepton is ideal – leptons are unambiguously identified in the detector, have excellent charge determination, and are maximally sensitive to the spin of their parent quarks.

The present work documents the first measurement of the leptonic asymmetry A_{FB}^ℓ in the full Tevatron Run-II sample. Subsequent to its initial publication in Ref. [61], several additional measurements have been reported by both Tevatron collaborations. A CDF result in 9.1 fb^{-1} of dilepton events adopts the same correction methodology that will be developed here, and reports an asymmetry of 0.076 ± 0.082 [62]. That

Table 1.4. The asymmetry of leptons produced in the decay of top-quark pairs, as measured in several channels by the CDF and D0 collaborations. Shown also are the combinations of each collaboration’s measurements. \star : This result is documented in the present work.

Measurement		A_{FB}^ℓ	
\star	CDF ℓ +Jets [61]	9.4 fb^{-1}	$0.094_{-0.029}^{+0.032}$
	CDF Dilepton [62]	9.1 fb^{-1}	0.076 ± 0.082
	CDF Combination [62]		$0.090_{-0.026}^{+0.028}$
	D0 ℓ +Jets [51]	9.7 fb^{-1}	$0.042 \pm 0.023_{-0.020}^{+0.017} \quad y_\ell < 1.5$
	D0 Dilepton [63]	9.7 fb^{-1}	$0.044 \pm 0.037 \pm 0.011$
	D0 Combination [51]		$0.042 \pm 0.020 \pm 0.014 \quad y_\ell < 1.5$

works also reports a combination with the present result, yielding a CDF lepton asymmetry of $0.090_{-0.026}^{+0.028}$. A measurement performed by the D0 collaboration in 9.7 fb^{-1} of dilepton events measures $0.044 \pm 0.037 \pm 0.011$ [63]. D0 also reports a measurement in 9.7 fb^{-1} of semileptonic top-quark-pair candidates of $0.042 \pm 0.023_{-0.020}^{+0.017}$, and a combination with their dilepton result that yields a D0 lepton asymmetry of $0.042 \pm 0.020 \pm 0.014$ in the restricted lepton rapidity range $|y_\ell| < 1.5$ [51]. These results are summarized in Table. 1.4.

CHAPTER II

Experimental Apparatus

The Fermi National Accelerator Laboratory (Fermilab) in Batavia, IL has hosted experiments yielding numerous discoveries in particle physics, perhaps most notably the discoveries of the top and bottom quarks. The 10.6 square-mile site houses an interlinked complex of accelerators, designed to provide controlled beams of charged particles to meet a variety of experimental needs. From October 1985 through September 2011, Fermilab was the home of the Tevatron - the second-most energetic particle accelerator ever built, colliding protons and antiprotons at an energy of $\sqrt{s} = 1.96$ TeV.

This chapter describes the Fermilab accelerator complex (Fig. 2.2) as it relates to the production, acceleration, and collision of protons and antiprotons in the Tevatron. The CDF detector, used (as in the present work) to examine the debris of these collisions, is also described.



Figure 2.1. The chapter headpiece.

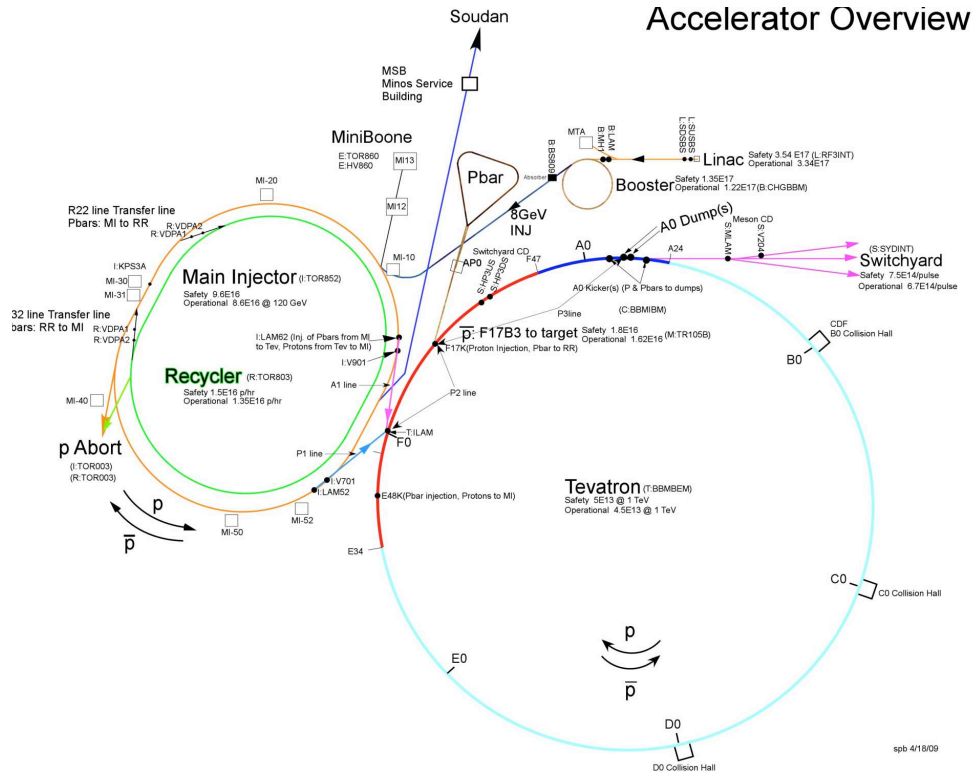


Figure 2.2. The Fermilab accelerator complex. Protons and antiprotons are accelerated through a sequence of several accelerators, eventually reaching 980 GeV per beam. The protons/antiprotons are then stored as countercirculating beams in the Tevatron, intersecting within the CDF and D0 detectors (location B0 and D0, respectively) [6].

2.1 The Fermilab Accelerator Complex

2.1.1 Proton Source and Preaccelerator

The preaccelerator (‘preacc’) is the first accelerator of the FNAL complex, supplying protons at 750 KeV to all of the downstream accelerators at a repetition rate of 15 Hz. Since the cessation of Tevatron operation, the preaccelerator has been replaced with an RF quadrupole accelerator which has greatly improved the beam-transfer efficiency to subsequent accelerators. For the entirety of the Tevatron’s lifetime, however, the preacc was an electrostatic Cockroft-Walton device.

H⁻ ions are produced by a magnetron-based source. A pulsed plasma arc impinges on a Cesium-coated cathode and sputters negative H⁻ ions. The extremely low work

function of Cesium aids in producing reasonable yields of H-. Electrons and negative ions exit the source when an 18 kV extractor is pulsed. Bending and focusing magnets separate the H- ions from electrons while controlling space-charge-induced beam divergences.

The ion source is enclosed in an electrically-conductive dome charged to a potential of -750 kV. An aperture in the dome leads to a column, through which the H- ions accelerate toward a grounded electrode. Upon exiting the accelerating column, the beam travels through a transfer line to the Linac. Two nearly-identical preaccs, misleadingly named ‘H-’ and ‘I-’, ensure continued operation in the event that one source fails. Each can provide a current of $65 - 70$ mA [64].

2.1.2 Linac

The linear accelerator (‘linac’) accepts H- ions at 750 KeV from the preacc and accelerates them to an energy of 400 MeV. It is actually two distinct linear accelerators – a five-stage drift tube linac operating at 201 MHz increases the beam energy to 116 MeV, and a subsequent seven-stage cavity linac at 805 MHz provides the remaining energy. Both linacs are water-cooled and constructed from Oxygen-Free High Conductivity (OFHC) copper. Their total length is about 150 m.

As a result of the difference in drive frequency, every cycle of the drift-tube linac is used to accelerate particles, while only every fourth cycle of the cavity linac is used. A buncher between the two sections aids in efficiently transferring the particle beam between the two geometrically-different accelerator segments. The linac operates at the same 15 Hz repetition rate as the preacc [64].

The 400 MeV H- beam may be transferred to several targets; for Tevatron utilization, the beam from the linac passes through the ‘400 MeV line’ to the Booster.

2.1.3 Booster and Main Injector

The Booster is the first synchrotron in the Fermilab complex. It is a 150 m diameter ring, with 17 RF accelerating cavities and a magnetic field which varies from 74 mT at injection to 0.7 T at extraction. Injection occurs over multiple turns, by merging H⁻ bunches from the linac with the existing beam and converted them to bare protons. A dipole injection magnet located at the injection point simultaneously moves an existing proton bunch and new H⁻ bunch into the same orbit. The bunch passes through a thin carbon stripper foil, which removes the electrons from the H⁻ ions. A second dipole magnet restores the newly-enlarged bunch to a stable orbit and ejects any residual H⁻ ions.

Under acceleration, the protons in the Booster accumulate an additional 500 KeV during each 2.2 μ s turn around the ring. Upon reaching an energy of 8 GeV, they are extracted to the Main Injector. Like the preceding accelerators, the Booster also operates at a 15 Hz repetition rate. [65]

The Main Injector further increases the energy to either 120 GeV or 150 GeV. An ellipse averaging 1 km in diameter, the Main Injector has 18 RF cavities and is able to accelerate protons or antiprotons every 2.2 s. It replaced an older synchrotron – the Main Ring – which shared the tunnel now housing the Tevatron. Multiple transfer lines allow the Main Injector to function as a central hub of the Fermilab complex, and as such it has several modes of operation: [66]

- *Antiproton production*: the Main Injector accelerates protons to 120 GeV for delivery to the antiproton target.
- *Proton and antiproton injection*, to raise the energy of protons and antiprotons to 150 GeV for injection into the Tevatron.
- *Fixed target experiments*, where protons and antiprotons are accelerated for delivery via the switchyard to a variety of fixed-target experiments.

2.1.4 Antiproton Source, Debuncher, Accumulator

Unlike protons, there is no convenient low-energy technology to generate antiprotons in copious numbers. Indeed, producing antiproton bunches with sufficiently large luminosity and low emittance is a worthy enough technical challenge that its accomplishment won Simon van der Meer the 1984 Nobel Prize. Antiproton production was a primary limiting factor in the achievable Tevatron luminosity. Even with the substantial improvement in antiproton production made over the course of nearly three decades of operation, accumulating a sufficient antiproton stockpile for a Tevatron store always remained a process of several hours.

Antiprotons are initially produced by a 120 GeV proton beam from the Main Injector impinging on a nickel-chromium alloy target (Inconel). Typically, the Main Injector delivers around 8×10^{12} protons every 2.2 s. The collisions yield a variety of particles with broad momentum spectra, a fraction of which are antiprotons. These secondary particles are collected and focused with a pulsed magnetic lens (a cylinder of liquid lithium carrying an axial current). A subsequent pulsed dipole selects antiprotons with an energy of approximately 8 GeV by mass/charge ratio. The overall yield is, on average, 2 antiprotons per 100,000 incident protons [67]. These antiprotons are directed into the Debuncher, while the remaining particles are absorbed by a beam dump.

The Debuncher functions to accept the ‘hot’ antiprotons from the Antiproton Source, and form them into low-emittance bunches which may be efficiently used by subsequent accelerators. This is accomplished by a technique known as ‘stochastic cooling’: a pickup sensor on one side of the ring monitors the beam shape and transmits a corrective signal to a kicker magnet across the diameter of the ring. Over the course of many cycles, the spread of particle momenta is reduced on average and the beam is ‘cooled’ into well-controlled bunches.

Just before the next pulse arrives from the target, cooled antiprotons from the

Debuncher are transferred to the Accumulator, a second circular synchrotron housed in the same tunnel. The Accumulator temporarily stores the antiprotons, ‘stacking’ multiple pulses from the Debuncher, and continues the cooling process. When a sufficient number of antiprotons have been accumulated, they are transferred back to the Main Injector. There they receive a small adjustment to their energy before being transferred to the Recycler [67].

2.1.5 Recycler

Sharing the Main Injector tunnel, the sole purpose of the Recycler is to store antiprotons. This was originally intended to accomplish two objectives: first, to provide a means to store larger numbers of antiprotons than the Accumulator; and second, to accept excess antiprotons at the end of a Tevatron store for reuse in subsequent stores. After early problems ‘recycling’ antiprotons from the Tevatron, the Recycler now only accepts antiprotons from the Accumulator. Unlike the other synchrotrons at Fermilab, the Recycler is constructed with permanent magnets, made from strontium ferrite with low-carbon steel pole pieces.

Antiproton cooling is continued in the Recycler. The Recycler has two cooling systems. First, antiprotons are cooled using a stochastic cooling system much like that of the Debuncher and Accumulator. Stochastic cooling becomes less effective with increased intensity; as larger antiproton stores are accumulated, the Recycler switches to electron cooling. In electron cooling, a beam of cold electrons is combined with the antiprotons. The colder electrons and hot antiprotons thermalize, reducing the temperature of the antiprotons. The electrons are then magnetically extracted, leaving more compact, high-luminosity antiproton bunches [68].

2.1.6 Tevatron

The Tevatron was the largest and final accelerator in the Fermilab complex. In 85s, it accelerated the 150 GeV protons and antiprotons from the Main Injector to a final energy of 980 GeV. This, however, occupied only a small fraction of normal operation – the Tevatron functioned primarily as a storage ring. Having reached their final energy, the countercirculating beams would be sustained for hours at a time. This is known as a *store*.

The Tevatron ring was roughly 2 km in diameter and had a 21 μ s period at $v \simeq c$. It was an approximate circle, with 8 superconducting accelerating cavities operating at a temperature of 4 K. It was divided into six sectors (A-F), each of which had five service buildings (0-4). The ‘0’ segments contained long, straight sections. A0 was the entry point of the transfer line from the Main Injector. The CDF detector was located at B0, and the D0 detector at its namesake.

The Tevatron was synchronized to a 53 MHz clock. Proton and antiproton bunches were phased to every twenty-first clock cycle – a 396 ns spacing. Each beam was separated into 36 bunches, which in turn were grouped into 3 trains of 12 bunches each. A 2.617 μ s gap between each bunch train allowed time for kicker magnets to energize in the event of a beam abort. Due to the limited availability of antiprotons, the antiproton beam was typically about 10% the intensity of the proton beam. The beams passed through each other at two Interaction Points (IPs), located in the CDF and D0 collision halls. At the interaction points, the beam diameter was a mere 2 μ m. Particles which did not collide continued to circulate until the stored beams were depleted below a useful level [69].

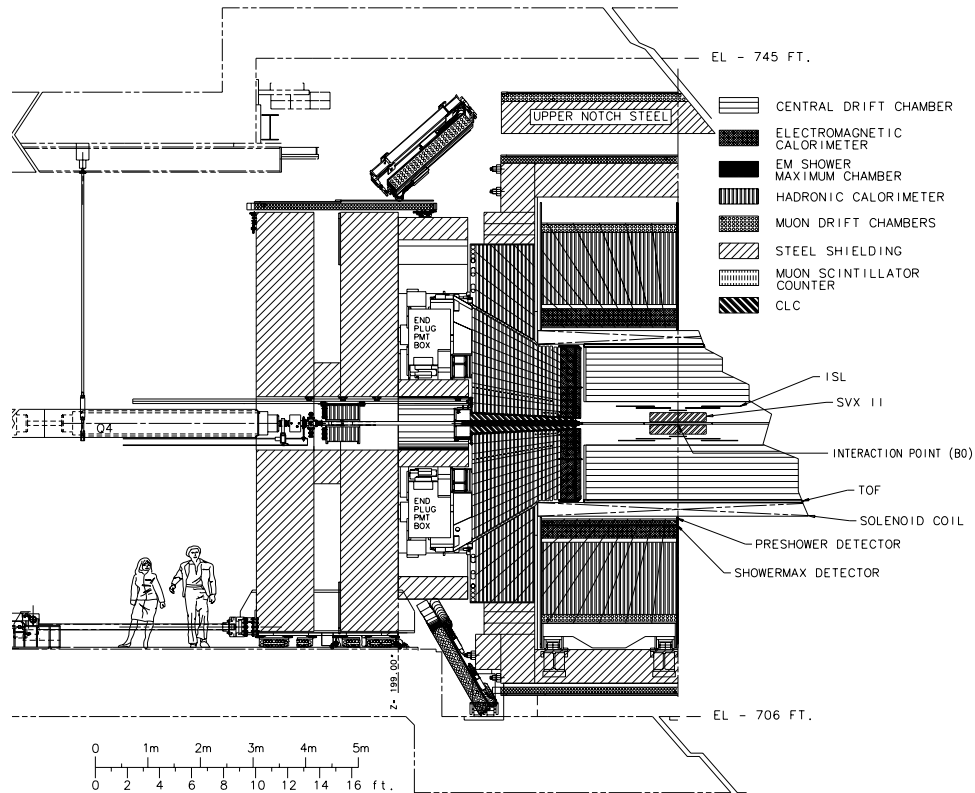


Figure 2.3. An elevation view of the CDF-II detector, showing the physical arrangement of tracking and calorimetry systems, the solenoidal magnet, shielding, and muon detection [7].

2.2 The Collider Detector at Fermilab

CDF-IIb – the Collider Detector at Fermilab – was a general-purpose particle detector, designed to identify and measure the properties of the final-state particles produced by proton-antiproton collisions at the full Tevatron energy of $\sqrt{s} = 1.96$ TeV. The detector was comprised of a collection of tracking systems which measured the momentum of charged particles and calorimetry systems which measured the energy of particle showers, arranged as a series of concentric cylindrical layers. The CDF-IIb detector is depicted in Figure 2.3.

The innermost layers were silicon charged particle detectors, designed for impact parameter resolution and precision tracking (the SVX and ISL layers). Surrounding this, a large open-cell drift chamber – the Central Outer Tracker or COT – provided

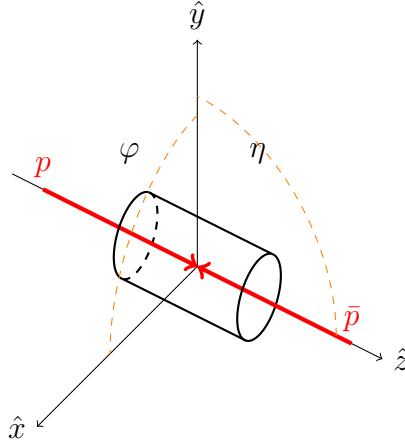


Figure 2.4. The CDF coordinate system as described in Section 2.2.1

long lever-arm measurements to resolve track momentum. Both of these systems were immersed in an axial 1.4 T magnetic field produced by a superconducting solenoid 1.5 m in radius and 4.8 m in length. Outside the magnet were electromagnetic and then hadronic calorimeters, segmented as wedges pointing to the IP. Preshower and shower maximum detectors colocated with the calorimeters provided identification of primary photons. Finally, muon detectors surrounding CDF's steel shielding detected any charged particles that the shielding did not absorb.

The remainder of this chapter will discuss each of these subsystems in detail.

2.2.1 Coordinate System

The geometry of the CDF-IIb detector naturally lends itself to the usage of a cylindrical coordinate system. The \hat{z} -axis runs parallel to the beam, through the center of the detector. It is positive in the proton flight direction (east). The radial coordinate r describes the distance from the beamline, and the azimuthal angle ϕ is defined such that north is 0° and up is 90° . The origin, $(r, z, \phi) = 0$, is the nominal interaction point B0 at the center of the detector (Fig. 2.4).

The topology of a scattering event – i.e. a pointlike collision resulting in long-lived relativistic debris travelling outward from the collision point – usually makes a form

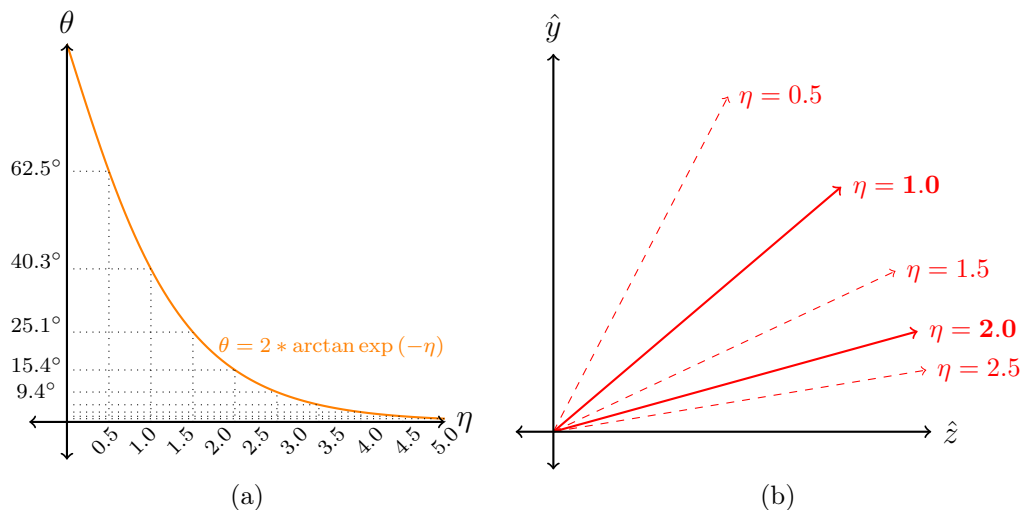


Figure 2.5. The relationship between the pseudorapidity η and the azimuthal angle θ . The functional dependence of $\theta = \theta(\eta)$ is shown in a, while the rays corresponding to several values of η are illustrated in b

of spherical coordinates a convenient tool. Instead of the usual polar angle θ it is customary to use the *pseudorapidity* (Fig. 2.5), related to the polar angle by

$$\eta = -\ln \tan \left(\frac{\theta}{2} \right). \quad (2.1)$$

With the pseudorapidity defined in this way, a particle travelling perpendicular to the beampipe has $\eta = 0$. The region with pseudorapidity $|\eta| \leq 1.0$ is referred to as the *central* region; from $1.2 \leq |\eta| \leq 2.0$ is the *plug* region. Pseudorapidities $\eta > 0$ are called *forward* and $\eta < 0$ are *backward*.

The plane defined by $\eta = 0$, e.g. the $(\hat{r}, \hat{\phi})$ plane, is called the *transverse plane*. Frequently we will refer to p_T , the component of a particle's momentum that lies in the transverse plane, defined as:

$$p_T = |\vec{P}| \cdot \sin \theta. \quad (2.2)$$

The pair (p_T, η) is often used as a concise summary of the most important prop-

erties of a final-state object. The particular utility of these two variables reflects a physical fact: when two hadrons (e.g., an antiproton and a proton) collide, the resultant processes are initiated by a parton-parton interaction with an unknown boost along the \hat{z} -axis. The pseudorapidity has the advantage over the polar angle that in the limit of massless or ultrarelativistic particles, it approaches the rapidity y and is thus invariant under boosts along \hat{z} . In fact, for a particle with known mass m , the rapidity may be recovered from η and p_T :

$$y = \frac{1}{2} \ln \left(\frac{E + p_z}{E - p_z} \right) = \ln \frac{\sqrt{m^2 + p_T^2} \cosh^2 \eta + p_T \sinh \eta}{\sqrt{m^2 + p_T^2}}. \quad (2.3)$$

The transverse momentum p_T is similarly \hat{z} -boost-invariant; furthermore, conservation of momentum requires that the vector sum of all particles' transverse momenta in a collision be zero.

2.2.2 Tracking

The path of a charged particle through the detector's tracking volume can be reconstructed from a collection of discrete position measurements ('hits'). The CDF-IIb detector utilized an integrated tracking system which combined small-radii measurements from extremely precise silicon tracking with large-radii measurements from an open-cell drift chamber, the Central Outer Tracker or COT (Fig. 2.6). The COT provided tracking in the region $|\eta| < 1.0$ while the silicon trackers extended coverage to $|\eta| \leq 2.0$. Integrated tracking optimizes overall performance while decreasing cost: high-precision (but expensive) silicon tracking near the IP allowed excellent resolution of a track's impact parameter, a feature of great utility, e.g. for b -tagging. On the other hand, the less-expensive wire tracking of the COT accommodated a large tracking volume and measurements with long lever-arm; this assists in resolving track curvature and consequentially p_T .

CDF Tracking Volume

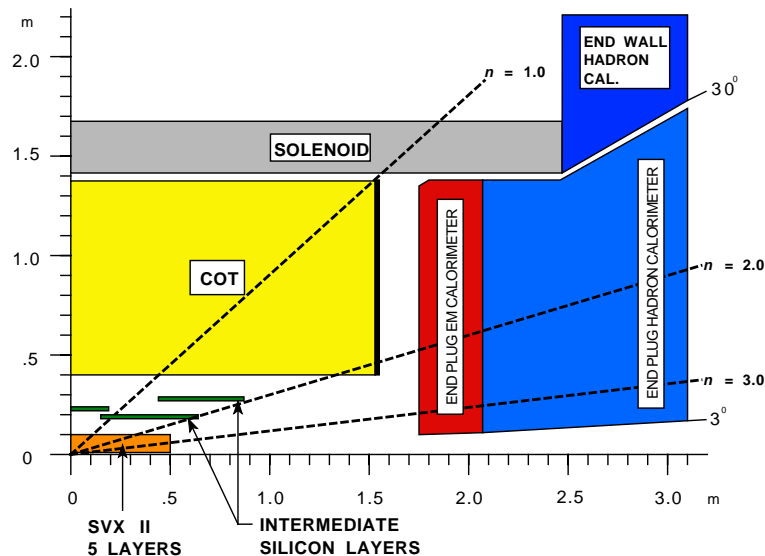


Figure 2.6. The CDF-II tracking volume. Shown are the superconducting solenoid, Central Outer Tracker, Intermediate Silicon Layers, and Secondary Vertex Detection. Layer 00 is not shown [8].

Solenoid

Precise determination of the momentum of a charged particle was accomplished through the measurement of its curvature in a magnetic field. At CDF, both the wire and silicon tracking systems were contained within a uniform 1.5 T magnetic field oriented parallel to the beamline. The field was produced by a solenoidal superconducting coil, 1.5 m in radius and 3 m in length. This coil was constructed from 1164 turns of extruded aluminum-stabilized NbTi/Cu superconducting wire. A thin aluminum alloy cylinder outside the coil counteracted the radially-outward forces of the magnetic field. Two-phase helium was pumped through an aluminum tube welded to this support cylinder for cooling [70].

Central Outer Tracker

The COT was a multiwire drift chamber. Drift chambers detect the passage of ionizing radiation via gas amplification: an electric field is applied across a gas-filled gap between two electrodes, and electrons from primary ionization within the gap are accelerated by the electric field, producing secondary ionization. The secondary ionization is collected by the electrodes. Precise measurements of the amplitude and timing of the resulting current pulse, along with knowledge of the electron drift velocity in the fill gas, allow inference of the distance between the anode and the site of the primary ionization. The design parameters for the COT are reproduced in Table 2.1.

The CDF Central Outer Tracker occupied the region $|\eta| \leq 1.0$ and $44 \text{ cm} \leq r \leq 132 \text{ cm}$. It consisted of a collection of drift cells arranged into eight radial superlayers, alternating between axial and stereo layers. Both primarily resolved r - ϕ position, but the wires of the stereo layers were tilted at $\pm 3^\circ$ degrees relative to the axial layers in order to provide some z -position information as well.

A single drift cell was comprised of 25 wires made from $40 \mu\text{m}$ gold-plated tungsten: 13 potential wires alternated with 12 sense wires. These were sandwiched between a pair of $6.35 \mu\text{m}$ gold-on-mylar cathode sheets. The assembly was filled with a 50:50 mixture of Ar – Et, having a drift velocity of about $56 \mu\text{m ns}^{-1}$ in a field of

Table 2.1. Design parameters for the CDF-II Central Outer Tracker [7].

Radial coverage	44 – 132 cm
Number of superlayers	8
Measurements per superlayer	12
Readout coordinates of SLs	$+3^\circ \ 0 \ -3^\circ \ 0 \ +3^\circ \ 0 \ -3^\circ \ 0$
Maximum drift distance	0.88 cm
Resolution per measurement	$180 \mu\text{m}$
Rapidity coverage	$ \eta \leq 1.0$
Number of channels	30, 240
Material thickness	$1.3\% X_0$

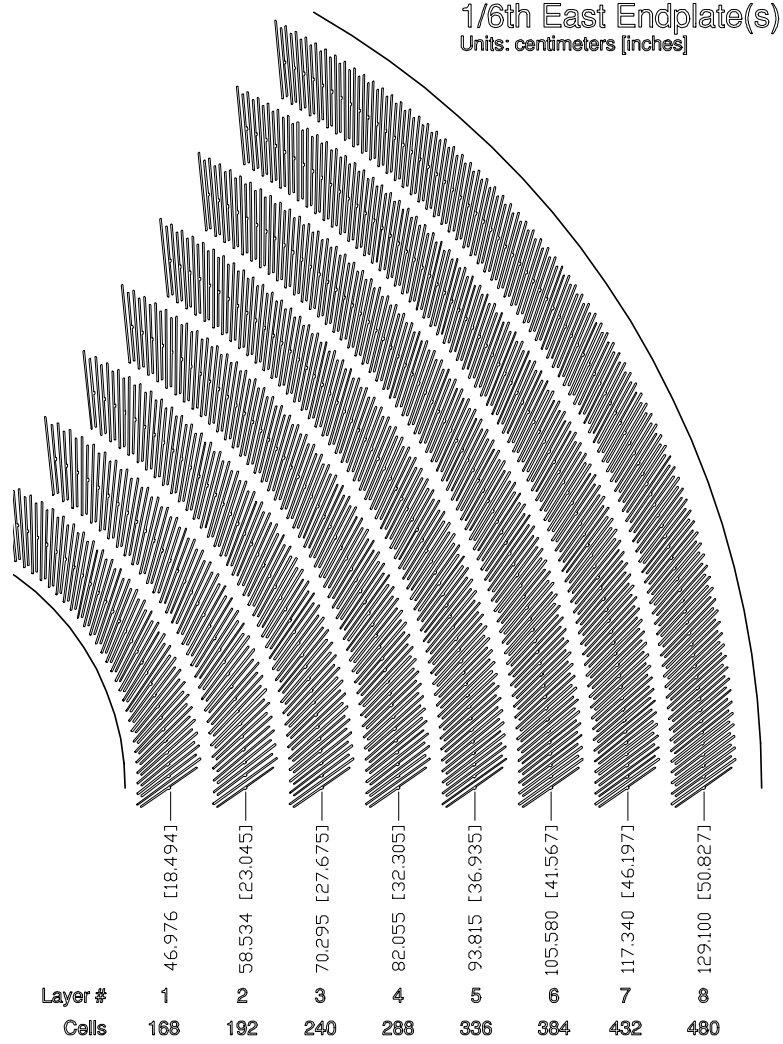


Figure 2.7. The east endplate of the Central Outer Tracker. The long slots located the gold-on-mylar cathode sheets which separate adjacent cells, while the short, keyed slots locate the wire plane of an individual cell [8].

2.5 kV cm^{-1} . Ionization in the $\simeq 2 \text{ cm}$ cells therefore had a maximum drift time of 177 ns , comfortably within the 396 ns Tevatron bunch spacing [8, 71].

The cells were terminated on a pair of precision-milled endplates, constructed of 4.1 cm -thick 6061-T561 aluminum. Each cell was tilted at a 35° angle relative to the radial direction (Fig. 2.7). This compensated for the effect of $\overline{E} \times \overline{B}$ drift on the electron trajectory, which otherwise would cause loss of drifting charge near the ends of a drift cell. As the wires and sheets run horizontally, they required tension to avoid

excessive sag – individual wires were tensioned at 135 g and sheets at 9.98 kg. The resulting total load on the endplates was in excess of 3.7×10^4 kg. The wires also had additional supports midway between the endplates to counteract the effects of electrostatic repulsion.

Due to the radial taper of a drift cell, small variations in the wire voltage across a cell were necessary to maintain a uniform electric field. For the highest-taper cells (the innermost superlayer), this was at most $\simeq 200$ V. With 25 wires per cell and 8 superlayers, 200 high-voltage (HV) channels were required for the COT. These were produced by VME-based pods located in the CDF counting room. A 1:4 fanout individually supplied each quadrant of each superlayer through 800 RG-58 coaxial cables. After filtering, the HV was distributed to the COT wires through the endplate opposite the readouts. Each sense wire and each potential wire was attached to the corresponding HV bus with a capacitor and feed resistor. Sense wires also had termination resistors to prevent reflected signals [8].

In total, the COT had 30,240 channels: 16,128 axial channels and 14,112 stereo channels. Amplification, pulse shaping and discrimination – that is, all necessary analog signal processing – were accomplished on the endplate using a custom Amplifier/Shaper/Discrimination (ASD) chip. These provided both timing and charge information, to distinguish particles by dE/dx . The resulting differential signals were carried to Time-to-Digital Conversion (TDC) boards mounted in a VME crate on the chamber walls. Each TDC board handled 96 sense wire channels and contained sufficient buffering for both Level 1 and Level 2 triggering. TDC auxiliary cards latched hits for the eXtremely Fast Tracker (XFT) triggering system [7]. Triggers and the XFT will be discussed in more detail in Section 2.2.5.

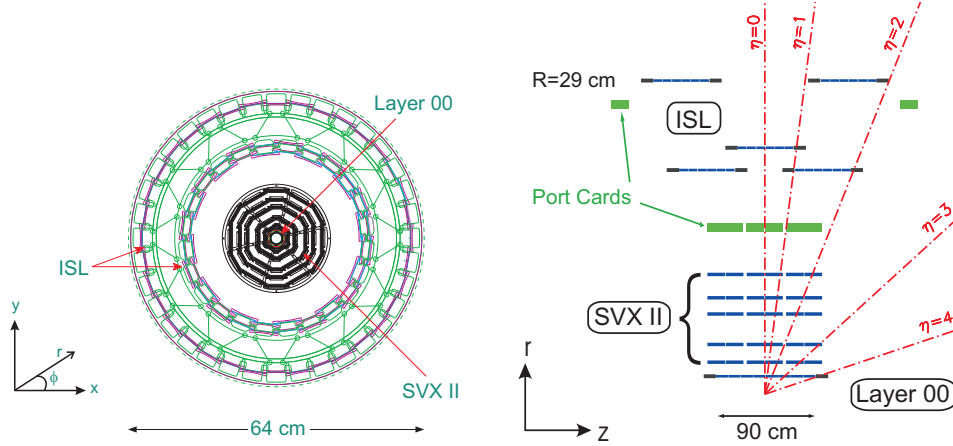


Figure 2.8. The layout of the CDF silicon tracking system. Layer 00 (L00) is closest to the beampipe, surrounded by the SVX layers and the associated Port Cards. Outside both of these are the Intermediate Silicon Layers (ISL) and the ISL Port Cards. Note that the z -axis is compressed for convenient illustration [9].

Silicon Tracking – SVX and ISL

The precision inner tracking system at CDF was constructed from double-sided silicon microstrip charged particle detectors. Silicon detectors operate by reverse-biasing a silicon p - n junction with a voltage sufficient to ensure full depletion. The ionization created by charged particles passing through the bulk silicon induces small (but measureable) ionization currents across the junction. Modern lithographic techniques allow the creation of many such junctions on a single large wafer of silicon, with very tight spatial tolerances.

The silicon tracking system was divided into three subsystem: Layer 00 (L00) and the Silicon VerteX Detector (SVX) provided impact parameter resolution and vertex detection, and the Intermediate Silicon Layers (ISL) provided standalone tracking extending to $|\eta| \leq 2.0$. Although conceptually similar, due to the distinct (and rather more severe) mechanical constraints for L00 and the SVX layers, they are most readily treated as separate from the ISL layers [8]. The very small-radius L00 existed to alleviate limitations on impact-parameter resolution otherwise caused by multiple-scattering in the non-active material in the SVX layers [9]. Design parameters for

Table 2.2. Design parameters for the CDF-II Secondary Vertex Layers [8].

Radial coverage	2.4 – 10.7 cm, staggered quadrants
Number of layers	5
Readout coordinates	r - ϕ on one side of all layers
Stereo side	r - z , r - z , r - uv , r - z , r - uv ($uv \equiv 1.2^\circ$ stereo)
Readout pitch	60 – 65 μm (r - ϕ); 60 – 150 μm (stereo);
Total length	96.0 cm
Rapidity coverage	$ \eta \leq 2.0$
Number of channels	405, 504
Material thickness	3.5% X_0
Power dissipated	1.8 kW

these three subsystems are shown in Tables 2.2 and 2.3, and the physical arrangement in Figure 2.8.

Silicon detector crystals and the associated readout ASICs were assembled into ‘ladders’ – a beryllium substrate and carbon/boron fiber support rail with two silicon detector assemblies on either side. Twelve ladders arranged in a ring formed a layer; the SVX system used five double-sided layers having radii $2.4 \text{ cm} \leq r \leq 10.7 \text{ cm}$. The 96 cm length was divided into three 32 cm ‘barrels’, each of which had a 29 cm active length. A barrel was terminated on either end by a pair of precision-machined beryllium bulkheads (Fig. 2.9). These bulkheads also included machined channels for cooling the attached ladders. Layer 00, which had only a single side, was located immediately outside the beampipe at a radius of 1.6 cm [72].

The SVX system used both small-angle stereo layers (L2 and L4, at $\pm 1.2^\circ$) as well as 90° stereo layers (L0, L1, L3). The 90° stereo layers were constructed from ladders with an r - ϕ readout on one side and r - z on the opposite. Small-angle stereo layers had an r - ϕ layer paired with a stereo layer tilted at 1.2° [8].

To take proper advantage of the precision of silicon tracking systems, extremely tight spatial tolerances were required for all mechanical components. The two silicon crystals on a ladder side were located during ladder assembly with the aid of a

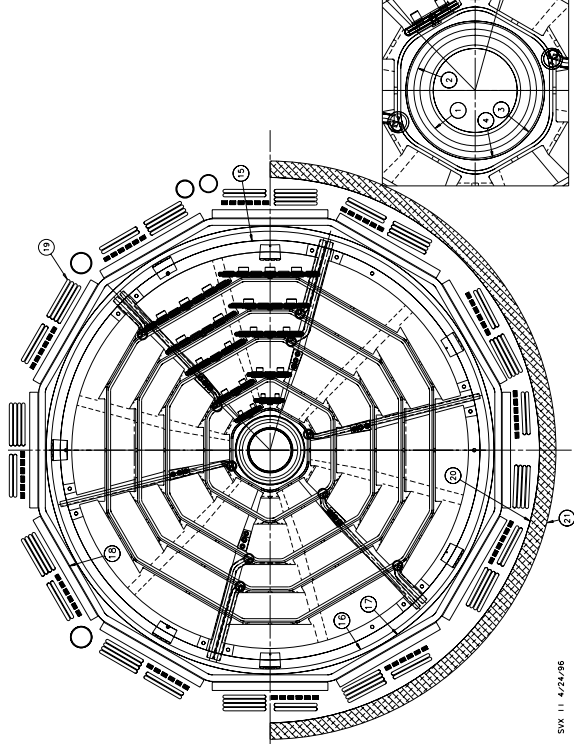


Figure 2.9. The SVX-II bulkhead design. The bulkhead is constructed from precision-machined beryllium, and locates 60 silicon microstrip ‘ladders’ arranged in 12 wedges and 5 layers [8].

precision coordinate measurement machine. Locking pins affixed the ladders to the barrel bulkheads with a repeatability of $\pm 3\ \mu\text{m}$. The barrel axis required alignment to within $\pm 100\ \mu\text{rad}$ of the beam direction, corresponding to a relative placement of $\pm 25\ \mu\text{m}$ for the barrel ends. This was accomplished by mounting the barrels into a rigid carbon-fiber spaceframe, which was positioned at installation and adjusted during commissioning by moving the detector. Beam steering was used to maintain alignment while operating.

The best impact parameter resolution is obtained when the measurements from the inner silicon detectors are anchored to tracks measured at larger radius. In the central region ($|\eta| \leq 1$), this may be accomplished by integration with the COT. The COT, however, is sensitive to the overall occupancy of the detector and provides no coverage in the forward regions. Both of these issues were addressed by inserting

Table 2.3. Design parameters for the CDF-II Intermediate Silicon Layers [8, 9].

Radial coverage		20 – 28 cm
Number of layers		1 for $ \eta < 1$; two for $1 < \eta < 2$
Readout coordinates	r - ϕ and r - uv (1.2° stereo) (all layers)	
Readout pitch		110 μm (axial); 146 μm (stereo)
Resolution per measurement		16 μm (axial)
Total length		174 cm
Rapidity coverage		$ \eta \leq 1.9$
Number of channels		303, 104
Material thickness		2% X_0

additional silicon tracking between SVX and the COT. In the central region this took the form of a single ISL layer at a radius of 22 cm. In the region $1.0 \leq |\eta| \leq 2.0$, two ISL layers at radii 20 cm and 28 cm provided stand-alone tracking independent of the COT.

The Intermediate Silicon Layers were in most ways very similar to the SVX small-angle stereo layers. Several simplifications helped both to accommodate the large required silicon area and best take advantage of the lower occupancy, reduced radiation damage and loosened positional tolerances which accompany the larger radius. ISL layers used longer strips with larger pitch, and ladders had three wafers instead of two. The ladders were supported by lightweight carbon-fiber bulkheads, which were able to maintain a $\pm 180 \mu\text{m}$ tolerance between opposite ends of an ISL layer.

All of the silicon systems shared a common biasing and readout design. The silicon detectors initially required a bias voltage of 70 V to achieve full depletion. This increases with accumulated radiation-induced bulk damage, necessitating separate bias supplies for each layer. Each wedge of each layer was powered by a single power supply module located in a crate on the detector end wall. The power supply modules provided separate biasing voltage for each layer (up to +200 V) along with +5 V power for the front-end electronics.

In total the silicon system had 722,432 channels: 13,824 for L00, 405,504 chan-

nels for SVX, and 303,104 for ISL. Front-end ASICs (SVX3FE and SVX3BE) were located directly on the ladders. Each provided amplification and charge integration for 128 channels along with a $16.5\ \mu\text{s}$ pipeline to buffer events for the Level-1 triggers. Several (4-14) SVX3 chipsets were serviced by a Port Card (PC) and Fiber Interface Board (FIB) which handled initialization, calibration and interfacing. Each FIB was connected to a VME Readout Buffer (VRB), which were aggregated in VME crates. The VRBs provided buffering for events awaiting Level-3 readout as well as events destined for the Level-2 trigger systems, most importantly the Silicon Vertexing Trigger (SVT). A Silicon Readout Controller (SRC) module provided a clock to the silicon system and supervised triggering and readout [8].

An improved silicon tracking system was designed for the CDF-IIb upgrade (Ref. [7, 73]), but due to funding constraints the project was abandoned before the system could be constructed. Instead, the silicon system from Run IIa was operated throughout the entirety of Run II. Initially designed only for an integrated luminosity of $2 - 3\ \text{fb}^{-1}$, the original silicon system was successfully operated through a total delivered luminosity of $12\ \text{fb}^{-1}$. To moderate the effects of radiation damage, the operating temperature during Run II-b was lowered to $-10\ ^\circ\text{C}$ for L0/SVX and $6\ ^\circ\text{C}$ for ISL and the Port Cards. However, by the end of Run II the accumulated radiation damage was still such that roughly one-third of L0 was no longer operating in a fully-depleted state. For the most damaged sensors, the required operating voltage had risen to 165 V, and was limited to that level only to mitigate the risk of catastrophic damage. Fortunately, the resulting degradation was not severe enough to impact overall silicon performance more than a small amount [9].

2.2.3 Calorimetry

Outside the solenoid, sampling calorimeters consisting of alternating layers of absorber and scintillator provided measurements of the outward flow of energy in a

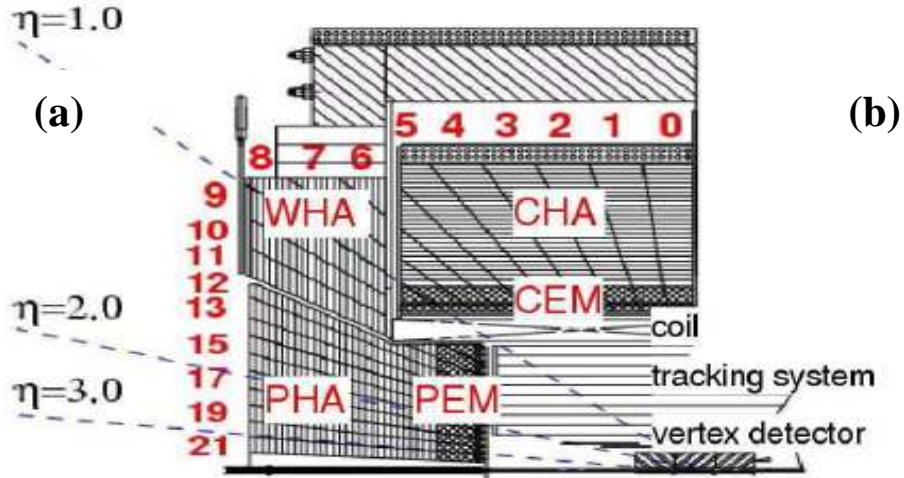


Figure 2.10. The CDF calorimeters. The CEM and PEM calorimeters measure the energy of electromagnetically-interacting particles, while CHA, PHA and WHA measure the energy of strongly-interacting particles [10].

collision. Incident particles interact with the absorber layers and produce cascading showers of lower-energy secondary particles. Scintillator material sandwiched between absorber layers converts a portion of the shower energy into light, which was collected by photomultiplier tubes (PMTs) and converted into an analog signal for readout. Unlike charged particle tracking, calorimetry is a destructive measurement: the energy of the incident particle is mostly or fully absorbed in the calorimeter. Also unlike tracking, calorimetry is sensitive to photons and neutral hadrons.

The CDF calorimeters were segmented into wedges pointing toward the nominal interaction point ('towers'). There were 24 azimuthal divisions of $\Delta\phi = 15^\circ$ and 22 axial divisions of $\Delta\eta \approx 0.15$. Calorimeters that measured the energy of electromagnetically-interacting particles (EM) are located just outside the solenoid. These were surrounded by separate calorimeters that measure the energy of strongly-interacting particles (HAD). In total, five subsystems covered the range $|\eta| \leq 3.0$: CEM and CHA provided electromagnetic and hadronic calorimetry in the central region, PEM and PHA in the plug region, and WHA filled the gap in hadronic

calorimetry in the endwall region between the PHA and CHA calorimeters (Fig. 2.10). Table 2.4 compares the designs of the central and plug calorimeters [8].

All calorimeters were photomultiplier-based and shared a common set of electronics. VME cards ('ADMEM') contained custom current-integrating ADCs, charge-injection calibration circuitry and trigger buffering. Each card could service up to twenty photomultipliers, and provided the summed value of the PMT amplitudes to the Level-1 triggering system. Readout occurred through the VME backplane bus via VME Readout Controllers ('VRC') [74].

Electromagnetic Calorimeters

The preferred absorber materials for electromagnetic calorimeters are elements with high nuclear charge Z . Energetic electrons and photons interact with the absorber primarily through pair production and Bremsstrahlung, both of which are substantially enhanced in high- Z absorbers ($\propto Z^2$). These materials then have a characteristically short radiation length X_0 (the distance over which the deposited energy is $\delta E/E = 1/e$), allowing easy confinement of EM showers in a moderate volume. Lead, used in the CDF calorimeters, is an effective choice with a reasonable cost.

The EM plug calorimeters were constructed from 23 layers, each of which had 4 mm lead and 4.5 mm of plastic scintillator. Wavelength-shifting fibers embedded in the scintillator matched the scintillator output to the sensitive wavelengths of the PMTs. These were spliced to clear fibers which carried the output signal to the PMTs, located on the outside plane of each endplug [8]. The overall resolution was $\delta E/E = 16\%/\sqrt{E} \oplus 1\%$, dominated by the statistical variation on the sampling fraction, i.e. the fact that some portion of the shower energy is deposited in lead rather than scintillator [10].

The central EM calorimeters were constructed similarly. Here there were 19 layers,

Table 2.4. Comparison of design parameters for the CDF-II central and plug calorimeters [7].

	Central	Plug
Electromagnetic		
Thickness	$19X_0, 1\lambda$	$21X_0, 1\lambda$
Sample (Pb)	$0.6X_0$	$0.8X_0$
Sample (scint.)	5 mm	4.5 mm
WLS	sheet	fiber
Light yield	160pe/GeV	300pe/GeV
Sampling res.	$11.6\%/E_T$	$14.0\%/E_T$
Stoch. res.	$14.0\%/E_T$	$16.0\%/E_T$
SM size (cm)	$1.4\phi \times (1.6 - 2.0) Z$	$0.5 \times 0.5IV$
Pre-shower size	$1.4\phi \times 65Zcm$	by tower
Hadronic		
Thickness	4.5λ	7λ
Sample (Fe)	1 in. C, 2 in. W	2 in.
Sample (scint.)	10 mm	6 mm
WLS	finger	fiber
Light yield	$\simeq 40pe/GeV$	$39pe/GeV$

with 3 mm of lead and 5 mm scintillator. Wavelength-shifting was performed by sheets on the side of each tower, and routed via acrylic light-pipes to PMTs on the outside edge [8]. The resolution of the CEM calorimeters was $\delta E/E = 14\%/\sqrt{E} \oplus 1\%$ [10]. Preshower detectors (thin lead sheets with scintillating tile detectors) located just inside the central EM calorimeters are used to help distinguish photons which usually shower immediately from neutron pions which do not [75]. Additionally, a ‘Shower Maximum’ wire chamber, the CES, located at a depth of $6X_0$ measures the lateral shower profile to extract position and amplitude information. This aids in rejecting early hadronic showers which begin in the EM calorimeters [76].

Hadronic Calorimeters

The more penetrating hadrons are in general only somewhat attenuated by the EM absorbers. The hadronic interaction length λ is a function of the absorber density, but does not exhibit the Z^2 dependence which is characteristic of EM interactions.

As a result, λ is typically an order of magnitude or more greater than the EM radiation length in high- Z materials. The full thickness of the CDF electromagnetic calorimeters corresponds to only 1λ . Hadronic calorimeters must be physically large to fully contain the hadronic shower. Steel, about 70% the density of lead, is nearly as effective an absorber for hadrons and much lower in cost.

The plug hadronic calorimeters alternated 6 mm scintillator layers with 5.08 cm steel slabs. Like the plug EM calorimeters, wavelength-shifting fibers embedded in the scintillator were spliced to clear fibers which carried signals to PMTs on the outside calorimeter wall. The sampling fraction, which is lower for hadronic calorimeters than EM calorimeters, limited the resolution to $\delta E/E = 70\%/\sqrt{E} \oplus 4\%$ [10].

The central hadronic calorimeters (CHA) used 2.54 cm steel and 10.0 mm scintillator layers for an overall resolution of $\delta E/E = 33\%/\sqrt{E} \oplus 4\%$. The wall calorimeters (WHA) used larger 5.08 cm steel absorbers due to the higher overall occupancy in the more-forward regions of the detector. Both shared the acrylic light-pipe and photomultiplier architecture of the CEM calorimeter [77].

2.2.4 Muon Detection

The outermost layer of the CDF-II detector was a set of four muon detection systems which provided coverage of the range $|\eta| \leq 1.5$. Much of the interesting physics that was accessible at Tevatron energies results in the production of energetic, near-minimum-ionizing muons. These typically escape the detector, interacting minimally with any intervening materials. As such, muons are readily identifiable: any charged particle which penetrates a sufficiently thick absorber is most likely a muon.

The absorbers for the four muon subsystems were the calorimeter steel (CMU), the magnet return yolk (CMP/CSP), additional steel walls (CMX/CSX), and the steel from the Run I forward muon toroids (IMU). The last of these is not used for triggering in this analysis and will not be discussed further. Design parameters for

Table 2.5. Design parameters for three of the four CDF-II muon detection subsystems (IMU is not shown). Pion interaction lengths and multiple scattering assume a reference angle of $\theta = 90^\circ$ in CMU and CMP/CSP and an angle of $\theta = 55^\circ$ in CMX [7].

	CMU	CMP/CSP	CMX/CSX
Pseudo-rapidity coverage	$ \eta \leq \sim 0.6$	$ \eta \leq \sim 0.6$	$\sim 0.6 \leq \eta \leq \sim 1.0$
Drift tube cross-section	2.68×6.35 cm	2.5×15 cm	2.5×15 cm
Drift tube length	226 cm	640 cm	180 cm
Max drift time	800 ns	1.4 μ s	1.4 μ s
Total drift tubes	2304	1076	2208
Scintillation counter thickness		2.5 cm	1.5 cm
Scintillation counter width		30 cm	30 – 40 cm
Scintillation counter length		320 cm	180 cm
Total counters		269	324
Pion interaction lengths	5.5	7.8	6.2
Minimum detectable muon p_T	1.4 GeV/c	2.2 GeV/c	1.4 GeV/c
Multiple scattering resolution	12 cm/p	15 cm/p	13 cm/p

the remaining three systems are shown in Table 2.5.

Each muon system was constructed from several layers of single-wire drift cells, filled with an approximately 50:50 argon-ethane mixture and small ($< 1\%$) amounts of isopropyl alcohol. The multilayer construction allowed the muon system to aggregate hits into short ‘stub’ tracks which could be matched by the triggering system to a corresponding track from the central tracking system, or included in offline track fitting to improve overall muon resolution.

The directional character of muon stubs aids in rejecting backgrounds, which are likely to form a track that does not extrapolate back to the interaction point. The CMP and CMX wire chambers also had associated fast scintillator counters (CSP and CSX, respectively), which aided in rejecting out-of-time backgrounds. These features allowed muon hits to be associated with the correct bunch crossing, as the (relatively long) maximum drift time of the muon chambers spanned multiple crossings.

Central Muon Detector (CMU)

The CMU was constructed from 144 modules, each of which contains 16 cells. Each 226 cm cell had a 50 μm stainless wire in the center, operating at 2.5 kV. Field shaper cathodes operated at -2.3 kV . The cells were stacked 4 deep in the radial direction, with the odd layers having a small offset in ϕ relative to the even layers. A TDC measured the ϕ location of a wire hit, while ADCs attached to each end utilized charge sharing to measure the z location [7].

Central Muon Upgrade (CMP)

The CMP was a second set of muon chambers in the central region behind an additional 60 cm of steel. Above and below the detector, this steel was the magnetic return yolk. Retractable walls served as shielding on the two sides. The chambers were arranged as a box around the central detector, and consequentially the rapidity coverage varied in ϕ . Like CMU, the CMP had four layers with half-cell staggering of alternate layers. Anode wires operated at 5.6 kV and field shapers at 3 kV. A single TDC read out each wire. Additionally, a scintillator counter (CSP) was installed on the inside surface of the CMP. Each rectangular scintillator counter covered two CMP cells in width and one-half of a CMP cell in length, and was read out by phototubes in the center of the array [7].

Central Muon Extension (CMX)

The Central Muon Extension was shaped as a pair of conic sections in the region $0.6 \leq |\eta| \leq 1.0$. Each 15° sector in ϕ had 8 layers of twelve tubes each. The 8 physical layers were grouped into 4 logical layers, each of which consisted of two layers with a small offset in ϕ . Logical layers were alternately offset by a complete half-cell in ϕ . Wires operated at 5.4 kV and field shapers at 2.8 kV. Four layers of trapezoidal CSX scintillation counters were installed on both the inner and outer surfaces of each

sector. Scintillators were read out by single phototubes located on opposite ends for the inner and outer layers [7].

2.2.5 Triggers

The 2.5 MHz Tevatron bunch-crossing rate resulted in a 1.7 MHz event rate after accounting for abort gaps. If every crossing were to be read out, the result would be a tremendous data set consisting almost entirely of uninteresting events. More importantly, it would far exceed the ~ 150 Hz rate at which events could be recorded. To cope with this limitation, CDF used a three-level trigger system (Fig. 2.11) to select potentially interesting rare events from the enormously larger number of minimum-bias events. Each trigger level successively reduced the event rate to a sufficient degree to allow for more sophisticated processing in the subsequent level [8].

The Level-1 triggering system used custom hardware to identify physics objects based on a limited, local subset of the detector channels. About 1 in 500 events were retained, reducing the rate to ~ 35 kHz. Upon Level-1 accept, the frontend electronics moved the event into one of four onboard Level-1 buffers. The Level-2 triggers performed a partial event reconstruction in custom, programmable hardware and further reduced the rate to < 1 kHz. Upon Level-2 accept, data from accepted events was read out and assembled by the Event Builder (EVB). The complete event was then passed to the Level-3 triggering system, implemented in software using full event reconstruction on a processor farm. The entire trigger system was pipelined to allow for event processing with minimal deadtime. It retained approximately 1 in 11,000 events overall for a final event recording rate of 150 Hz [9].

Level-1 Triggering

The Level-1 triggering system was a 40-stage pipeline constructed from three parallel processing streams, each of which located objects in a major detector subsystem:

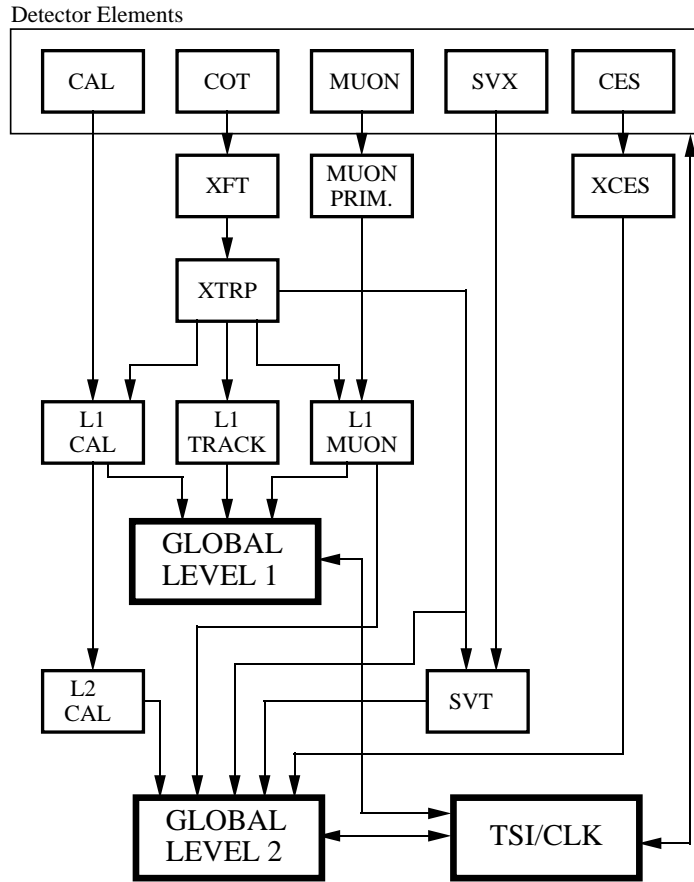


Figure 2.11. The CDF triggering architecture. Three trigger levels successively reduce the event rate from the 1.7 MHz bunch crossing rate down to the 150 Hz at which events can be written to tape [8, 11]. Shown here are the Level-1 and Level-2 triggering systems. Level-3, which is implemented entirely in software, is not displayed.

the calorimeter, the muon detectors, and the COT. These streams were merged in a global Level-1 decision unit, which issued a Level-1 accept to the frontend electronics. The decision to retain an event was based on either object triggers – the numbers of electron, muon, jet and photon candidates as well as their energy – or global calorimeter triggers [8].

The Level-1 track processor – the eXtremely Fast Tracker (XFT) – provided 2-d tracks (track ϕ and curvature sign) to each of the three Level-1 streams. ‘Finder’ modules processed the hit data from a single COT superlayer in slices of $\delta\phi = 30^\circ$.

Track segments were identified by attempting to match hits to predefined patterns corresponding to physical tracks with $p_T > 1.5 \text{ GeV}/c$. The resulting segments were passed to ‘Linker’ modules, which similarly used predefined patterns to attempt to join collections of segments into tracks. Stereo track-finding occurred simultaneously, although at Level-1 this information was only available to set a single flag to mark a given 2-d track as ‘stereo-confirmed’ or not [78].

A collection of fast hardware modules (the XTRP system) extrapolated the tracks from the XFT into the other regions of the detector and fanned out track information to all three Level-1 streams. The Level-1 track trigger used *only* this information; it was important for accepting events which might be of interest to the Level-2 SVT trigger. For the muon triggers, extrapolated track information allowed the construction of muon candidates by matching muon stubs to tracks. In the case of the calorimeter triggers, it allowed enhanced identification of electron candidates by matching tracks to EM-dominated calorimeter towers.

At this stage of processing, no clustering of calorimeter towers was performed. Instead, calorimeter objects were simply towers with energy deposits exceeding a certain threshold. However, some aggregate values were both readily computed and of much utility for triggering. These are the global trigger quantities. First, the sum of all calorimeter transverse energies ($\sum E_T$) allowed the retention of events with large total energy. Second, the vector sum of tower energies allowed the Level-1 decision to incorporate information about the imbalance of transverse energy flow (E_T^{miss} , detailed further in Sec. 3.6). This aided in selecting events which might contain a (undetectable) neutrino or exotic particles that might not interact with detector material.

Level-2 Triggering

The Level-2 triggers were implemented using a combination of custom hardware and a programmable CPU for global L2 decision-making. In addition to the Level-1 trigger objects, information was available from the silicon displaced-vertex reconstruction (SVT [79]), the Level-2 calorimeter reconstruction (L2CAL [80]), and ShowerMax cards that measured the lateral shower position in the EM calorimeter (CES/XCES). A stereo extension to the XFT system allowed for 3-d track reconstruction at Level-2 [78].

Much of the custom Level-2 trigger hardware was implemented using 9U VME ‘Pulsar’ boards. Each of these boards integrated three Field-Programmable Gate Arrays (FPGA) for trigger processing: a pair of data FPGAs which interfaced to two I/O mezzanine cards each, and a control FPGA for additional processing. Offloading the I/O to a mezzanine card allowed the Pulsar board to act as a universal interface board for the CDF Level-2 triggering system, even with the individual detector subsystems having a diverse set of electrical and data-format specifications [81].

The Level-2 calorimeter trigger performed simple jet clustering using the full 10-bit resolution of both the HAD and EM calorimeters. A collection of Pulsar boards arranged as two stages merged the 288 calorimeter channels into a single stream before sending it to the Level-2 trigger processor CPU. There, towers with E_T above a programmable threshold were selected as cluster seeds. Using all towers within a fixed radius of the seed in η - ϕ , jet energy was computed as a simple sum of tower energies. Jet direction was computed as a weighted mean with the tower E_T as weight. Electron and photon clustering were performed similarly, and both E_T^{miss} and $\sum E_T$ were recomputed with improved precision [80].

3-d track information from the XFT Stereo Finder modules was fully available at Level-2. The stereo XFT system utilized a sparse readout system: segments from the XFT Stereo Linkers were read out only in the vicinity of specified regions of interest,

i.e. stereo-confirmed axis-traversing 2-d tracks. Pulsar boards merged the data from the XFT Stereo Linker modules before the Level-2 trigger processor CPU. There, a fast track-linking and reconstruction algorithm produced tracks in software with a z_0 resolution of 11 cm and ϕ resolution of 0.13 cm [78].

The SVT trigger exploited the naturally massively-parallel readout of the silicon inner detector systems to quickly fit tracks with extremely high r - ϕ precision. This allowed sufficient impact parameter resolution to identify the displaced vertices that are characteristic of long-lived b -mesons, substantially improving the acceptance for physics involving b -quarks. To perform precision pattern recognition in such a short time, parallel track reconstruction was combined with very fast Associated Memory (AM++) chips and FPGAs. The first processing stage used FPGAs to convert lists of channel numbers and pulse heights from the silicon detectors into charge-weighted centroids. Hits in each plane were binned into ‘superstrips’ of 250 – 700 μm width.

A collection of AM++ chips formed a very fast pattern look-up table. The full list of binned hits in a 30° silicon wedge was presented to each of 64 AM++ chips, housed on a pair of carrier boards. Each AM++ chip could store up to 5120 patterns. The entire SVT system encoded 512K distinct patterns per wedge. Once all hits were read, an encoder listed all patterns – known as ‘roads’ – for which all of the five SVX layers had a matching hit. Track Fitters perform refined track fitting from the roads identified by the associative memory, and Hit Buffers stored the hits associated with a track. Both of these were constructed from Pulsar boards. The entire SVT system required over 150 VME boards, distributed amongst 10 VME crates on 6 racks [9, 79].

The output from these systems, as well as the Level-1 triggering information, was then passed to the software component of the Level-2 trigger. Six Pulsar boards acted as sinks for the various Level-2 triggers:

- *Muon Rx* aggregated muon information and XFT tracks.
- *Calo Rx* received both Level-1 tower and energy sum information as well as

Level-2 calorimeter clusters.

- *SVT Rx* received information from the SVT subsystem.
- Three *ShowerMax Rx* boards interfaced to the CES/XCES ShowerMax system.

Two additional Pulsar board merged all but the SVT streams. The output from the final merge and from the SVT trigger were fed separately into the global Level-2 decision node. This was a commodity dual-core PC running Linux with real-time scheduling, which received data from the dedicated trigger hardware via S-LINK using a pair of commercial PCI interface cards. Trigger decisions (as well as other trigger information) were sent using a third S-LINK interface to yet another Pulsar board, which distributed the result to the Trigger Supervisor (TSI) and CDF data acquisition system [81].

Level-3 Triggering and Data Acquisition

The Level-3 triggering system at CDF was implemented entirely in software on a farm of 256 commodity PCs running Linux. The reconstruction algorithms were consistent with (but faster and less accurate than) those used in the offline reconstruction. For this reason they will not be discussed in detail here, although the offline reconstruction algorithms will be described in Chapter III. The Level-3 farm communicated through an ATM switch, to which also was attached the Event Builder (EVB), responsible for aggregating data from the readout system. The trigger processors were grouped into 16 sub-farms. Each of these had a converter node, 16 processor nodes, and an output node. Events which passed the Level-3 selection were archived to a tape library for permanent storage and offline analysis [82].

CHAPTER III

Offline Reconstruction and Object Identification

The accelerator complex and particle detectors described in the previous chapter are capable of producing and recording proton-antiproton collisions in extreme detail. The resulting measurements, however, are performed on the stable remnants of a physical process that has usually already undergone several stages of decay. It is necessary to reconstruct the preceding stages in order to access most of the physics of interest.

This chapter describes the manner in which the low-level measurements made by the detector lead to particle tracks, leptons, and jets. The utility of missing transverse energy (E_T^{miss}) is discussed, as is the powerful technique of b -tagging.



Figure 3.1. The chapter headpiece.

3.1 Data Handling

A ‘run’ at CDF was a contiguous block of time during which the detector was active and recording data. A Tevatron store for physics use entailed at least one CDF run; however, in the event that the detector malfunctioned or components required reinitialization, a single store might include several CDF runs. Depending on the time spanned and the instantaneous Tevatron luminosity, a given run may contain anywhere from several to several million recorded events. Each run was assigned a unique ‘run number’ to identify it. At the end of a run, a flag was set for each detector component to indicate the portion of the run during which that component was operating properly. Not every physics need requires every detector subsystem, so this maximizes the amount of usable data available for a given purpose. In the present work, for example, this allows the use of runs in which only a subset of the lepton triggering systems were functioning.

The most precise event reconstruction occurred asynchronously with data-taking. Several large computing centers, both at Fermilab and offsite, provide extensive grids of commodity CPUs which are suitable for the mass parallel processing of detector data. Raw data from the detector is stored in a tape library during data-taking as described in Chapter II. After the completion of a run, offline reconstruction jobs running on grid computing resources read the raw data back from tape and apply accurate (but slow) algorithms to parametrize tracks, vertices, and calorimeter clusters. These objects form the basis of most subsequent physics analysis.

3.2 Track Reconstruction

The homogenous magnetic field of the CDF tracking system causes charged particles to follow helical paths with axes parallel to the magnetic field ($-\hat{z}$). Such a helix may be fully described with five parameters. At CDF, the chosen parameters

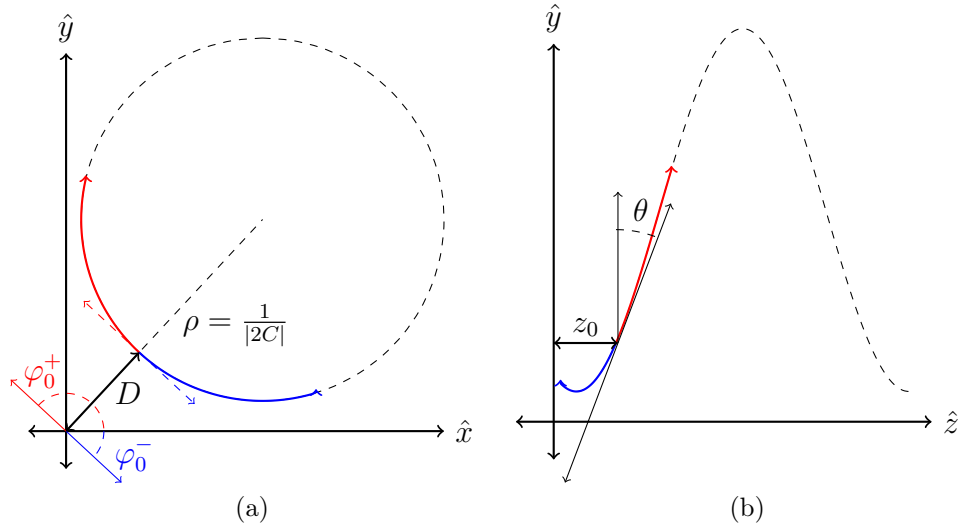


Figure 3.2. The parametrization used at CDF to describe the helical paths of particles within the inner tracking system. Paths for both positively-charged ($C > 0$, red) and negatively-charged ($C < 0$, blue) are shown, assuming that both have the same origin and opposite initial momenta. The dashed line shows the extrapolated helix common to both. Figure a shows the projection of the helix to the r - ϕ plane, and b to r - z .

(Fig. 3.2) are

$$\vec{\alpha} = \left(\cot \theta, z_0, C, D, \varphi_0 \right)$$

where

- $\cot \theta$ is the cotangent of the polar angle at the point of closest approach to the beamline. It may also be expressed in terms of the particle's momentum components: $\cot \theta = p_z/p_T$.
- z_0 is the z -position at the point of closest approach to the beamline.
- C is the half-curvature in the projection of the helix to the r - ϕ plane. It is defined to have the same sign as the particle's charge.
- D is the signed impact parameter: the distance between the beamline and the helix's point of closest approach.
- φ_0 is the ϕ direction of the track at the point of closest approach to the beamline.

The last three parameters describe the particle’s path in the r - ϕ plane, while the first two characterize the pitch and z -location of the helix [83]. A collection of different track-fitting algorithms are used to extract a set of tracks parametrized in this way from hits in the COT and silicon systems. This retains an extremely good track-finding efficiency in the central region (exceeding 99.9% for dimuon events near the J/ψ mass), while minimizing duplicate or misreconstructed tracks [84]. The momentum resolution of tracks which traverse the entire COT region has been measured to $\sigma_{p_T}/p_T^2 = 1.7 \times 10^{-3} / (\text{GeV}/c)$ using cosmic-ray events [17].

Because the lowest tracker occupancy is found at the largest radii, the primary track-finding algorithm in the central region is a progressively-updated outside-in algorithm (OI). Tracks are first formed by linking segments between COT superlayers. The COT track is then used as a seed to update the track fit to include silicon hits [83]. Outside the central region, a similar algorithm uses ISL hits and a point on the beamline to provide the seed track. Inside-out (IO) algorithms are also used to improve track-finding efficiency, particularly in the plug region [85]. Results from all track algorithms are pooled and classified into one of six mutually-exclusive categories by the availability of silicon information, stereo information (small-angle or 90°), and the originating algorithm. Inside-out tracks which share more than 15% of hits with an existing track are dropped [84].

3.3 Vertexing

An ‘event’ recorded at CDF corresponds to a single bunch-crossing. Such an event may potentially contain multiple energetic $p\bar{p}$ collisions. For sufficiently luminous bunches (early in a Tevatron store, for example) this is in fact almost assured. Usually only one vertex is sufficiently energetic to produce the high- p_T events of interest to electroweak or top studies. However, additional interactions do contribute to overall detector occupancy, and consequentially they impact tracking efficiency and

calorimeter underlying-event (UE) corrections. Furthermore, the interaction region within the detector extends over an appreciable span in the z -direction. Knowledge, then, of the actual z -location of the originating (primary) vertex is required in order to correctly measure the angular distributions of final-state objects and their transverse energies (and therefore also E_T^{miss}).

The set $\{z_0\}$ of track z -origin values provides sufficient information to identify the interaction vertices in a given event. A histogram-fitting algorithm is used to count the number of vertices and determine their z -positions. The set $\{z_0\}$ from the OI seed tracks is formed into a histogram, and seed vertices are taken from high-density regions in the histogram. Nearby tracks are then associated to the seed vertices: silicon standalone tracks must be within 1 cm of the seed vertex, and COT standalone tracks within 5 cm. Seed vertices which do not have a sufficient number of $p_T > 300$ MeV tracks are discarded. The remaining vertices are then re-fit by taking a weighted mean of the z_0 values of the associated tracks, using the z_0 fit uncertainties as weights [86].

Each vertex is assigned a quality based on the number and type of associated tracks:

- Quality 0: All vertices.
- Quality 4: ≥ 1 track with COT hits.
- Quality 7: ≥ 6 tracks with silicon hits, ≥ 1 track with COT hits.
- Quality 12: ≥ 2 tracks with COT hits.
- Quality 28: ≥ 4 tracks with COT hits.
- Quality 60: ≥ 6 tracks with COT hits.

The number of quality-12 vertices has a linear relationship with both the instantaneous luminosity as well as the magnitude of the underlying-event corrections to jet

energies. This vertex selection is used both for deriving jet-energy corrections as well as for the present analysis. The quality-12 vertex with the largest $\sum_{n=0}^{N_{\text{trk}}} p_{\text{T}}^n$ is designated as the ‘primary vertex’: the most likely origin for the bulk of the energy recorded in that bunch-crossing. Primary vertices in minimum-bias events have z_0 -resolution on the order of $100\ \mu\text{m}$. Depending on the physics process, the vertex-finding efficiency in non-minimum-bias events ranges from $80 - 100\%$ and the fake-vertex rate from $2 - 11\%$ [86].

Having identified a primary vertex, the azimuthal angles θ and η may then be recalculated in ‘vertex-corrected’ form, with the coordinate origin taken to be the location of the primary vertex rather than the center of the detector. For the remainder of this text, it should be assumed that θ and η are vertex-corrected unless otherwise specified.

3.4 Lepton Identification

The combination of tracking, separate electromagnetic and hadronic calorimetry, and well-shielded muon chambers allows many types of long-lived particles to be distinguished from one another. Muons, typically close to minimum-ionizing at collider energies, leave charged tracks, deposit minimal energy in the calorimeter, and penetrate the steel shielding at near-100% efficiency to interact with the muon chambers. Charged hadrons also leave tracks, but deposit most of their energy in the hadronic calorimeters; neutral hadrons do the same but do not leave a track. Electrons and photons deposit their energy in the EM calorimeter, but differ in whether or not they leave a charge track. Photons also shower earlier in the absorber than electrons. This collection of behaviors is illustrated in Figure 3.3.

For the purpose of the present work, energetic electrons and muons are the primary objects of interest. The term ‘lepton’ will generally be taken here to refer either to an electron or a muon. The τ has not been forgotten – although produced copiously, the

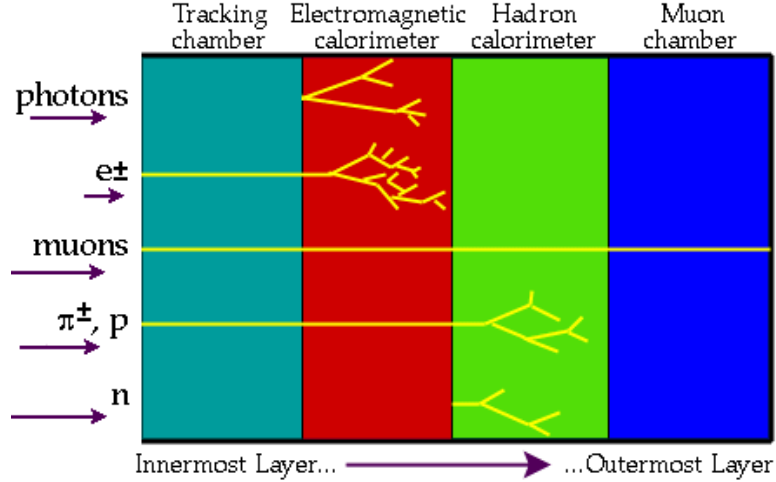


Figure 3.3. An illustration of the interactions of different particle types with the major subsystems of the CDF-II detector. The characteristic patterns of interaction allow different particle types to be distinguished in the data [12].

τ decays long before reaching the detector and is therefore observed only through its decay products: either a jet-like set of hadronic tracks, an electron, or a muon (and associated neutrinos).

Electrons

Electrons are identified by searching for charged tracks which point to an EM-dominated cluster in the central calorimeter (CEM). Clustering for electron identification is performed separately from the jet clustering described in the next section. Towers with EM energy $E_T > 2 \text{ GeV}$ and $E_{\text{had}} < 0.125 \cdot E_{\text{EM}}$ are used as seeds. Adjacent towers in the same η wedge are included in the cluster if the EM transverse energy of the adjacent tower is less than or equal to that of the seed tower [87]. The precise location of the shower is determined from the associated CES hits.

A number of variables are used to decide when track and cluster are adequately electron-like [17]:

- *EM fraction:* To be considered as an electron candidate, the calorimeter cluster must satisfy $E_{\text{had}}/E_{\text{EM}} < 0.055 + 0.00045 \cdot E$, where E is the total cluster

Table 3.1. Electron identification requirements [17].

Variable	Cut
$E_{\text{had}}/E_{\text{EM}}$	$< 0.055 + 0.00045 \cdot E$ (GeV)
E/p (for $E_T < 100$ GeV)	< 2.0
L_{shr}	< 0.2
$Q \cdot \Delta x$	> -3.0 cm, < 1.5 cm
$ \Delta z $	< 3.0 cm
χ_{strips}^2	< 10.0
ISO	< 0.1

energy measured in GeV. This helps exclude jets, which typically produce large depositions in the hadronic calorimeter. The term linear in E accounts for the increasing probability of an electron shower extending into the hadronic calorimeter as its momentum increases.

- *Track momentum ratio:* The ratio of the cluster EM energy to the track momentum must satisfy $E/p < 2.0$. Although these two values are nominally equal, it is possible for an electron to emit a hard bremsstrahlung photon. If the electron retains sufficient momentum, the electron and photon will be nearly collinear and both will contribute to the cluster energy. This cut becomes unreliable for sufficiently energetic electrons and is not applied if the cluster energy exceeds 100 GeV [17].
- *Shower Shape:* The lateral shower profile, which parametrizes the sharing of energy between the seed tower and adjacent towers [88], is required to satisfy $L_{\text{shr}} < 0.2$. Additionally, the shape of the CES strip hits is compared to data from electron test beams and must satisfy $\chi_{\text{strips}}^2 < 10.0$. These variables help distinguish real electrons and photons from early hadronic showers.
- *Track Position:* The extrapolated track must match the CES cluster: $Q\Delta x \in (-3.0 \text{ cm}, 1.5 \text{ cm})$, where Δx is the distance in the r - ϕ plane between the extrapolated track and the cluster location, and Q is the charge of the track.

The charge-weighting is a convenient way to account for differences in the development of electron- and positron-initiated showers [17]. Additionally, the distance in the z -direction between cluster and extrapolated track must satisfy $|\Delta z| < 3.0$ cm.

- *Isolation:* Electron candidates must be well-isolated: within a cone of $\Delta R < 0.4$ surrounding the electron candidate, the ratio of non-clustered energy to clustered energy must satisfy $ISO < 0.1$.

These requirements are also summarized in Table 3.1.

Muons

Muon candidates fall into two categories. First, ‘trigger muons’ are constructed from tracks which point to muon chamber stubs. This analysis includes trigger muons from the CMU and CMP systems as well as CMX. As the former two systems cover the same detector region, a muon stub in one is considered only if also present in the other. The two systems are therefore referred to in combination as CMUP. Collectively, CMUP and CMX cover the region $|\eta| < 1.1$ – although there are gaps in the coverage due to fiducial cuts made to avoid poorly-instrumented regions and areas near the edges of the muon chambers (Tbl. 3.2).

Trigger muon candidates are subject to isolation and track quality requirements. The same set of cuts is applied to both CMUP and CMX muons:

- *Track quality:* Several quality cuts are imposed on muon candidate tracks. The muon track must pass through all COT layers ($\rho_{\text{COT}} \leq 140$ cm). At least three axial layers and three stereo layers must each have seven or more hits. The track must be well-fit by its helical parametrization ($\chi^2/\text{NDF} < 2.0$). To reject cosmic-ray backgrounds, the track impact parameter must be small; this

Table 3.2. Cuts for muon identification. In this table, x is the *local* x defined by the drift direction of the chamber. ΔX is the distance between the muon stub and extrapolated track measured in the plane of the module. Fiducial distances are measured between the extrapolated track and the nearest chamber edge [17].

Variable	Cut
Track Quality Cuts	
# Axial COT Superlayers	≥ 3 with ≥ 7 hits
# Stereo COT Superlayers	≥ 3 with ≥ 7 hits
$ d_0 $ (no silicon hits)	0.2 cm
$ d_0 $ (silicon hits)	0.02 cm
χ^2/ndf	< 2.0
ρ_{cot}	140 cm
Minimum Ionizing Cuts (GeV)	
$E_{\text{EM}} (p < 100 \text{ GeV}/c)$	< 2
$E_{\text{EM}} (p \geq 100 \text{ GeV}/c)$	$< 2 + (p - 100) \cdot 0.0115$
$E_{\text{had}} (p < 100 \text{ GeV}/c)$	< 6
$E_{\text{had}} (p \geq 100 \text{ GeV}/c)$	$< 6 + (p - 100) \cdot 0.0280$
Muon Stub Cuts (cm)	
$ \Delta X_{\text{CMU}} $ (CMUP)	< 3.0
$ \Delta X_{\text{CMP}} $ (CMUP)	< 5.0
$ \Delta X_{\text{CMX}} $ (CMX)	< 6.0
CMP x -fiducial distance (CMUP)	< 0.0
CMP z -fiducial distance (CMUP)	< -3.0
CMX x -fiducial distance (CMX)	< 0.0
CMX x -fiducial distance (CMX)	< -3.0
Other Cuts	
ISO	< 0.1

is loosened for COT-only tracks, for which the impact parameter is less well-resolved.

- *Track position:* The distance between the extrapolated track and the corresponding muon stub must be $\Delta X \leq 3 \text{ cm}, 5 \text{ cm}, 6 \text{ cm}$ for CMU, CMP and CMX stubs, respectively.
- *Minimum-ionizing and isolation:* Because muons are minimum-ionizing, the calorimeter energy in the vicinity of the extrapolated track must be small. Furthermore, muon candidates must satisfy the same isolation requirements as

electrons ($\text{ISO} < 0.1$).

The trigger muon identification cuts are summarized in Table 3.2.

A second category of muon candidates is known as ‘loose muons’. This selection is designed to recover muons which fall outside the fiducial regions of the muon detection systems. These muon candidates are constructed offline by examining events which triggered on large $E_{\text{T}}^{\text{miss}}$, and looking for well-reconstructed high- p_{T} tracks that extrapolate to regions in the calorimeter with little deposited energy. This is consistent with the passage of a charged, minimum-ionizing particle that by chance falls into a region without muon coverage.

Loose muons are required to satisfy all of the same criteria as trigger muons, with the exception that no matching muon stub is required. This does result in a larger rate for fake muon backgrounds amongst loose muon events, but in the present analysis the inclusion of these events results in a gain in the number of $t\bar{t}$ candidates that is more than substantial enough to compensate for the additional background. Additionally, all loose muon events have two or more jets. This is a constraint imposed by the $E_{\text{T}}^{\text{miss}}$ trigger hardware, which rejects events with a single jet and large $E_{\text{T}}^{\text{miss}}$, as these are most likely to be very poorly measured dijet events.

3.5 Jets

Top-quark pairs that decay semileptonically produce four final-state quarks that evolve into jets of particles. Jets are initially located by searching for isolated energy deposits in the calorimeter. Tracking information is later incorporated in the form of ‘ b -tagging’, a technique to distinguish the jets produced by long-lived b -quarks from the jets produced by light quarks or gluons. The presence of jets, and in particular the presence of b -tagged jets, will be used to select candidate top-quark pair events.

3.5.1 Calorimeter Clustering

All calorimeter energy deposits have some degree of lateral breadth. In the case of jets, much of this is the intrinsic angular spread of the jet itself. However, even a single particle (an electron, for example) is naturally broadened by shower development in the absorber. It is typical that the energy from a given object is spread over many calorimeter towers; in order to recover the energy and direction of that object, it is necessary to combine – or ‘cluster’ – the measurements from adjacent towers.

Calorimeter clusters are formed using a fixed-diameter cone algorithm. Only calorimeter towers with transverse energy $E_T > 1 \text{ GeV}$ are considered, where the transverse energy is defined as

$$E_T = E \sin \theta \tag{3.1}$$

with E the energy measured in that calorimeter tower and θ the azimuthal angle of the tower with respect to the primary vertex. Towers are then ranked by E_T in descending order. The initial list of clusters is derived by taking most energetic tower in the list as the jet seed and associating with it all towers having $\Delta R < 0.4$, where the distance ΔR is defined in η - ϕ space as

$$\Delta R = \sqrt{(\eta_{\text{tower}} - \eta_{\text{jet}})^2 + (\phi_{\text{tower}} - \phi_{\text{jet}})^2}. \tag{3.2}$$

The most energetic remaining tower forms the second seed, and the process is repeated until all towers have been assigned to an initial cluster.

The centroid and transverse energy of each cluster are then calculated from the

associated towers:

$$E_{\text{T}}^{\text{jet}} = \sum_{i=0}^{N_{\text{tow}}} E_{\text{T}}^i \quad (3.3)$$

$$\eta^{\text{jet}} = \sum_{i=0}^{N_{\text{tow}}} \frac{E_{\text{T}}^i \eta^i}{E_{\text{T}}^{\text{jet}}} \quad (3.4)$$

$$\phi^{\text{jet}} = \sum_{i=0}^{N_{\text{tow}}} \frac{E_{\text{T}}^i \theta^i}{E_{\text{T}}^{\text{jet}}}. \quad (3.5)$$

where N_{tow} is the number of towers assigned to that cluster and $(E_{\text{T}}^i, \eta^i, \phi^i)$ are the transverse energy and coordinates of the i 'th tower. A new list of towers is then formed for each cluster, consisting of the towers within the jet cone ($\Delta R < 0.4$) as measured from the cluster centroid $(\eta^{\text{jet}}, \phi^{\text{jet}})$. If two clusters overlap by more than 50%, they are merged. If two clusters overlap by less than 50%, each tower in the overlap is assigned to whichever cluster has the nearer centroid. This process is iterated until the algorithm has converged (i.e. tower lists are stable) [13].

A calorimeter cluster is elevated to the status of 'jet' if it meets additional criteria on its direction and energy. In particular, we require that all jets have $|\eta| \leq 2.0$ in order that the entire jet cone lie in the well-instrumented and well-calibrated region of the detector. A jet must also have transverse energy $E_{\text{T}} \geq 12 \text{ GeV}$. A cluster with energy $E_{\text{T}} \geq 20 \text{ GeV}$ is known as a 'tight jet', and a cluster with energy $12 \text{ GeV} \leq E_{\text{T}} \leq 20 \text{ GeV}$ is a 'loose jet'. These cuts are made after the energies are corrected as described in Section 3.5.2.

3.5.2 Jet Energy Scales

In addition to the irreducible uncertainty from the sampling fraction of the calorimeters, various other effects tend to skew the energy of the measured jets away from that of the originating parton. The jet cone may not include the entire particle shower. It may incorrectly include contributions from nearby jets, the underlying event, or additional interactions in multiple-interaction events (pileup). As the calorimeter

is segmented in both η and ϕ , energy may be lost in gaps between towers or in other uninstrumented regions. Low-momentum particles can become trapped in the tracker’s magnetic field and never reach the calorimeter; even if they do, nonlinear calorimeter response at very small energies results in poor measurement. Physical, rather than instrumental, causes also contribute: heavy quarks (e.g. b , c) decay in flight and often do so leptonically. The resulting neutrino(s) carry off energy which the calorimeter cannot measure.

For most high- p_T physics, it is the energies of the originating partons that are of physical interest. Understanding the overall response of the detector to partons with a variety of energies is essentially a calibration of both detector and reconstruction; this calibration is known as the ‘Jet Energy Scale’ (JES). The JES calibrations are parametrized as a function of η and p_T to account for differing calorimeter construction and energy-dependent response in different regions of the detector. A variety of techniques are used to measure and validate the JES, as well as to understand the associated uncertainties.

The initial energy scale of the EM calorimeters is set using the electrons from $Z \rightarrow e^+e^-$; the hadronic calorimeters rely on data from a 50 GeV pion test beam. Data from single-track triggers is used to further calibrate the response of individual calorimeter towers by examining E/p – the ratio of calorimeter energy to track momentum. As most final-state particles are nearly massless at the relevant energies, this allows the calorimeter towers to be calibrated to the highly precise track momenta. This is used to tune the detector Monte-Carlo simulation to best match the physical detector response, along with minimum-bias data, electrons from $Z \rightarrow e^+e^-$, and electrons from $J/\psi \rightarrow e^+e^-$.

Using these single-particle calibrations, energy scales are derived for jets. Non-uniform response in η is corrected by a dijet balance method: it is assumed that in events with low E_T^{miss} , two back-to-back jets, and no additional objects, the jets must

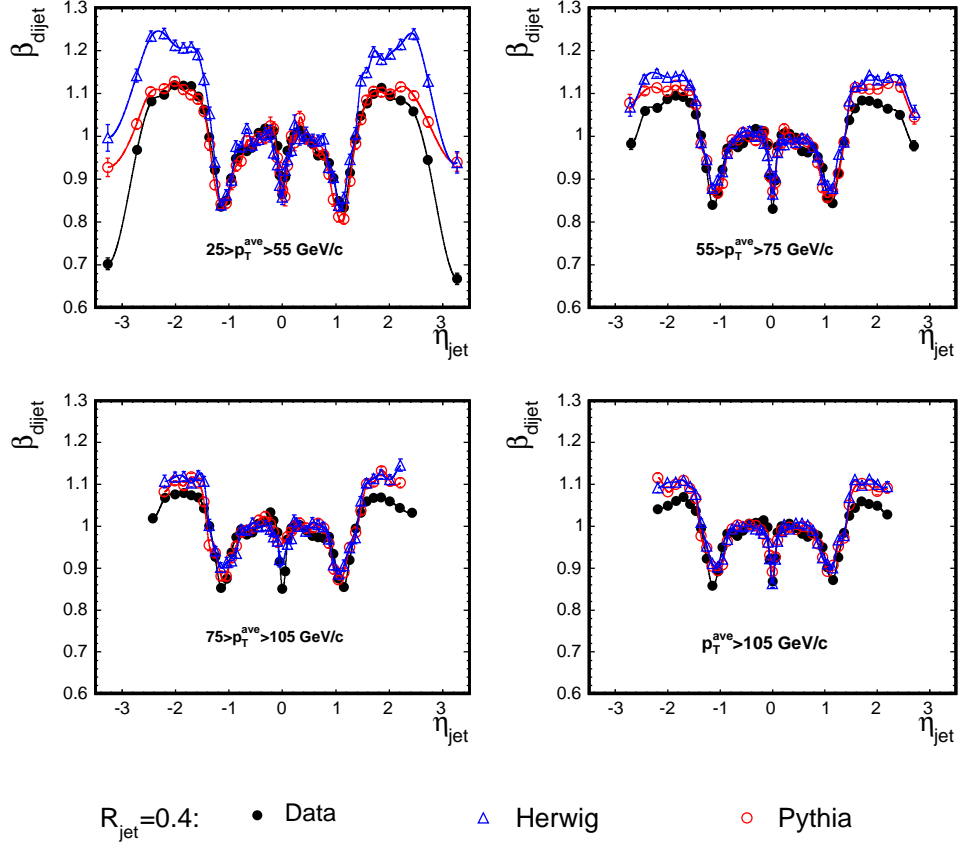


Figure 3.4. Dijet balance corrections to the jet energy scales. Shown is the ratio $\beta_{\text{dijet}} = p_{\text{T}}^{\text{probe}} / p_{\text{T}}^{\text{trigger}}$ as a function of η , in four separate ranges of the jet p_{T} . This is used to calibrate the η -dependent calorimeter response to that of the central region ($0.2 \leq |\eta| \leq 0.6$) [13].

be balanced in p_{T} . In practice, this is used to calibrate the η -dependent response of the entire calorimeter to the response of the well-instrumented and well-understood central region. To determine the corrections, one jet in $0.2 \leq |\eta| \leq 0.6$ is defined as the ‘trigger jet’ and the second jet as the ‘probe jet’. The probe jet may lie in any accessible η range; if it is also in the region $0.2 \leq |\eta| \leq 0.6$, then jets are randomly assigned as trigger and probe. The η -dependent correction factor $\beta_{\text{dijet}} = p_{\text{T}}^{\text{probe}} / p_{\text{T}}^{\text{trigger}}$ is then measured separately for several bins of $p_{\text{T}}^{\text{trigger}}$. To accommodate residual differences between the physical and simulated detector, separate corrections are derived for real and simulated events. Figure 3.4 shows the measured β_{dijet} from data as well as simulated samples.

Luminosity-dependent corrections for pileup are parametrized as a function of the number of identified vertices by measuring the energy in random cones of $\Delta R = 0.4$ in minimum-bias datasets. [13]. Additional corrections may be derived for radiation from spectator partons in the $p\bar{p}$ collision (underlying event or UE) as well as for the radiation of energy out of the jet cone (out-of-cone or OOC). For the present work, the presence or absence of energetic jets is used only to define the signal and control regions, and so these latter two corrections are not required.

Uncertainties in the single-particle calorimeter response arise from poor modeling of tracks which have low p_T or which point to the transition regions between calorimeter towers, from uncertainties in the test-beam momentum scales, and from limited single-track statistics in certain momentum ranges. The η -dependent corrections accumulate additional uncertainties from limitations of the parametrization and from the precise choice of cuts for E_T^{miss} and additional objects. Any post-correction deviations from jet balance are also assigned as systematic uncertainties, as are any differences between real and simulated data (PYTHIA). Systematic uncertainties on JES are parametrized in η and p_T in the same way as the JES calibrations themselves. Differences between simulated events generated with PYTHIA and HERWIG (as seen in Fig. 3.4) will be included later as a separate systematic uncertainty on hadronization and parton showering.

3.5.3 *B*-Tagging

A variety of algorithms are available to distinguish between jets that originate from a b -quark and jets that originate from a light quark or gluon. Many of these algorithms exploit the fact that b -hadrons have an unusually long lifetime, on the order of $c\tau \sim 0.5$ mm. At an energy of 50 GeV – fairly typical of a b -quark produced by a decaying nonrelativistic top quark – this decay length is enhanced by a Lorentz factor of ~ 10 . These millimeter-scale displacements between the primary vertex

and the site of the b decay (the ‘secondary vertex’) are readily measurable using the highly accurate tracking provided by L00 and the SVX system. This process is known as ‘ b -tagging’, and in the present analysis it is accomplished by the widely-known and widely-used SECVTX algorithm [18].

The SECVTX Algorithm

SECVTX functions on a per-jet basis. The algorithm selects tracks within the cone of a given jet that have a large impact parameter and attempts to reconstruct a secondary vertex from those tracks. If the secondary vertex is significantly displaced in the transverse direction, the jet is b -tagged. This requires accurate knowledge of the transverse positions of both primary and secondary vertices.

To obtain the transverse position of the primary vertex, SECVTX uses all tracks associated with the vertex that have silicon hits and have impact parameter significance $|D|/\sigma_D < 3$. The uncertainty σ_D includes both the uncertainties on the track impact parameter as well as on the beamline location. The transverse beam profile at the primary vertex’s z -location is also used as a constraint. Tracks which contribute $\chi^2 > 10$ to the fit are then discarded. The primary vertex position is then re-fit, and the track pruning repeated, until all remaining tracks pass the χ^2 cut. The resolution on the transverse position of the primary vertex generally ranges between 10 – 32 μm , depending on the event topology and the number of tracks contributing to the fit.

Each jet is then considered in turn. The SECVTX algorithm begins by searching for tracks that lie inside the jet cone. Poorly-reconstructed tracks are rejected by imposing several cuts on the track transverse momentum, the number of silicon hits, the quality of those hits, and the χ^2/ndf of the final track fit. If at least two well-reconstructed tracks within the jet cone remain, the jet is ‘taggable’. From these remaining tracks, SECVTX uses a two-stage procedure to attempt to reconstruct a displaced vertex. The first stage looks for three-or-more-track displaced vertices.

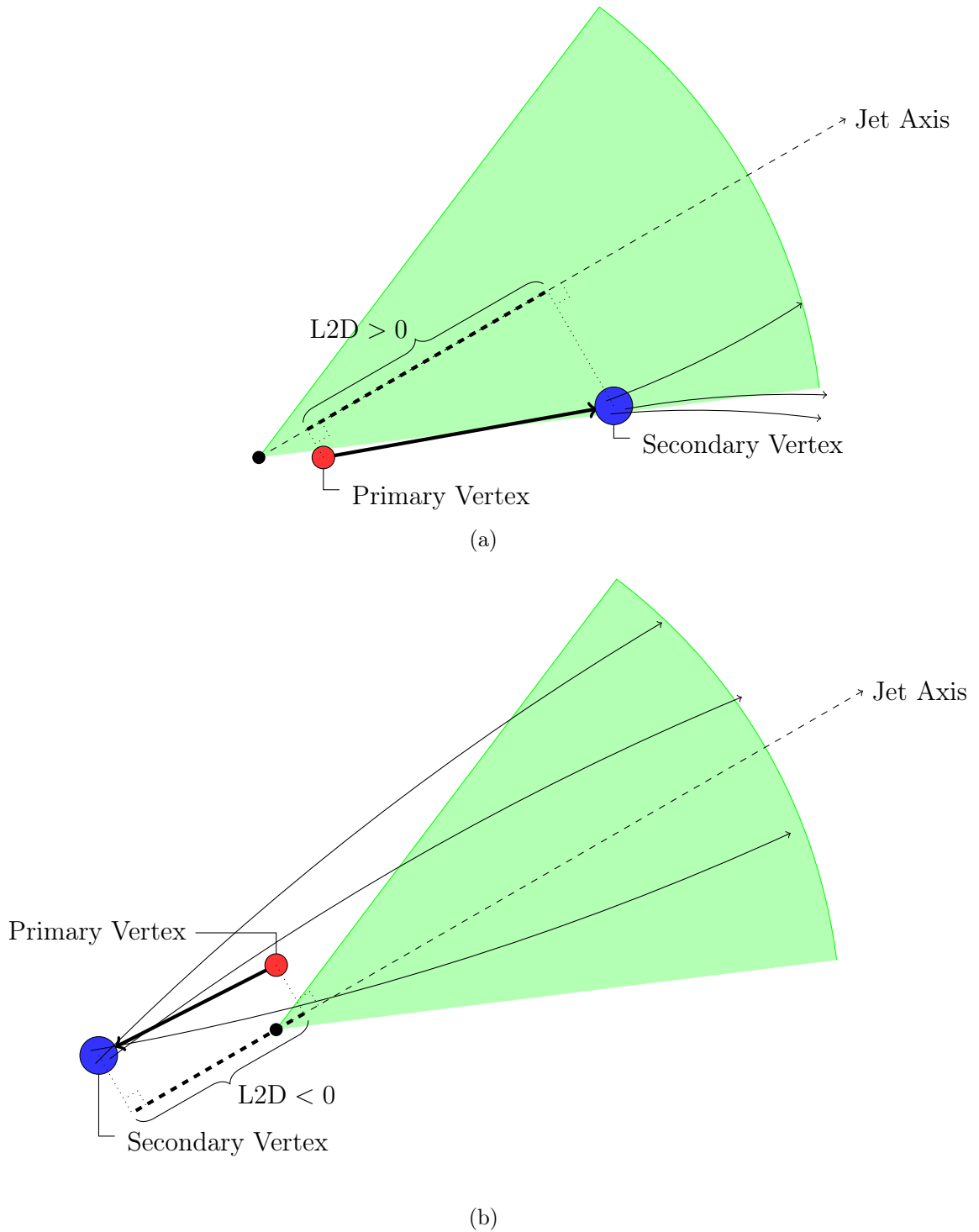


Figure 3.5. A depiction of the parameter L2D used in SECVTX b -tagging. The jet cone is indicated by the shaded wedge, and the jet axis by the dashed line. The displacement vector between the primary and secondary vertices (heavy solid line) is projected onto the jet axis, and the length of the projection is the parameter L2D (heavy dashed line). Figure a shows a ‘positive tag’ ($L2D > 0$) and b shows a ‘negative tag’ ($L2D < 0$).

Table 3.3. Track selection requirements for the SECVTX algorithm [18].

Variable	Cut	
Primary Vertex Fit		
Impact Parameter Significance	$ D $	$< 3\sigma_D$
χ^2 Threshold	χ^2	< 10
Secondary Vertex Fit (First Pass)		
Number of Tracks	N_{trk}	≥ 3
Track Momentum (all tracks)	p_T	$> 0.5 \text{ GeV}/c$
Track Momentum (leading track)	p_T	$> 1.0 \text{ GeV}/c$
Impact Parameter Significance	$ D $	$> 2.5 \cdot \sigma_D$
Tagging Threshold	L2D	$> 7.5 \cdot \sigma_{\text{L2D}}$
Secondary Vertex Fit (Second Pass)		
Number of Tracks	N_{trk}	$= 2$
Track Momentum (all tracks)	p_T	$> 1.0 \text{ GeV}/c$
Track Momentum (leading track)	p_T	$> 1.5 \text{ GeV}/c$
Impact Parameter Significance	$ D $	$> 3.0 \cdot \sigma_D$
Tagging Threshold	L2D	$> 7.5 \cdot \sigma_{\text{L2D}}$

A track is included in the first-stage fit only if its transverse momentum satisfies $p_T > 0.5 \text{ GeV}/c$ and its impact parameter is significantly distant from the primary vertex ($|D|/\sigma_D > 2.5$). At least one of the tracks must also satisfy $p_T > 1.0 \text{ GeV}/c$. If the first pass is unsuccessful, a second pass attempts to fit a two-track vertex with tighter track requirements. In the second pass, the track impact parameter must be $|D| > 3.0$ for boths tracks; one track must have $p_T > 1.0 \text{ GeV}/c$ and the other $p_T > 1.5 \text{ GeV}/c$. These requirements are summarized in Table 3.3.

If a secondary vertex is located in this way, the algorithm takes the 2-d transverse displacement vector between secondary and primary vertex and projects it onto the 2-d jet axis. The length of this projection, known as L2D, is used as the figure-of-merit to distinguish b -jets from light jets. The quantity L2D is therefore signed: it is positive if the vertex is displaced in the same direction as the jet, and negative if displaced in the opposite direction. Displaced vertices from b - and c -decays tend to have large positive L2D, while displaced vertices resulting from the misreconstruction of light jets are typically small and symmetric about zero. A jet is ‘tagged’ if the

displaced vertex satisfied $L2D/\sigma_{L2D} > 7.5$ (a ‘positive tag’) or $L2D/\sigma_{L2D} < -7.5$ (a ‘negative tag’). The uncertainty σ_{L2D} is calculated for each individual vertex fit, but is typically around $190\ \mu\text{m}$ [18].

Tag Matrices and SECVTX Performance

The performance of SECVTX is quantified by a pair of complementary measures: the *tag efficiency* is the probability that a jet from an actual b -quark decay will be b -tagged, while the *mistag rate* is the probability that a light-quark or gluon jet will produce an (incorrect) b -tag. Because SECVTX depends intimately on the detailed behavior of the tracking system, it is not possible to simulate its performance with the accuracy necessary for practical use. Instead, these parameters must be measured in data. The resultant calibrations are used to adjust the tag rates in simulated samples to reflect the performance of the physical CDF-IIb detector.

The mistag rate is measured using several large inclusive jet samples (JET20, JET50, JET70, and JET100), composed of events where detector readout was triggered at Level 2 by the presence of a calorimeter cluster having energy beyond a specified threshold (20, 50, 70, and 100 GeV respectively). These provide statistically large jet samples constituted primarily by light-quark and gluon jets.

The mistag rate is parametrized as a function of several variables which are correlated with tagging behavior [89]:

- *Jet E_T* : The average opening angle between tracks increases as the energy of the associated jet is reduced. Larger opening angles tend to improve secondary vertex reconstruction.
- *Jet η* : The effective lever-arm of the tracking system changes with the angle of incidence of the track, resulting in small changes in impact parameter resolution as a function of jet η . This variable also accommodates edge-effects

in the tracking system near the transition region between COT- and silicon-standalone-tracking.

- *Number of Tracks per Jet*: Secondary vertex reconstruction is improved when larger numbers of good tracks contribute to the fit.
- *Number of Primary Vertices*: The number of primary vertices is correlated with instantaneous luminosity and therefore the overall occupancy of the tracking system, which appreciably impacts tagging performance.
- $\sum E_T$: The total measured energy of an event is also strongly correlated with detector occupancy.
- *Primary vertex z_0* : The z -location of the primary vertex is important for accurately modeling b -tagging in vertices located near the bulkhead regions which separate adjacent barrels of the silicon tracking system.

Mistag rates are initially calculated as the ratio of the number of jets with a negative tag to the total number of taggable jets. Small additional corrections are required to account for asymmetries between positive- and negative-tag rates as well as for heavy-flavor contamination of the inclusive jet samples. These are derived from simulated data samples [90]. In the region $|\eta| \leq 1.0$ where tracks intersect all COT layers, the predicted probability of mistagging a light jet is generally under 1%.

Systematic uncertainties on the mistag rates are assessed from several sources. A collection of different inclusive jet samples are used to derive the mistag matrices. The largest deviation between any one sample and the inclusive mistag matrix is designated as a systematic uncertainty. Uncertainties resulting from $\sum E_T$ are calculated by increasing $\sum E_{rmT}$ by the mean jet energy in each event. Trigger bias is accounted for by dividing the jet sample into ‘trigger’ jets (the jet closest to the cluster which resulted in the Level-2 trigger) and ‘non-trigger’ jets. The largest deviation of either category is taken as the systematic uncertainty [89, 91].

The tag efficiency is modeled by deriving a scale-factor which is used to adjust the simulated tag rate to match the performance of the physical detector. This is accomplished using a sample which is enriched in b -quarks but has a known composition. Two methods are employed. Both of these rely on samples with exactly two back-to-back jets, in which one jet has an identified lepton within the jet cone (the ‘electron jet’ or ‘muon jet’) and the other has a SECVTX b -tag. The presence of a lepton within a jet is a characteristic feature of semileptonic decays of b and c quarks, but is less common in light jets.

In the muon-jet sample, the composition is determined by fitting p_T^{rel} , the momentum of the lepton in the direction perpendicular to the jet axis. This variable is sensitive to the mass of the originating parton, but is robustly modeled by the detector simulation. In a sample which is already enriched in b -quarks, it is adequately sensitive to the relative proportion of light- and heavy- jets.

In the electron-jet sample, the scale-factor is determined algebraically by comparing the rate of events in which the electron-jet is *also* tagged to the rate of events in which it is not. In combination, the two methods indicated that the appropriate scale factor on the simulated tagging rate is approximately 0.92. The resultant tag efficiency in the central region of the detector is over 40% [92].

For the production of simulated samples, the measured tag efficiencies and mistag rates are used to assign b -tags to simulated jets using the known type of originating parton. To maximize the statistical power of simulated samples, a procedure known as ‘tag weighting’ is employed. For each simulated event, a list of all possible tag combinations is prepared. The measured tag matrices are then used to assign a probability to each tag combination. When performing measurements on simulated samples, each tag combination is included as if it were a unique event, but is weighted according to the probability of that tag combination.

3.6 E_T^{miss} and H_T

The CDF-IIb detector is instrumented so as to record virtually the entire spectrum of known stable particles, ranging from the easily-shielded photon to the highly penetrating muon. Unfortunately, not every particle is so cooperative as to deposit its energy in a small and convenient volume: the neutrino couples to detector material only through the weak interaction, and is sufficiently penetrating that there is no feasible avenue for direct detection at a collider at any useful efficiency level. However, the high efficiency of the detector at capturing all other stable particles allows the properties of sufficiently energetic neutrinos to be inferred nonetheless.

The partons that initiate a collision have negligible transverse momentum. So long as conservation of momentum is obeyed, the vector sum of transverse momenta over all final-state particles from a collision will remain zero. Any deviation from this behavior must result either from instrumental uncertainties or from energetic particles that escape the detector unobserved. The additional contribution required to guarantee that the total transverse momentum is zero is readily calculated:

$$E_x^{\text{miss}} = - \left(\sum_{n=0}^{N_{\text{towers}}} E^n \sin \theta^n \cos \phi^n + \sum_{n=0}^{N_{\mu}} p_x^{\mu,n} \right) \quad (3.6)$$

$$E_y^{\text{miss}} = - \left(\sum_{n=0}^{N_{\text{towers}}} E^n \sin \theta^n \sin \phi^n + \sum_{n=0}^{N_{\mu}} p_y^{\mu,n} \right) \quad (3.7)$$

$$E_T^{\text{miss}} = \sqrt{(E_x^{\text{miss}})^2 + (E_y^{\text{miss}})^2}. \quad (3.8)$$

The sum of energies runs over all calorimeter towers, and θ is the vertex-corrected azimuthal angle of the tower. Muons escape the calorimeter, and so their contribution must be accounted for separately.

Both instrumental and physical sources contribute to E_T^{miss} . Uncertainties in calorimeter response or muon identification, energy lost between calorimeter towers, and incorrect vertex identification may all potentially create instrumental E_T^{miss} .

Neutrinos within heavy-quark jets can cause physical (but usually uninteresting) additions. However, the neutrinos of interest to the present analysis are produced by on-shell electroweak gauge bosons; their energy scale is much greater than that of jet neutrinos or instrumental uncertainties. To assess these hard neutrinos, $E_{\text{T}}^{\text{miss}}$ serves as an effective proxy.

A second quantity of interest is the scalar sum of the transverse energies of all identified objects in an event. This is known as H_{T} :

$$H_{\text{T}} = E_{\text{T}}^{\text{miss}} + \sum_{n=0}^{N_{\ell}} p_{\text{T}}^{\ell,n} + \sum_{n=0}^{N_{\text{jet}}} E_{\text{T}}^{\text{jet},n}. \quad (3.9)$$

Here, $E_{\text{T}}^{\text{miss}}$ is included as an object under the hypothesis that it corresponds to an unobserved neutrino. Sums run over all identified leptons and all identified jets (tight and loose); unclustered calorimeter energy or clusters that do not qualify as jets are not included. Since it depends only on *transverse* quantities, it is invariant under Lorentz boosts along the z -direction and also independent of the unknown neutrino p_{Z} . H_{T} is highly correlated with the total energy, making it a useful variable to distinguish events that are likely to be top pairs from background.

CHAPTER IV

Signal Selection and Modelling

The previous chapter has established a number of higher-level analysis objects and quantities of physical interest. Those quantities will now be used to define the criteria for an event to be included in this analysis. The sample is a superset of that used in the CDF $A_{\text{FB}}^{\Delta y}$ measurement [35]. As these selection criteria necessarily include events that are produced by processes other than top-pair production (i.e. backgrounds), a technique to estimate the composition of the data sample will be described, together with its results.

Standard-Model-based estimates of the expected lepton asymmetry are discussed and several benchmark beyond-the-Standard-Model scenarios are introduced, which will be used to validate the correction technique described in the next chapter.

In addition, two modified sets of selection criteria will be developed, which will provide statistically-independent data samples in order to validate the modeling of the detector and backgrounds.



Figure 4.1. The chapter headpiece.

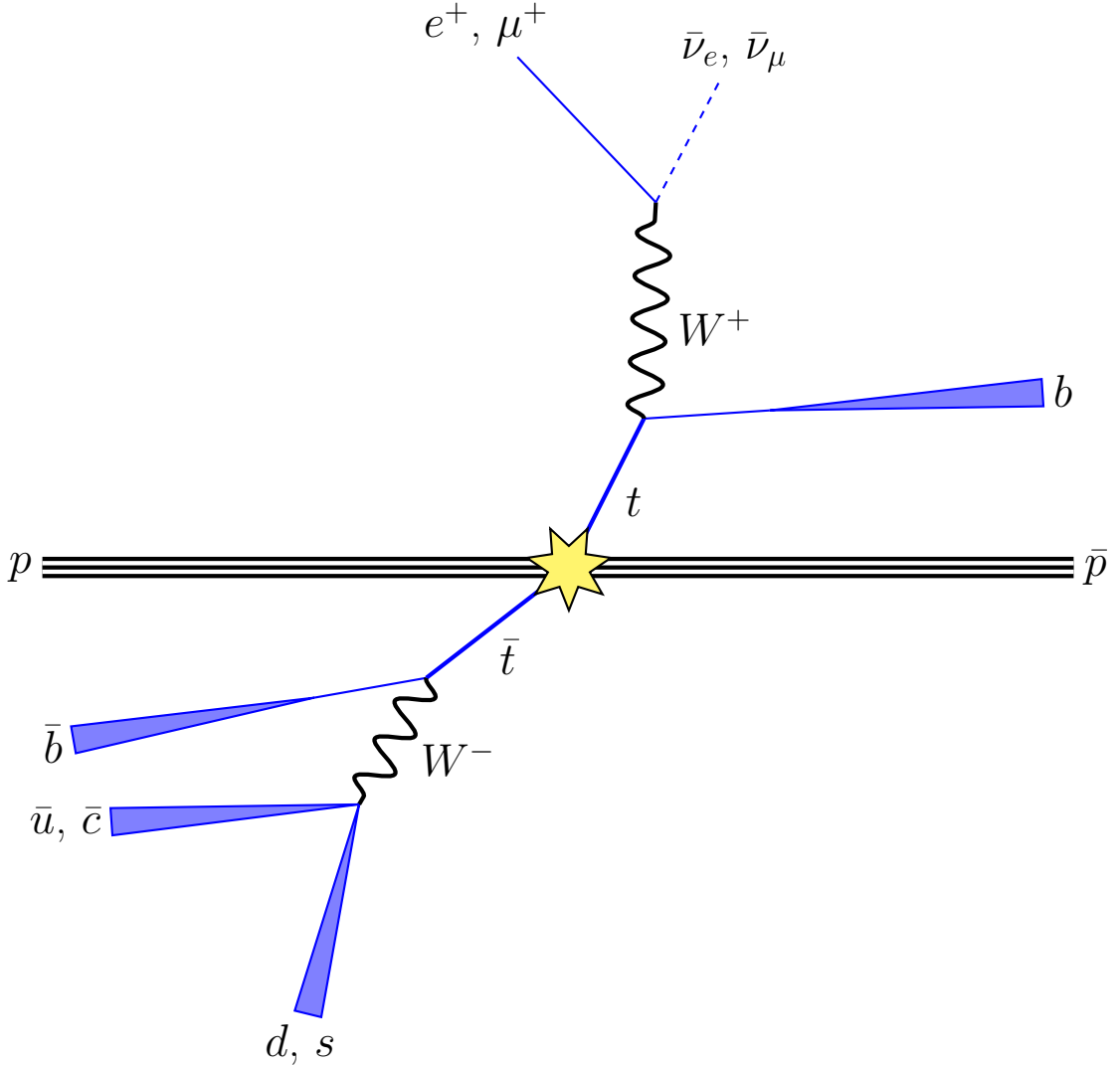


Figure 4.2. A top-quark pair in the ℓ +jets channel. In this illustration, the top (t) decays into a lepton, a neutrino, and a bottom quark which produces a b jet. The anti-top (\bar{t}) produces a second b jet and two light jets.

4.1 Definition of the Signal Region

This analysis utilizes top-pair events in which one top decays hadronically ($t \rightarrow Wb \rightarrow u\bar{d}b$) and the other decays leptonically ($t \rightarrow Wb \rightarrow l\bar{\nu}_l b$): the ‘lepton + jets’ channel. It is characterized by the presence of a lepton, a neutrino, and a b -jet from the leptonically-decaying top, alongside a second b -jet and two light jets from the hadronically-decaying top. This is illustrated in Figure 4.2. Additional jets may be

produced by initial-state gluons radiated from the incoming quark and anti-quark, or by final-state gluons radiated by the outgoing top-quark pair or its decay products.

Experimentally, these events are typified by an isolated lepton, large $E_{\text{T}}^{\text{miss}}$, and four or more energetic jets. Because the mass difference between the top quark and W boson is large, as is the mass difference between the W and its daughters, final-state objects are generally produced at high momentum. Reflecting this, minimum requirements are imposed on the transverse energy or momentum of the corresponding detector objects. These cuts also serve to restrict the detector objects under consideration to parameter ranges in which they are well-resolved and well-calibrated.

4.1.1 $W + \text{Jets Selection}$

Three statistically-independent samples will be utilized. One is the signal region itself; the other two are control regions which serve to validate the modeling of the detector and of the non-top-quark-pair events that contaminate the signal region. These samples are drawn from a larger selection, defined by requirements on event quality, the lepton, and $E_{\text{T}}^{\text{miss}}$. This selection is composed of events triggered by any of the mechanisms described in Section 3.4. Data-taking runs are included only if at least one lepton trigger and all other relevant detector subsystems are fully functional; the resulting data correspond to an integrated luminosity of 9.4 fb^{-1} .

To ensure that all events are located in the region of the detector with good tracking coverage, the z -position of the primary vertex is restricted to $z_0 < |60 \text{ cm}|$. There must be exactly one isolated lepton whose transverse momentum satisfies $p_{\text{T}}^{\ell} > 20 \text{ GeV}/c$, and the lepton's origin must be close to the primary vertex: $|z_0 - z_{\ell}| < 5.0 \text{ cm}$. Additionally, the fully-corrected missing transverse energy must be at least $E_{\text{T}}^{\text{miss}} > 20 \text{ GeV}$. As these properties are characteristic of the presence of a W -boson that decays into a lepton and a neutrino, this is known as the ' $W + \text{jets}$ ' selection. Note that the $W + \text{jets selection}$ is distinct from the $W + \text{jets background processes}$

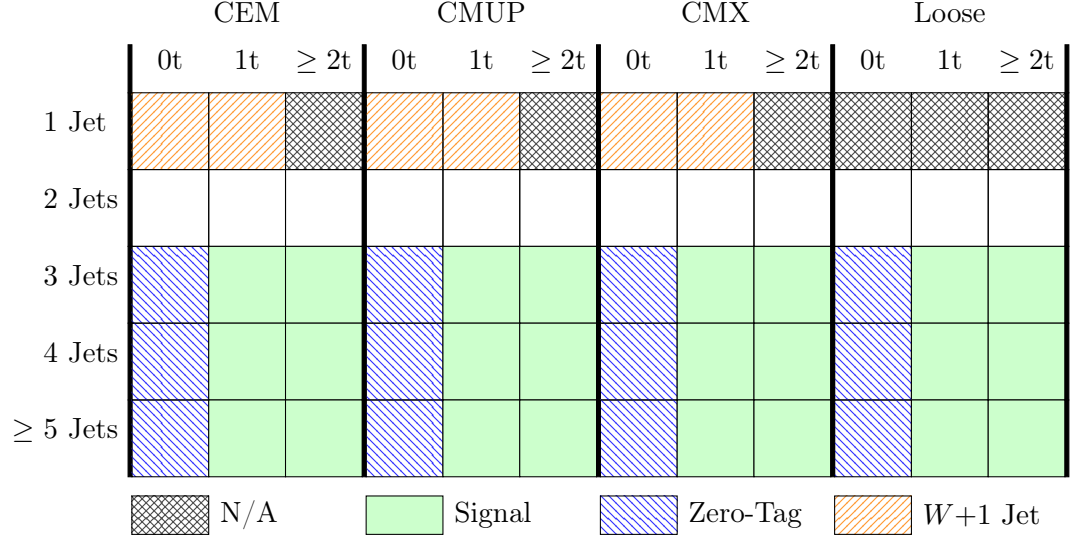


Figure 4.3. Divisions of $W + \text{jets}$ and their assignment to the signal and control regions. The $W + \text{jets}$ sample is separated by trigger (outer column) as well as by the number of tight jets (row) and the number of tagged tight jets (inner column). Gray, crosshatched regions do not exist or are unavailable. Note that additional requirements are imposed on these regions as per Table 4.1.

described in the next section.

Events satisfying these requirements are divided into mutually-exclusive categories according to the originating trigger (CEM, CMUP, CMX, or loose muons), the number of tight jets in the event (1, 2, 3, 4, ≥ 5), and the number of tight jets that have been b -tagged (0, 1, ≥ 2). To be considered a jet, a calorimeter cluster must have $|E_T^{\text{jet}}| < 2.0$ and $E_T^{\text{jet}} > 12$ GeV. The jet is ‘tight’ if it has $E_T^{\text{jet}} > 20$ GeV and ‘loose’ if $12 \text{ GeV} < E_T^{\text{jet}} < 20$ GeV. These divisions are illustrated in Figure 4.3.

Table 4.1 summarizes the shared requirements on all three samples as well as the additional requirements imposed individually on each. The individual regions will be more precisely defined in their respective sections that follow.

Table 4.1. The selection requirements for events in this analysis. The first section lists cuts applied to all regions. The remaining sections list the additional cuts that are individually applied to the signal and each control region.

Variable	Cut
Trigger	CEM, CMUP, CMX, Loose Muons
Primary Vertex z -position	$ z_0 < 60$ cm
Lepton z -position	$ z_0 - z_\ell < 5$ cm
Number of Leptons	$N_\ell = 1$
Lepton Isolation	ISO < 0.1
Lepton Transverse Momentum	$p_T^\ell > 20$ GeV/ c
Missing Transverse Energy	$E_T^{\text{miss}} > 20$ GeV
‘Tight’ Jet Transverse Energy	$E_T^{\text{jet}} > 20$ GeV
‘Loose’ Jet Transverse Energy	$E_T^{\text{jet}} > 12$ GeV
	$E_T^{\text{jet}} < 20$ GeV
Jet Pseudorapidity (Tight and Loose)	$ E_T^{\text{jet}} < 2.0$
Signal Region	
Number of Tight Jets	$N_{\text{tj}} \geq 3$
Total Number of Jets (Tight + Loose)	$N_{\text{tj}} + N_{\text{lj}} \geq 4$
Number of b -tagged Tight Jets	$N_{\text{tag}} \geq 1$
Total Transverse Energy	$H_T > 220$ GeV
Control Region I ($W+1$ Jet)	
Number of Tight Jets	$N_{\text{tj}} = 1$
Minimum Leptonic W Mass	$M_{\ell w}^{\text{min}} > 20$ GeV
Control Region II (Zero-Tag)	
Number of Tight Jets	$N_{\text{tj}} \geq 3$
Total Number of Jets (Tight + Loose)	$N_{\text{tj}} + N_{\text{lj}} \geq 4$
Number of b -Tagged Tight Jets	$N_{\text{tag}} = 0$
Total Transverse Energy	$H_T > 220$ GeV

4.1.2 Signal Region

The jets produced by top quarks tend to be energetic (see Fig. 4.6). Consequentially, most top-quark events reside in the categories with four or more tight jets (known as the ‘ $W+4$ ’ sample, identical to the selection of Ref. [35]). However, with four jets in an event, there is an appreciable probability that at least one will fail the tight jet cuts on purely statistical grounds. Such an event would then occupy the three-tight-jet bin. To recover some of these events while suppressing the otherwise-

substantial backgrounds in the three-tight-jet bin, events are also included if they have three tight jets and one loose jet (the ‘ $W+3+1$ ’ sample).

In principal, two of the jets from the decay of a top-quark pair are b -jets, and indeed, requiring that at least two jets are b -tagged does produce a highly-pure sample of top-quark pairs. However, with an overall b -tagging efficiency of 40%, many top-quark pairs are associated with one or even zero b -tagged jets. Requiring only one b -tagged jet provides an effective compromise between sample size and sample purity in the signal region.

Sample purity is also enhanced by imposing a requirement on the minimum total transverse energy in the event: $H_T > 220$ GeV. This primarily impacts the non- W/Z backgrounds described in the next section, reducing them by 30% while having almost no effect on the predicted top-pair yield.

4.2 Background Components

Events with the desired signature may be produced by a number of physical processes other than top-quark pair-production. In a hadron collider, copious strong production of jets leads to many events with high jet multiplicity. To enter the signal regions, an event must also have an isolated, energetic lepton and missing transverse energy. There are several sources of such events:

$W + \text{Jets}$

A real W -boson may be produced in conjunction with a large number of radiated jets, e.g. from the process $u\bar{d} \rightarrow W^+ \rightarrow \ell\bar{\nu}_\ell$ with the jets resulting from initial-state radiation. These are modeled using simulated events produced by ALPGEN. $W + \text{jets}$ events are further subdivided into categories:

- $W + \text{Light Flavor}$ ($W + \text{LF}$), with all jets produced by light quarks or gluons,

- Wc , where one jet is produced by the decay of a charm quark, and
- $Wb\bar{b}$ and $Wc\bar{c}$, where a heavy-quark pair is produced alongside a W boson.

The latter two categories are collectively referred to as W +heavy flavor ($W + \text{HF}$). These processes are treated separately because ALPGEN does not correctly predict their relative rates. By separating them, they may be individually normalized to reproduce the correct heavy-flavor fraction as measured in jet data.

Non- W/Z

These events are distinguished by the lack of a real electroweak gauge boson (W or Z). Instead, a mis-reconstructed event with high jet multiplicity is incorrectly identified as having an isolated lepton and significant $E_{\text{T}}^{\text{miss}}$. This may occur, for example, when an event contains a secondary lepton produced by a decaying b or c . If nearby particles fall outside the fiducial region of the calorimeter, the lepton may pass the isolation requirements while the unmeasured particles produce the requisite $E_{\text{T}}^{\text{miss}}$.

Non- W/Z events predominantly contaminate the isolated electron trigger (CEM) and, to a lesser extent, the loose muon trigger. This background is modeled using templates produced from a data-driven sideband. The sideband consists of events with lepton candidates which meet the two kinematic requirements for electron identification (Table 3.1; $E_{\text{had}}/E_{\text{EM}}$ and ISO), but fail two of the five remaining cuts. As the non-kinematic cuts primarily remove ‘fake’ electrons produced by non- W/Z processes, inverting them provides a selection rich in non- W/Z events. The retention of the two kinematic cuts helps ensure that the templates closely resemble the non- W/Z events in the signal region [93].

Single Top

Most top quarks at the Tevatron are produced in pairs. However, two processes may result in events containing a single top quark: First, a sufficiently massive virtual W boson may decay to a top and bottom quark (s -channel). Second, a virtual W interacts with a b -quark from the "sea" to produce a top (t -channel). If additional jets are produced by initial- and final-state radiation, these events may readily enter the signal region. This background is modeled using simulated events produced by PYTHIA.

Di-boson

Events containing pairs of electroweak gauge bosons (WW , WZ , and ZZ) together with two or more radiated jets form an additional irreducible background in the signal region. These also are modeled using PYTHIA.

Z + Jets

A Z produced in conjunction with jets may enter the signal region if the Z decays into a pair of leptons, and one lepton is detected while the other is not. This produces the characteristic signature of a lepton with E_T^{miss} . Like the W + jets backgrounds, Z + jets is modeled with ALPGEN.

4.3 Top-Pair Production Models

Model data sets of top-quark pairs are created with Monte Carlo event generators. The benchmark for Standard Model top-quark pair production is the POWHEG [94] generator, which includes NLO QCD but not electroweak effects. For all distributions of interest, POWHEG is used as the nominal model. The sole exception is A_{FB}^ℓ itself, for which the direction calculation of Ref. [32], which explicitly includes electroweak

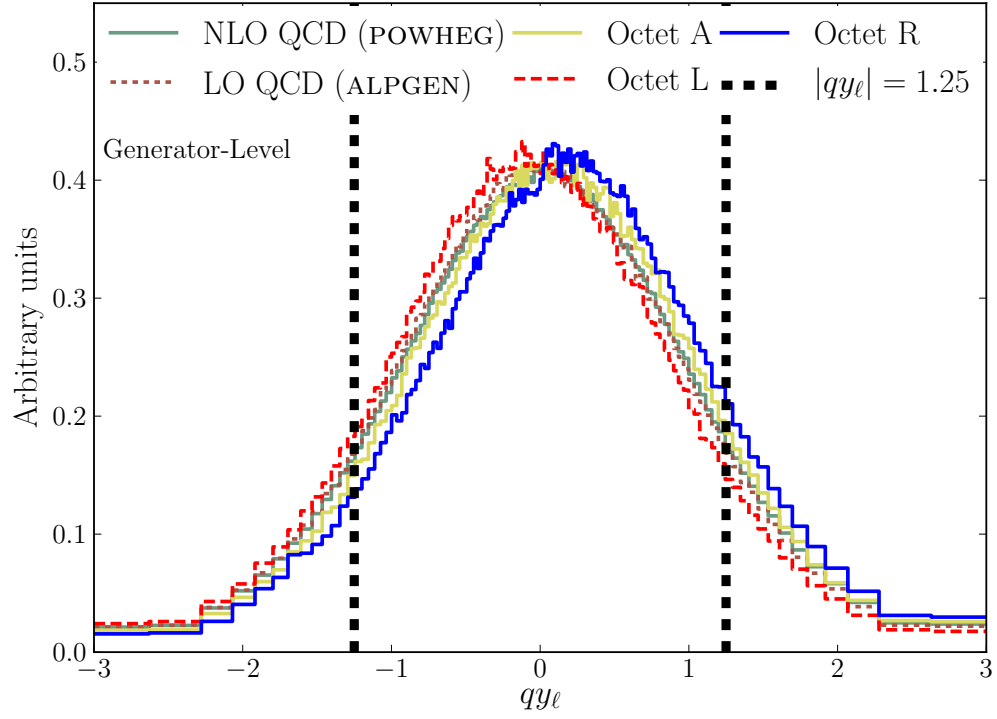
Table 4.2. Production-level asymmetries and polarizations for the model datasets. Here, the polarization is defined as $P = (N(t_R\bar{t}_R) - N(t_L\bar{t}_L)) / (N(t_R\bar{t}_R) + N(t_L\bar{t}_L))$, with the beamline taken as quantization axis. The statistical uncertainty on the final digit is shown in parenthesis.

CDF Run II Preliminary $\int \mathcal{L} = 9.4/\text{fb}$				
Model	$A_{\text{FB}}^{\Delta y}$	A_{FB}^{ℓ}	Polarization	
POWHEG	+0.052 (0)	+0.024 (0)	+0.001 (2)	NLO Standard Model QCD
ALPGEN	-0.000 (1)	+0.003 (1)	+0.009 (4)	LO Standard Model QCD
Octet A	+0.156 (1)	+0.070 (2)	-0.005 (6)	LO unpolarized axigluon
Octet L	+0.121 (1)	-0.062 (1)	-0.290 (6)	LO left-handed axigluon
Octet R	+0.114 (2)	+0.149 (2)	+0.280 (6)	LO right-handed axigluon

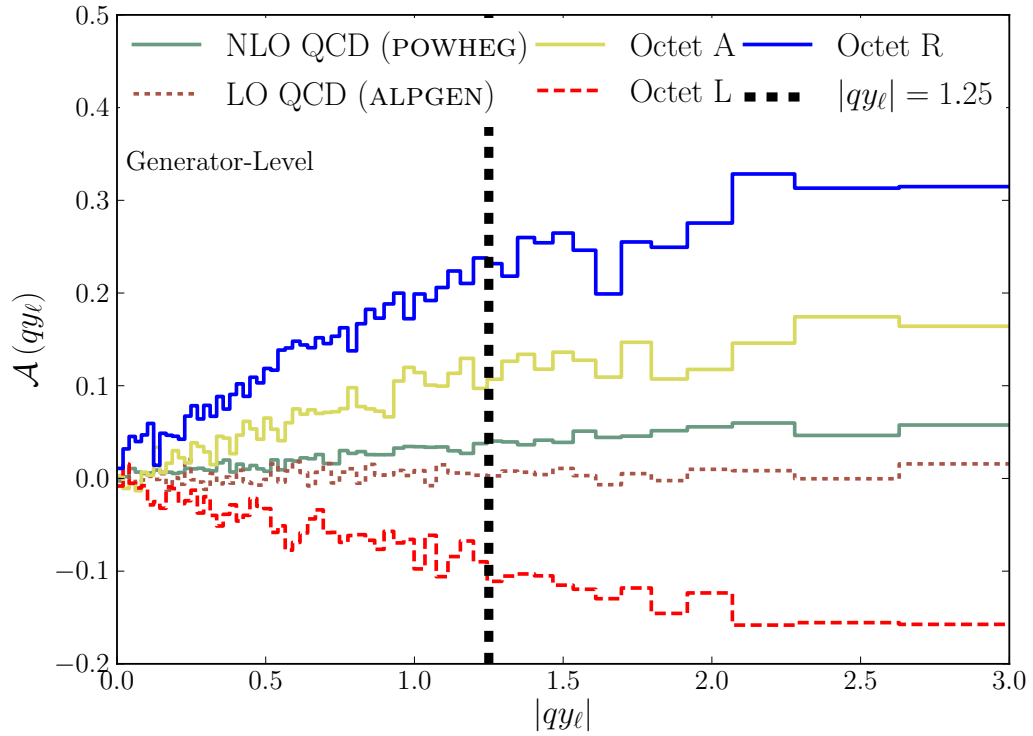
interference effects, is better suited.

Several additional models will be used to test the correction procedure developed in the next chapter. The LO Standard Model is used as a null-asymmetry sample, represented by events generated with ALPGEN [95]. To study larger asymmetries, the MADGRAPH [96] generator is used to produce three models containing heavy color-octet partners to the gluon. In these models, interference effects between Standard Model s -channel production (Fig. 1.5a) and an analagous diagram containing the heavy gluon partner can produce both a non-SM top-quark production asymmetry and a non-SM polarization.

These models are tuned to explore the lepton asymmetry in three different top-quark polarization scenarios, while maintaining an inclusive Δy asymmetry compatible with CDF measurements. The three models include the cases of new physics contributions with axial-vector couplings between the axigluon and quarks (Octet A), left-handed couplings (Octet L), and right-handed couplings (Octet R). Octet A includes a massive ($M_A = 2.0 \text{ TeV}/c^2$) axigluon [36]. Octet L and Octet R are the models of Ref. [59]. Both include axigluons of mass $M_A = 200 \text{ GeV}/c^2$ and decay width $\Gamma_A = 50 \text{ GeV}/c^2$. The large width is proposed by the authors as a means to evade dijet resonance searches. However, the importance of these samples in this work is in the validation of the analysis procedures for any polarization and asymmetry,



(a)



(b)

Figure 4.4. The distribution of simulated $t\bar{t}$ events as a function of qy_ℓ at the production level (Fig. (a)) for several benchmark models. The corresponding asymmetries in each bin are shown in Figure (b). The vertical lines at $|qy_\ell| = 1.25$ indicate the limits of the lepton acceptance.

independent of any limits on these particular models.

The lepton asymmetries in these three cases are shown in Table 4.2 along with the SM LO (ALPGEN) and NLO (POWHEG) estimates. The distribution in the charge-weighted lepton rapidity qy_ℓ is shown in Figure 4.4. The lepton asymmetry in Octet A results only from the Standard Model kinematic correlation with $A_{\text{FB}}^{\Delta y}$. In the right-handed Octet R, the polarization produces an additional positive contribution to the asymmetry of qy_ℓ . In Octet L, the negative contribution of the left-handed polarization overcomes the effect of a positive $A_{\text{FB}}^{\Delta y}$ and results in a negative A_{FB}^ℓ . A few other distributions are reproduced in Figure 4.5 to confirm that aside from the lepton asymmetry, the different models are generally consistent.

Leading order (LO) event generators are configured to use the CTEQ6.1L set of parton-distribution functions, while NLO event generators use CTEQ6.1M. The generated partons are processed by the PYTHIA [97] parton-showering and hadronization algorithms into final-state particles, which are then processed with a full simulation of the CDF II detector. The effects of the parton shower and hadronization are included in all of the production-level results.

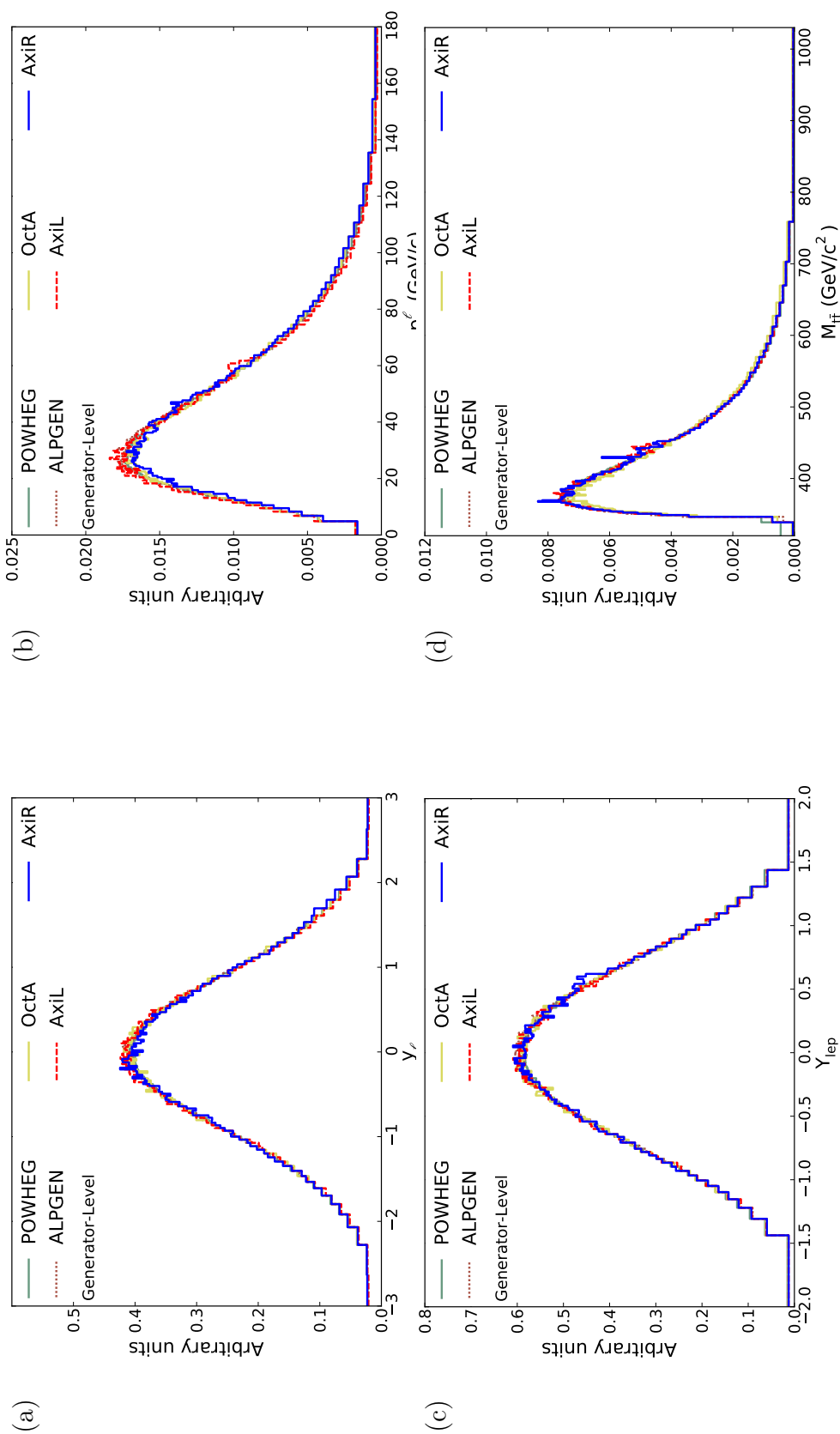


Figure 4.5. Several production-level distributions of simulated $t\bar{t}$ events. Figure (a) shows the distribution of the lepton rapidity y_{ℓ} without charge weighting. Figures b and d respectively show the distribution of the transverse momentum of the lepton, p_T^{ℓ} , and the invariant mass of the $t\bar{t}$ system, $M_{t\bar{t}}$. Figure c) shows the rapidity distributions of the leptonically-decaying top quark. All distributions indicate good agreement between the different models.

4.4 Sample Composition

The contribution of each processes in the data sample is determined using a combination of theoretical calculation, simulation, and *in situ* measurement known as ‘Method 2’ [19]. The composition of the data from each trigger with a particular number of tight jets is determined individually. This accommodates the different acceptances, efficiencies, and background rates of each lepton trigger. These are summed to provide the overall composition of the sample.

The sample of events from a given trigger with a given jet multiplicity is divided into subsamples by the number of *b*-tagged jets: the *zero*-, *one*- and *two-or-more tag* samples. The union of these three subsamples is referred to as the *pretag* sample. The composition of the pretag sample is determined first. Then, individually, a similar procedure is applied to determine the compositions of the one- and two-or-more-tag samples. The difference between these yields provides the composition of the zero-tag region. The procedure, outlined below, is virtually identical for the pretag and tagged regions.

The yields of the $t\bar{t}$ signal and small electroweak backgrounds from single top, diboson, and $Z + \text{jets}$ are estimated by assuming the Standard Model production cross-section ($\sigma_{p\bar{p}\rightarrow X}$, Tbl. 4.3), the sample luminosity ($\int \mathcal{L} \cdot dt$), and several efficiencies and scale factors:

$$N_{p\bar{p}\rightarrow X} = \sigma_{p\bar{p}\rightarrow X} \times \epsilon_{\text{MC}} \times \frac{\epsilon_{z0}^{\text{data}}}{\epsilon_{z0}^{\text{MC}}} \times \frac{\epsilon_{\ell}^{\text{data}}}{\epsilon_{\ell}^{\text{MC}}} \times \epsilon_{\text{trigger}} \times \epsilon_{\text{tag}} \times \int \mathcal{L} \cdot dt. \quad (4.1)$$

The simulated efficiency (before considering *b*-tag information) is given by ϵ_{MC} . This is corrected by the measured trigger efficiency, $\epsilon_{\text{trigger}}$, and two scale factors: $\epsilon_{\ell}^{\text{data}}/\epsilon_{\ell}^{\text{MC}}$ corrects the simulated lepton identification and reconstruction efficiency to match the performance of the physical detector, and $\epsilon_{z0}^{\text{data}}/\epsilon_{z0}^{\text{MC}}$ does the same for the vertex-finding efficiency. In the tagged samples, ϵ_{tag} is the *b*-tagging efficiency. Because the

Table 4.3. The theoretical cross-sections used for top-quark pair production and those background processes whose yields are not derived from data [19].

Process	Cross-Section (pb)		
$t\bar{t}$	7.4	\pm	1.1
Single Top - t Channel	1.98	\pm	0.25
Single Top - s Channel	0.88	\pm	0.11
WW	12.4	\pm	0.25
WZ	3.96	\pm	0.06
ZZ	1.58	\pm	0.05
Z + Jets	787.4	\pm	85

triggering and lepton reconstruction efficiency vary for each subdetector, individual efficiencies and scale factors are applied for each. Uncertainties are propagated from all of these sources.

Next, the non- W/Z background contribution is estimated by removing the minimum E_T^{miss} requirement and examining the resultant E_T^{miss} distribution. This distribution is fit to the sum of three templates, corresponding to the non- W/Z model, the W + jets model, and the top/electroweak models. The variable parameter in this fit is the non- W/Z fraction $F_{\text{Non-}W}$:

$$N_{\text{Non-}W}^{\text{pretag}} = F_{\text{Non-}W} \cdot N_{\text{pretag}}. \quad (4.2)$$

Systematic uncertainties are estimated by taking the largest deviation of several alternate fits from the nominal value, where the alternate fits are performed by varying the binning, the range of the E_T^{miss} fit, and lepton isolation requirements.

The total W + jets yield then follows from the assumption that the remaining data must be attributable to W + jets. Finally, the relative contributions of W + HF and W + LF are calibrated to the measured heavy-flavor jet production rate. In the pretag sample,

$$N_{W+\text{HF}}^{\text{pre}} = N_{W+\text{jets}}^{\text{pre}} \times K_F \times f_{HF} \quad (4.3)$$

where

$$f_{HF} = \frac{N_{b,MC}^{W+Jets}}{N_{jets,MC}^{W+Jets}} \quad (4.4)$$

is the heavy-flavor fraction predicted by simulation, and

$$K_F = \frac{F_{j,data}^{b,events}}{F_{j,MC}^{b,events}} \quad (4.5)$$

is a data-derived correction factor for the heavy-flavor fraction. This calibration factor is intended to account for higher-order corrections to the heavy-flavor production rate, gluon-splitting processes, etc. Each of the heavy-flavor processes (Wc , $Wb\bar{b}$ and $Wc\bar{c}$) has an associated heavy-flavor fraction and in principal each of these processes might require a different K_F . However, a uniform correction factor of $K_F = 1.5 \pm 0.3$ suffices for all heavy-flavor processes.

The procedure in the tagged sample is very similar. The sideband which provides the non- W/Z templates suffers from diminished statistics when a b -tagged jet is required; to cope with this, templates for the tagged fits are produced by applying a tag-weighting procedure to pretag non- W/Z events. The tag-weighting procedure is much like that used for Monte Carlo samples as described in Section 3.5.3, but applies only the mistag matrices. For the $W + jets$ contribution, the heavy-flavor jet production rate must account for the tag efficiencies:

$$N_{W+HF}^{\text{tag}} = N_{W+jets}^{\text{tag}} \times \frac{\epsilon_{\text{tag}}^{W+HF}}{\epsilon_{\text{tag}}^{W+jets}} \times K_F \times f_{HF} \quad (4.6)$$

where $\epsilon_{\text{tag}}^{W+HF}$ and $\epsilon_{\text{tag}}^{W+jets}$ are the tagging efficiencies of heavy-flavor and inclusive $W + jets$ events, respectively. Since inclusive $W + jets$ production is a superset of heavy-flavor production, $\epsilon_{\text{tag}}^{W+HF}$ depends on K_F and f_{HF} .

Table 4.4. The estimated yield of processes which produce events in the signal region, compared to the observed number of events.

Process	Prediction		
$W+HF$	481	\pm	178
$W+LF$	201	\pm	72
$Z+jets$	34	\pm	5
Single top	67	\pm	6
Diboson	36	\pm	4
Non- W/Z	207	\pm	86
All backgrounds	1026	\pm	210
$t\bar{t}$ (7.4pb)	2750	\pm	426
Total prediction	3776	\pm	476
Observed	3864		

4.4.1 Signal Region: Yields and Validation

Reapplying the E_T^{miss} requirement after the procedure outlined above produces the predicted composition of the signal region. The yields of the i 'th process, as estimated above with no E_T^{miss} requirement, are propagated to the signal region ($E_T^{\text{miss}} > 20$ GeV) by assuming the yield ratio expected of that component's model:

$$N_{\text{data}}^i (E_T^{\text{miss}} > 20) = N_{\text{data}}^i (E_T^{\text{miss}} > 0) \times \frac{N_{\text{model}}^i (E_T^{\text{miss}} > 20)}{N_{\text{model}}^i (E_T^{\text{miss}} > 0)}. \quad (4.7)$$

The results are shown in Table 4.4.

To validate that the data is described well by this prediction, a number of kinematic distributions can be examined which display some distinction between top-quark pairs and background processes. First, the transverse energies of the jets are ranked in descending order in E_T . The E_T distributions for the first four jets are shown in Figure 4.6. Each plot also shows the estimated probability that the measured distribution was produced by the predicted distribution, generated using the Kolmogorov-Smirnov test [98]. This test is particularly sensitive to disagreements that produce skewed distributions, as would be expected were the sample compo-

sition not correct. The probabilities include only the statistical uncertainty from the data sample, and not the systematic uncertainties on the sample composition. Reasonable agreement is seen in all four cases.

Also shown are two distributions associated with the lepton itself: the lepton transverse momentum (p_T^ℓ , Fig. 4.7a) and the vertex-corrected pseudorapidity (η_ℓ , Fig. 4.7b). The distribution of the missing transverse energy, which is particularly powerful for distinguishing the non- W/Z background from the remaining processes, is shown in Figure 4.7c. Finally, Figure 4.7d displays the distribution of H_T . All of these distributions show reasonable agreement between data and prediction.

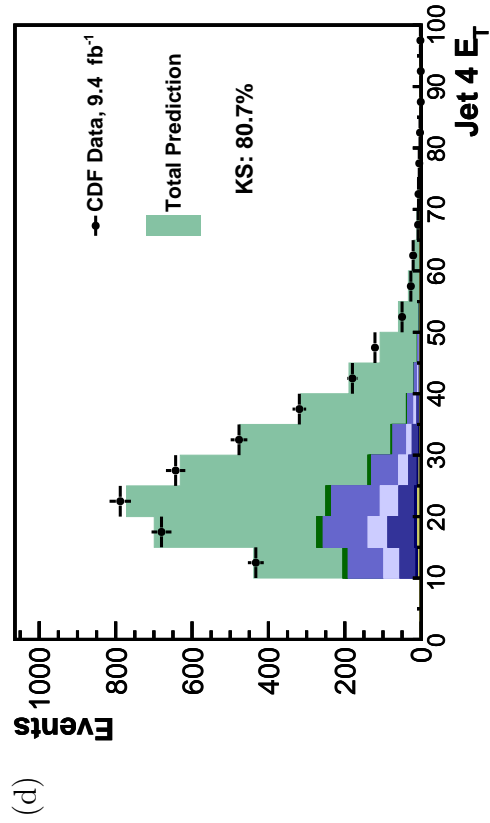
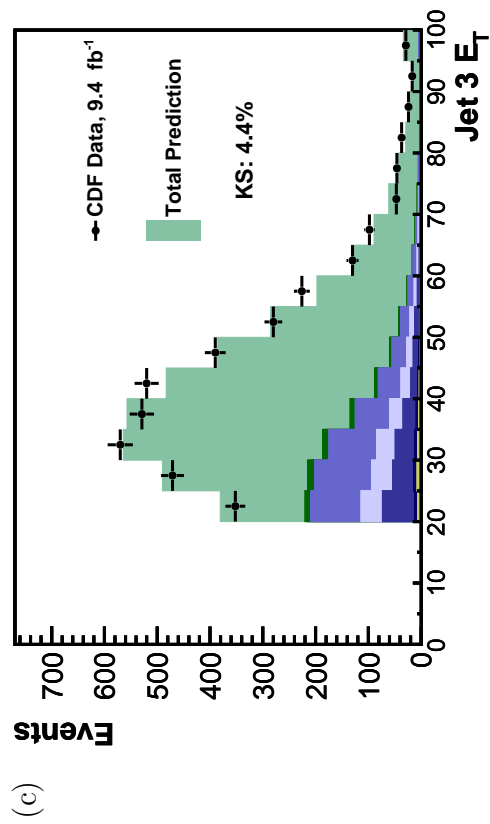
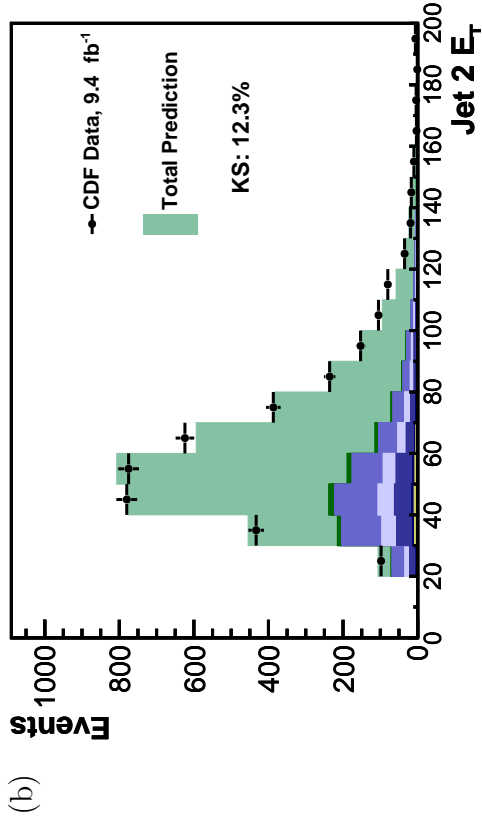
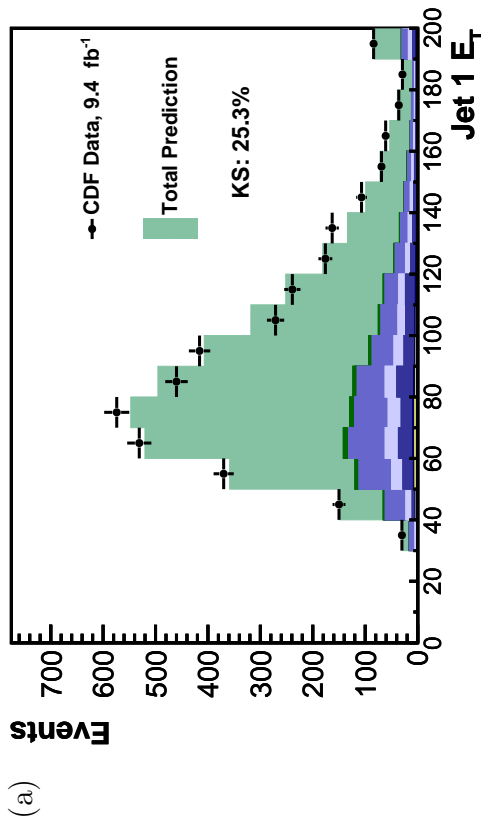


Figure 4.6. The transverse energies of the first four jets, where the jets are ranked by descending order in E_T . Figure (a) shows the E_T of the first jet, (b) the second, (c) the third, and (d) the fourth. In all cases the distribution of the observed CDF data agrees well with the prediction.

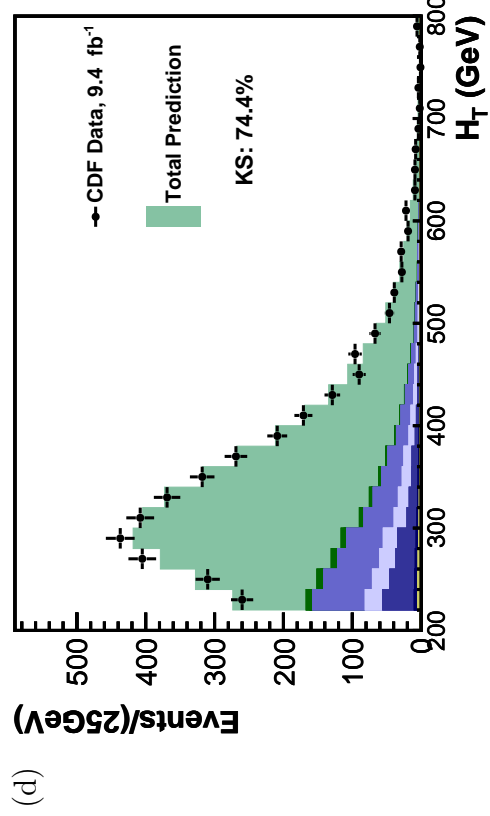
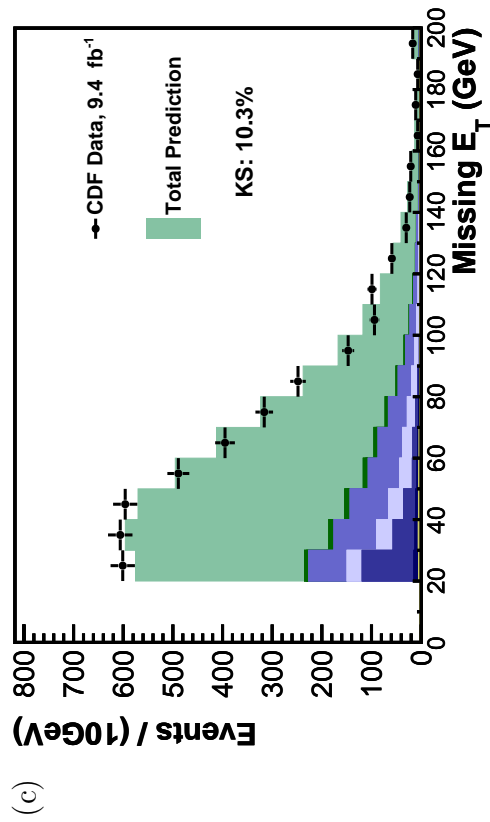
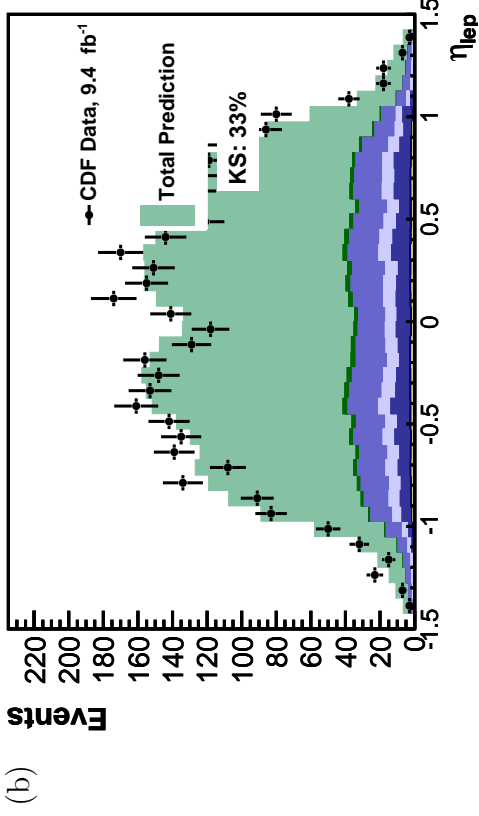
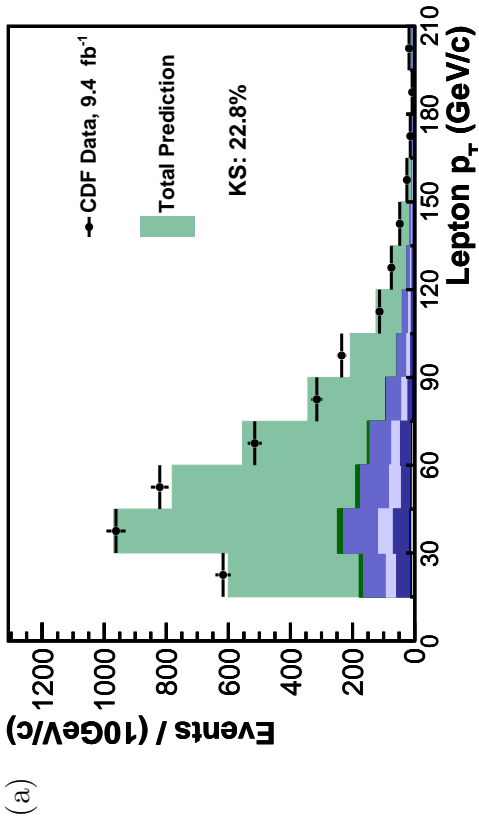


Figure 4.7. Additional validation histograms. Figure (a) and (b) show the distributions of the transverse momentum p_T^ℓ of the lepton and its vertex-corrected pseudorapidity η^ℓ . Figure (c) shows E_T^{miss} , and (d) the distribution of H_T . In both the leptonic variables (p_T^ℓ , η^ℓ) and the macroscopic variables (E_T^{miss} , H_T), good agreement is seen between the measured CDF data and prediction.

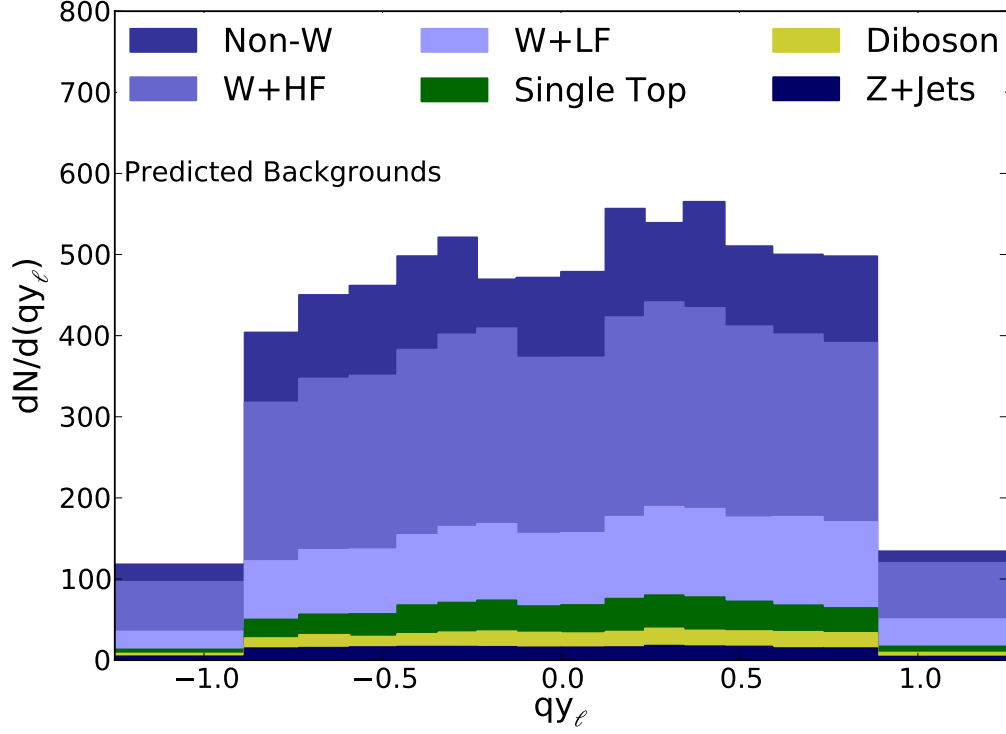


Figure 4.8. The distribution of qy_ℓ for the predicted backgrounds.

4.5 Asymmetries of the Backgrounds

Background processes are expected to contribute a nonzero asymmetry to the data-level result. The dominant background is W +jets, and both W +HF and W +LF are asymmetric. Additionally, the small background contributions from Z +jets and single-top-quark production can be expected to have an inherent asymmetry as well. The overall effect can be readily seen in Figure 4.8, the distribution of qy_ℓ for the predicted backgrounds alone.

The total asymmetry of a sample composed of several different processes may be written in terms of the yields and asymmetries of each individual process:

$$A_{\text{FB}}^\ell = \frac{\sum_{i=0} N_i \times A_{\text{FB}}^{i,\ell}}{\sum_{i=0}^M N_i} \quad (4.8)$$

Table 4.5. Asymmetries and yields of the dominant background processes in the signal region. The final column is the relative contribution of that process to the total background asymmetry.

CDF Run II Preliminary $\int \mathcal{L} = 9.4/\text{fb}$			
Background	Yield	Asymmetry	Relative Contribution
Non- W/Z	206.6	0.019	0.071
$W + \text{HF}$	481.3	0.032	0.280
$W + \text{LF}$	200.8	0.124	0.454
Other*	137.0	0.078	0.195
Total	1025.7	0.054	

*Other: Single Top, Diboson, $Z+\text{Jets}$

where N_i is the yield of the i 'th process and $A_{\text{FB}}^{i,\ell}$ its asymmetry. Table 4.5 shows these parameters for the major background processes in the signal region. The final column contains the fractional contribution of that process to the total background asymmetry, defined as

$$f_i = \frac{N_i \times A_{\text{FB}}^{i,\ell}}{N_{\text{bkg}} \times A_{\text{FB}}^{\text{bkg},\ell}}.$$

The bulk of the background asymmetry is produced by $W + \text{jets}$, with $W + \text{LF}$ alone accounting for nearly half the predicted value. Interference between the photon and the left-handed W naturally tends to produce a negative lepton asymmetry. A stronger effect, however, results from PDFs: u quarks typically carry more momentum than d quarks, and both carry more momentum than gluons. Thus, both processes of Figure 4.9 produce a positive asymmetry in the W ; this induces a corresponding positive asymmetry in the lepton. Because the momentum imbalance is greater in qg -initiated events, which preferentially produce W bosons in association with light jets, the asymmetry of $W + \text{LF}$ is greater than that of $W + \text{HF}$.

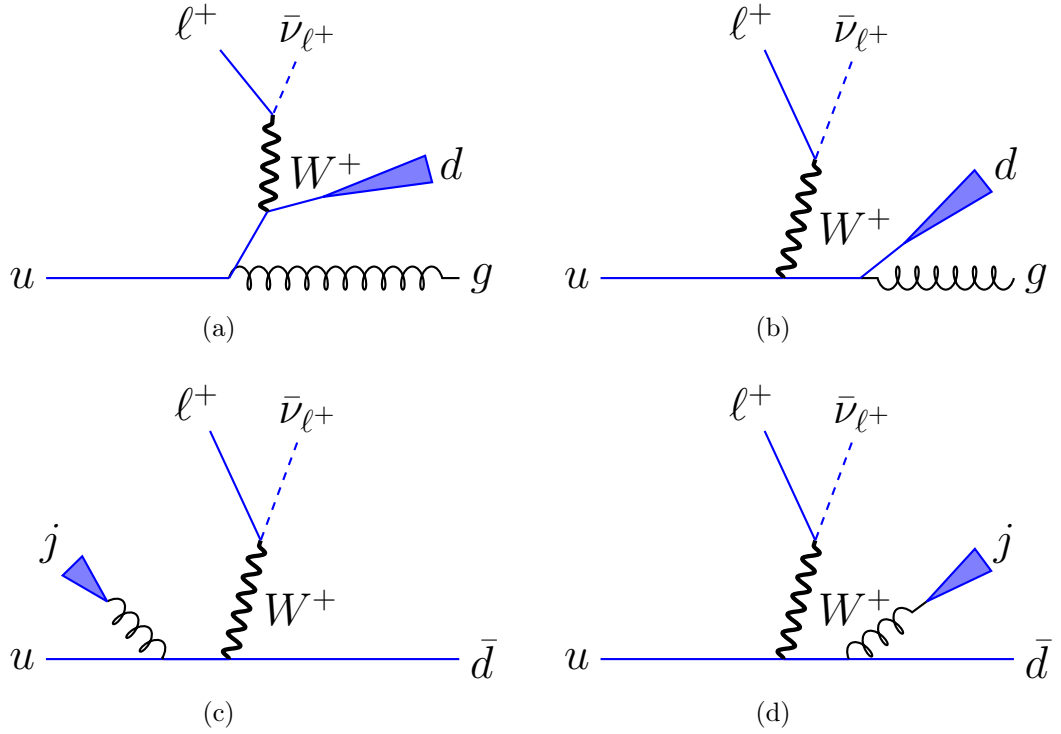


Figure 4.9. Production mechanisms for a positive W boson in association with one jet. Contributions initiated by ug are shown in Figure (a) and (b); analogous processes exist for the other light-quark flavors. Alternatively, a jet may be produced from initial-state radiation (d), (c). Tree-level production of larger jet multiplicities occurs through additional initial- and final-state radiation and gluon-splitting.

4.5.1 Control Sample I: $W+1$ Jet

The measurement of the leptonic forward-backward asymmetry A_{FB}^ℓ in top-quark pairs relies crucially on the charge-determination of the lepton and on accurate modeling of any asymmetries of the detector itself. These may be precisely tested by examining the leptonic asymmetry in a large and well-understood sample: events in which a W boson is produced in conjunction with exactly one jet. This is also the simplest context in which W production displays all of the physics that produce the asymmetry of the W + jets background in the signal region. The predicted asymmetry in $W+1$ jet exhibits dependences on both p_{T}^ℓ and η_ℓ ; good agreement is strongly indicative of accurate modeling of both detector artifacts and the W + jets background.

Table 4.6. The estimated yield of processes which produce events in the $W+1$ jet control sample, compared to the observed number of events. The overall $W + \text{jets}$ normalization is chosen so that the number of predicted and observed events are equal.

CDF Run II Preliminary $\int \mathcal{L} = 9.4/fb$			
Process	Prediction		
$W+\text{HF}$	76,025	\pm	10,489
$W+\text{LF}$	671,684	\pm	31,458
$Z+\text{jets}$	19,117	\pm	1,344
Single top	458	\pm	29
Diboson	3,205	\pm	203
Non- W/Z	19,303	\pm	12,187
$t\bar{t}$ (7.4pb)	154	\pm	23
Observed	789,946		

This sample begins from the portion of the $W + \text{jets}$ selection having exactly one tight jet. No b -tagging requirement is made. To reject non- W/Z backgrounds, we construct a variable known as the 'minimum leptonic W mass':

$$M_{\ell W}^{\min} = E_{\text{T}}^{\text{miss}} \times p_{\text{T}}^{\ell} \times [1 - \cos(\Delta\phi_{\ell\nu})] \quad (4.9)$$

where $\Delta\phi_{\ell\nu}$ is the difference in azimuthal angles between the lepton and missing transverse energy. This variable originates as an enhancement to a more traditional alternative, the transverse mass of the W . It is derived by assuming that $E_{\text{T}}^{\text{miss}}$ represents the transverse component of the momentum of a massless neutrino, and then solving for the neutrino z -momentum that would minimize the invariant mass of the lepton-neutrino system.

For events in which the identified lepton and $E_{\text{T}}^{\text{miss}}$ are produced by an on-shell W boson, $M_{\ell W}^{\min}$ tends to be large. On the other hand, non- W/Z events tend to cluster in the region of small $M_{\ell W}^{\min}$. In the $W+1$ jet sample, the minimum leptonic W mass is required to satisfy $M_{\ell W}^{\min} > 20$ GeV. The composition of the nearly 800,000 events which remain is determined by the same procedure as for the signal region, except that the overall $W + \text{jets}$ normalization is chosen so that the number of predicted

and observed events are exactly equal after the $E_{\text{T}}^{\text{miss}}$ cut is applied. The yields of all contributing processes are shown in Table 4.6.

Figure 4.10a and 4.10c show the predicted and observed distributions of p_{T}^{ℓ} and η_{ℓ} in the $W+1$ jet sample. Figure 4.10b and 4.10d show the dependence of A_{FB}^{ℓ} on these variables. To quantify these dependences simply, the sample is divided into regions of small ($p_{\text{T}}^{\ell} < 60$ GeV) and large ($p_{\text{T}}^{\ell} \geq 60$ GeV) transverse momentum, with asymmetries as listed in Table 4.7. Similarly, the sample is divided into central ($|\eta_{\ell}| < 0.75$) and noncentral ($|\eta_{\ell}| \geq 0.75$) regions in Table 4.8.

Excellent agreement is seen across the entire range of both variables. The comparison is limited by systematic uncertainties on the prediction, which are dominated by uncertainty on the heavy-flavor fraction. Statistical limitations of the $W + \text{jets}$ models also contribute at large values of p_{T}^{ℓ} and $|\eta_{\ell}|$.

Table 4.7. The qy_{ℓ} asymmetry in the $W+1$ jet sample, compared to Standard Model expectations, for small and large lepton p_{T}^{ℓ} .

	$p_{\text{T}}^{\ell} < 60 \text{ GeV}/c$	$p_{\text{T}}^{\ell} \geq 60 \text{ GeV}/c$
Observed data	0.083 ± 0.001	-0.009 ± 0.004
SM prediction	0.089 ± 0.004	-0.001 ± 0.013
Data minus prediction	-0.006 ± 0.004	-0.008 ± 0.014

Table 4.8. The qy_{ℓ} asymmetry in the $W+1$ jet sample, compared to Standard Model expectations, for small and large $|\eta_{\ell}|$.

	$ \eta_{\text{lep}} < 0.75$	$ \eta_{\text{lep}} \geq 0.75$
Observed data	0.059 ± 0.001	0.124 ± 0.002
SM prediction	0.063 ± 0.005	0.134 ± 0.008
Data minus prediction	-0.004 ± 0.005	-0.010 ± 0.008

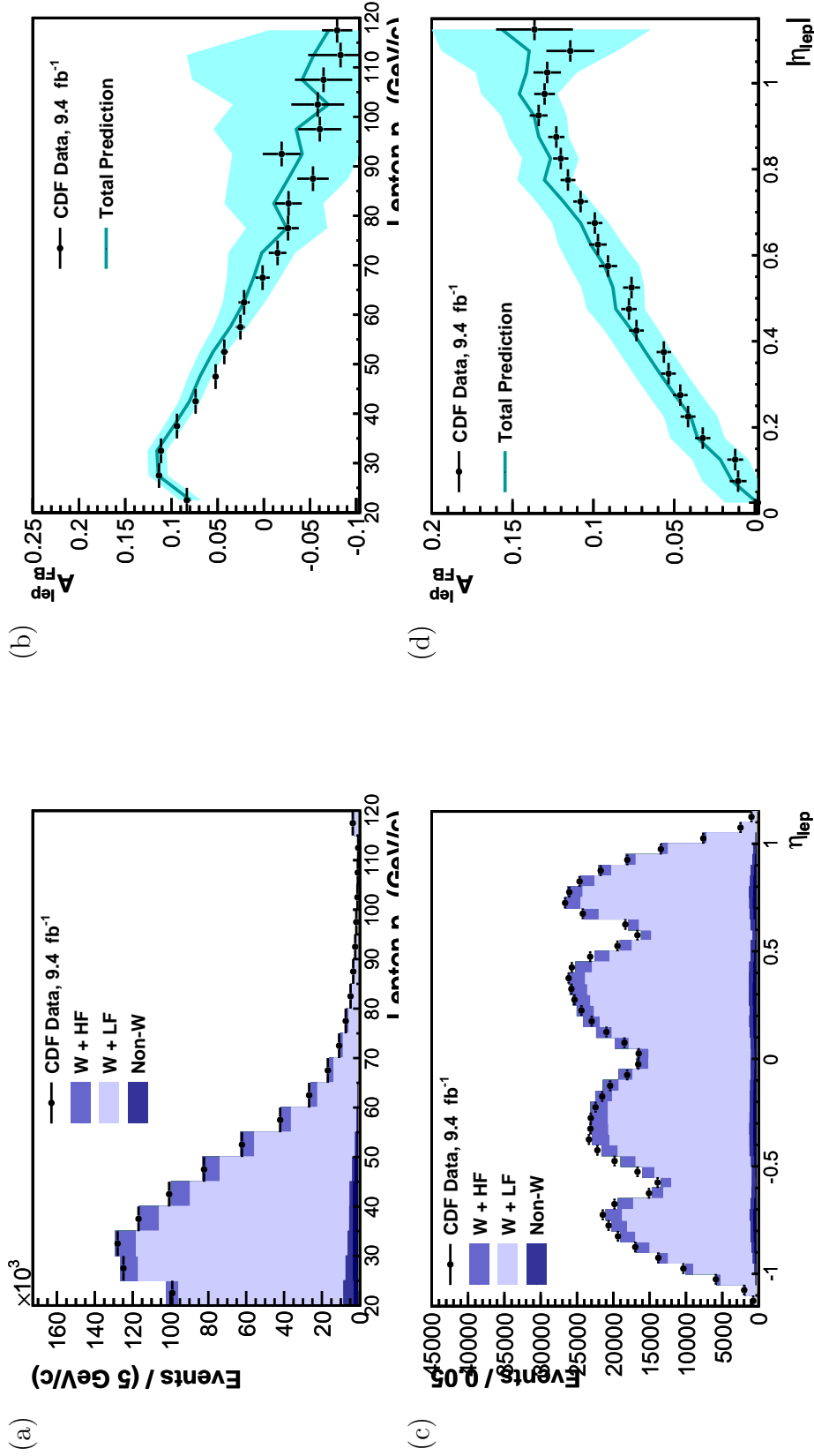


Figure 4.10. Plots of the $W+1$ jet control region. Figure (a) shows the observed and predicted distributions of p_T^{ℓ} , and Figure (c) of the vertex-corrected η_{ℓ} . Figure (b) and (d) show the dependence of A_{FB}^{ℓ} on the lepton p_T^{ℓ} and η_{ℓ} respectively. The colored bands around the predicted A_{FB}^{ℓ} indicate the $\pm 1\sigma$ uncertainties on the prediction, which are dominated by uncertainties on the heavy-flavor fraction. In all cases the observed CDF data agrees with the prediction well within uncertainties.

4.5.2 Control Sample II: Zero Tag

The $W+1$ jet sample provides a valuable check of the modeling of charge identification and detector asymmetries. Additionally, it is evidence that the $W +$ jets backgrounds are well-understood. However, larger jet multiplicities entail more intricate production mechanisms, and the higher average energy of events in the signal region does probe somewhat different PDF parameters. Conceivably, the modeling might become more sensitive to higher-order corrections or to a myriad of other effects.

A second control region is used to validate that any such effects are small, and that the background and its asymmetries are properly modeled. To replicate the kinematics of the signal region as closely as possible, this control region is comprised of events that otherwise meet the signal selection criteria of Section 4.1.2 but have exactly zero b -tagged tight jets. This ‘zero-tag’ selection is statistically independent of the signal region. Although in most respects the two are comparable, the zero-tag region is dominated by backgrounds and relatively depleted of signal. The estimated composition is shown in Table 4.9. Of the 9,904 zero-tag events, under 2,000 are

Table 4.9. The estimated yield of processes which produce events in the zero-tag control sample, compared to the observed number of events.

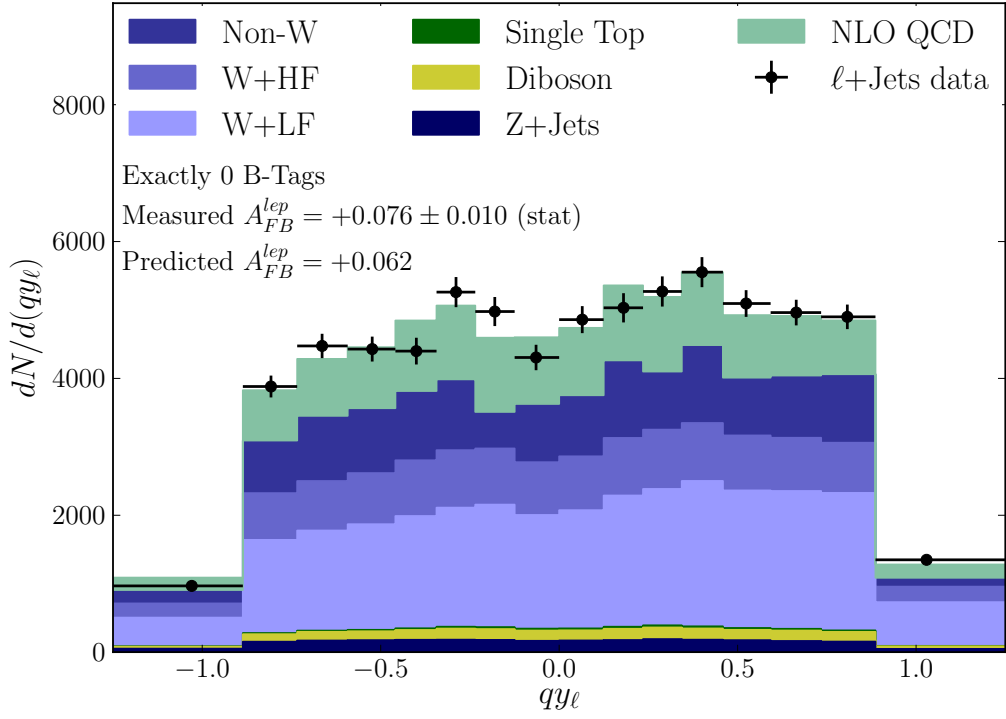
CDF Run II Preliminary $\int \mathcal{L} = 9.4/\text{fb}$			
Process	Prediction		
$W+\text{HF}$	1656	\pm	595
$W+\text{LF}$	3801	\pm	1158
$Z+\text{jets}$	363	\pm	214
Single top	50	\pm	4
Diboson	301	\pm	30
Non- W/Z	1828	\pm	525
All backgrounds	8000	\pm	1420
$t\bar{t}$ (7.4pb)	1969	\pm	254
Total prediction	9969	\pm	1442
Observed	9904		

Table 4.10. Comparison of the predicted and measured asymmetries in the zero-tag sample. “Signal + backgrounds” is the predicted asymmetry when the A_{FB}^ℓ of the $t\bar{t}$ component is fixed to 0.070.

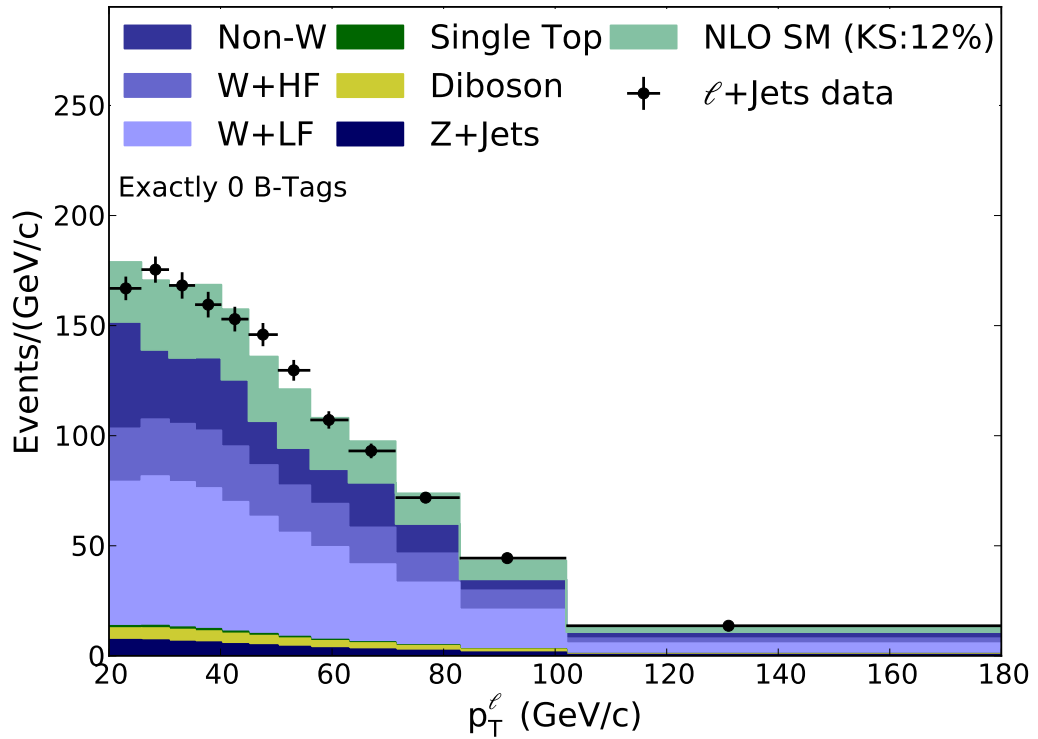
CDF Run II Preliminary $\int \mathcal{L} = 9.4/\text{fb}$	
	Asymmetry
NLO SM	0.017
Backgrounds	0.074
NLO SM + backgrounds	0.062
Signal + backgrounds	0.073
CDF Data	0.076 ± 0.010

expected to be top-quark pairs.

The distributions of qy_ℓ and p_T^ℓ are shown in Figure 4.11. As in the $W+1$ jet sample, there is good agreement between the data and prediction. The asymmetries in the zero-tag sample are summarized in Table 4.10. The predicted A_{FB}^ℓ in the zero-tag sample is 0.062; the asymmetry in the data is 0.076 ± 0.011 (stat.). This is already an acceptable level of agreement. A small portion of the zero-tag selection does consist of top-quark pairs; as a further check, we will anticipate the measurement of the background-subtracted asymmetry in the signal region ($A_{\text{FB}}^\ell = 0.070$; see Section 5.3.1). If the asymmetry of top-quark pairs is taken to be this value instead of that given by POWHEG, the predicted A_{FB}^ℓ in the zero-tag sample becomes 0.073. The agreement between the data and this modified prediction is consistent well within the statistical error.



(a)



(b)

Figure 4.11. Comparisons of measured and predicted distributions in the zero-tag control region. Figure (a) shows qy_ℓ , the charge-weighted lepton rapidity. Figure (b) shows the transverse momentum of the lepton, p_T^ℓ .

CHAPTER V

The Leptonic Asymmetry in Top-Quark Pairs

This chapter proceeds to the primary measurement of this analysis: the asymmetry A_{FB}^{ℓ} of leptons produced by the decay of top-quark pairs.

A technique to correct for the steeply-falling lepton acceptance is then developed. This is accomplished by separating the charge-weighted lepton rapidity into a symmetric part and a qy_{ℓ} -dependent asymmetry. It is shown that the acceptance corrections to these two parts decouple and that they may therefore be treated independently. A model function is used to parametrize the qy_{ℓ} -dependent asymmetry, and from this the inclusive A_{FB}^{ℓ} at production is recovered. The procedure is validated in the benchmark models.

Finally, the correction procedure is applied to the data in the signal region. Systematic uncertainties are evaluated and several cross-checks on the result are performed.



Figure 5.1. The chapter headpiece.

5.1 Methodology

The raw asymmetry in the signal region includes contributions from non- $t\bar{t}$ backgrounds and is further distorted by limited detector acceptance. Both of these effects must be corrected in order to determine the asymmetry at production. Contributions from the backgrounds, which are well-understood (Sec. 4.5.2), are removed by subtracting the most probable background contribution in each bin.

Acceptance corrections must accommodate the steep decline of the acceptance in y_ℓ . The distributions of simulated events as a function of qy_ℓ are shown in Figure 4.4a for each of the benchmark models; the corresponding asymmetries in each bin are shown in Figure 4.4b. The vertical lines indicate the limits of the lepton acceptance. About 80% of the total cross-section lies in the accepted region $|qy_\ell| \leq 1.25$. However, the 20% of events that fall outside the detector's acceptance are also predicted to have the largest asymmetry. The recovery of this contribution to the production-level inclusive A_{FB}^ℓ must necessarily rely on extrapolation into this unmeasured region.

5.1.1 Rapidity Decomposition

The extrapolation relies on a separation of the signed rapidity distribution $N(qy_\ell)$ into a symmetric part $\mathcal{S}(qy_\ell)$ and a qy_ℓ -dependent asymmetry $\mathcal{A}(qy_\ell)$ [99], defined as

$$\mathcal{S}(qy_\ell) = \frac{N(qy_\ell) + N(-qy_\ell)}{2} \quad (5.1a)$$

$$\mathcal{A}(qy_\ell) = \frac{N(qy_\ell) - N(-qy_\ell)}{N(qy_\ell) + N(-qy_\ell)} \quad (5.1b)$$

in the range $qy_\ell \geq 0$. This form is equivalent to the original signed rapidity distribution – the pair of functions $\mathcal{S}(qy_\ell)$ and $\mathcal{A}(qy_\ell)$ may be inverted to recover $N(qy_\ell)$:

$$N(qy_\ell) = \begin{cases} \mathcal{S}(qy_\ell) \times (1 + \mathcal{A}(qy_\ell)) & qy_\ell > 0 \\ \mathcal{S}(-qy_\ell) \times (1 - \mathcal{A}(qy_\ell)) & qy_\ell < 0. \end{cases} \quad (5.2)$$

This in turn may be integrated to recover the total number of forward or backward events:

$$N(qy_\ell > 0) = \int_0^\infty dqy_\ell \mathcal{S}(qy_\ell) \times (1 + \mathcal{A}(qy_\ell)) \quad (5.3a)$$

$$N(qy_\ell < 0) = \int_0^\infty dqy_\ell \mathcal{S}(qy_\ell) \times (1 - \mathcal{A}(qy_\ell)) \quad (5.3b)$$

which then yields the inclusive asymmetry, written in terms of $\mathcal{S}(qy_\ell)$ and $\mathcal{A}(qy_\ell)$:

$$A_{\text{FB}}^\ell = \frac{N(qy_\ell > 0) - N(qy_\ell < 0)}{N(qy_\ell > 0) + N(qy_\ell < 0)} \quad (5.4a)$$

$$= \frac{\int_0^\infty dqy_\ell [\mathcal{A}(qy_\ell) \times \mathcal{S}(qy_\ell)]}{\int_0^\infty dqy_\ell \mathcal{S}(qy_\ell)}. \quad (5.4b)$$

5.1.2 Bin-by-bin Acceptance Corrections

Leptons are experimentally very well-resolved: events with y_ℓ so mismeasured as to populate the wrong bin are a negligible effect. In the accepted region $|qy_\ell| < 1.25$, then, multiplicative acceptance corrections adequately recover the production-level distribution of qy_ℓ without any unsmearing. In this section, multiplicative acceptance corrections to $N(qy_\ell)$ will be reformulated as corrections that act directly on $A_{\text{FB}}^\ell(qy_\ell)$ and $S(qy_\ell)$. Measured distributions will be represented by unsuperscripted variables, and production-level distributions will be labeled as such.

Let $C(qy_\ell)$ be the multiplicative acceptance correction factors on $N(qy_\ell)$:

$$N^{\text{prod}}(qy_\ell) = C(qy_\ell) \times N(qy_\ell). \quad (5.5)$$

Using this, $A^{\text{prod}}(qy_\ell)$ and $S^{\text{prod}}(qy_\ell)$ may be written in terms of the measured $N(qy_\ell)$ and acceptance correction factors:

$$A^{\text{prod}}(qy_\ell) = \frac{C(qy_\ell) N(qy_\ell) - C(-qy_\ell) N(-qy_\ell)}{C(qy_\ell) N(qy_\ell) + C(-qy_\ell) N(-qy_\ell)} \quad (5.6a)$$

$$S^{\text{prod}}(qy_\ell) = \frac{C(qy_\ell) N(qy_\ell) + C(-qy_\ell) N(-qy_\ell)}{2}. \quad (5.6b)$$

To simplify these expressions, the acceptance correction factors themselves may be separated into a symmetric acceptance correction $S^C(qy_\ell)$ and an acceptance asymmetry $A^C(qy_\ell)$. This is exactly analogous to Section 5.1.1:

$$A^C(qy_\ell) = \frac{C(qy_\ell) - C(-qy_\ell)}{C(qy_\ell) + C(-qy_\ell)} \quad (5.7a)$$

$$S^C(qy_\ell) = \frac{C(qy_\ell) + C(-qy_\ell)}{2}, \quad (5.7b)$$

with the original acceptance correction factor easily recovered:

$$C(qy_\ell) = \begin{cases} S^C(qy_\ell) \times (1 + A^C(qy_\ell)) & qy_\ell > 0 \\ S^C(-qy_\ell) \times (1 - A^C(qy_\ell)) & qy_\ell < 0. \end{cases} \quad (5.8)$$

Substituting this into Equation 5.6 and simplifying,

$$A^{\text{prod}}(qy_\ell) = \frac{A_{\text{FB}}^\ell(qy_\ell) + A^C(qy_\ell)}{1 + A^C(qy_\ell) A_{\text{FB}}^\ell(qy_\ell)} \quad (5.9a)$$

$$S^{\text{prod}}(qy_\ell) = S^C(qy_\ell) S(qy_\ell) [1 + A^C(qy_\ell) A_{\text{FB}}^\ell(qy_\ell)] \quad (5.9b)$$

Table 5.1. Bin-by-bin values that are used in the extrapolation procedure. These quantities are measured in simulated events generated by POWHEG. The first column shows the bin range. The second column lists the predicted bin centroids, calculated as a weighted mean. The third column shows the asymmetries of the acceptance $A^C(qy_\ell)$ in each bin.

CDF Run II Preliminary $\int \mathcal{L} = 9.4/\text{fb}$		
$ qy_\ell $	Bin Center	$A^C(qy_\ell)$
[+0.00, +0.12)	0.065	-0.0042
[+0.12, +0.24)	0.180	-0.0113
[+0.24, +0.34)	0.289	-0.0044
[+0.34, +0.46)	0.400	-0.0055
[+0.46, +0.59)	0.524	-0.0050
[+0.59, +0.73)	0.664	-0.0002
[+0.73, +0.89)	0.807	-0.0034
[+0.89, +1.50]	1.029	-0.0013

In practice $A^C(qy_\ell) \ll 1$, as seen in Table 5.1. To a good approximation:

$$A^{\text{prod}}(qy_\ell) = A_{\text{FB}}^\ell(qy_\ell) + A^C(qy_\ell) \quad (5.10a)$$

$$S^{\text{prod}}(qy_\ell) = S^C(qy_\ell) S(qy_\ell). \quad (5.10b)$$

The acceptance corrections to the symmetric part and to the qy_ℓ -dependent asymmetry decouple. The bin-by-bin corrections act as a multiplicative factor on $S(qy_\ell)$ but as an additive offset on $A_{\text{FB}}^\ell(qy_\ell)$. Deviations from this behavior in the accepted region are on the order of one part per thousand of the measured asymmetry.

5.1.3 Extrapolation Procedure

Figure 5.2 shows the shape of the symmetric part (a) and qy_ℓ -dependent asymmetry (b) of the benchmark models. The shape of $\mathcal{S}(qy_\ell)$ is very similar across models, suggesting little or no dependence on either the top-quark production asymmetry or the polarization, while $A_{\text{FB}}^\ell(qy_\ell)$ captures the variation between models.

This suggests a strategy for extrapolating the asymmetry into the unmeasured region. If $\mathcal{A}(qy_\ell)$ can be robustly parametrized by some function $\mathcal{F}(qy_\ell)$, whose

parameters can be extracted in the accepted region, then the integral of Eq. (5.4) can be used to recover the production-level asymmetry. This also requires a prediction for $\mathcal{S}(qy_\ell)$. Since there is good agreement between different models, and $\mathcal{S}(qy_\ell)$ decouples from $\mathcal{A}(qy_\ell)$, use of the simulated $\mathcal{S}(qy_\ell)$ over the entire range of qy_ℓ is justified if it agrees with measured data in the accepted region.

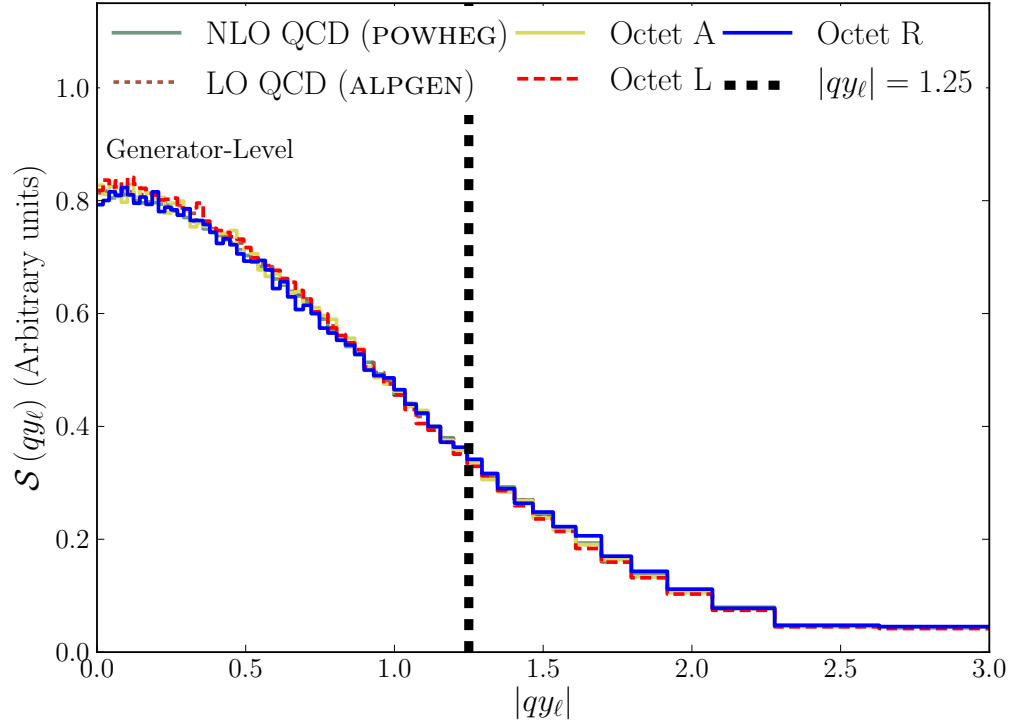
The model function $\mathcal{F}(qy_\ell)$ can be arbitrary – it need only reproduce $\mathcal{A}(qy_\ell)$ well enough that any mismodeling error is small compared to the statistical uncertainty of the data – and a candidate function can be proposed by inspection. The qy_ℓ -dependent asymmetries of the benchmark models all exhibit similar behavior: each appears to increase asymptotically with qy_ℓ , climbing from zero to some model-dependent saturation asymmetry $a \leq 1$ (Fig. 5.2b). This behavior is described adequately by the function

$$\mathcal{F}(qy_\ell) = a \tanh \left[\frac{1}{2} qy_\ell \right] \quad (5.11)$$

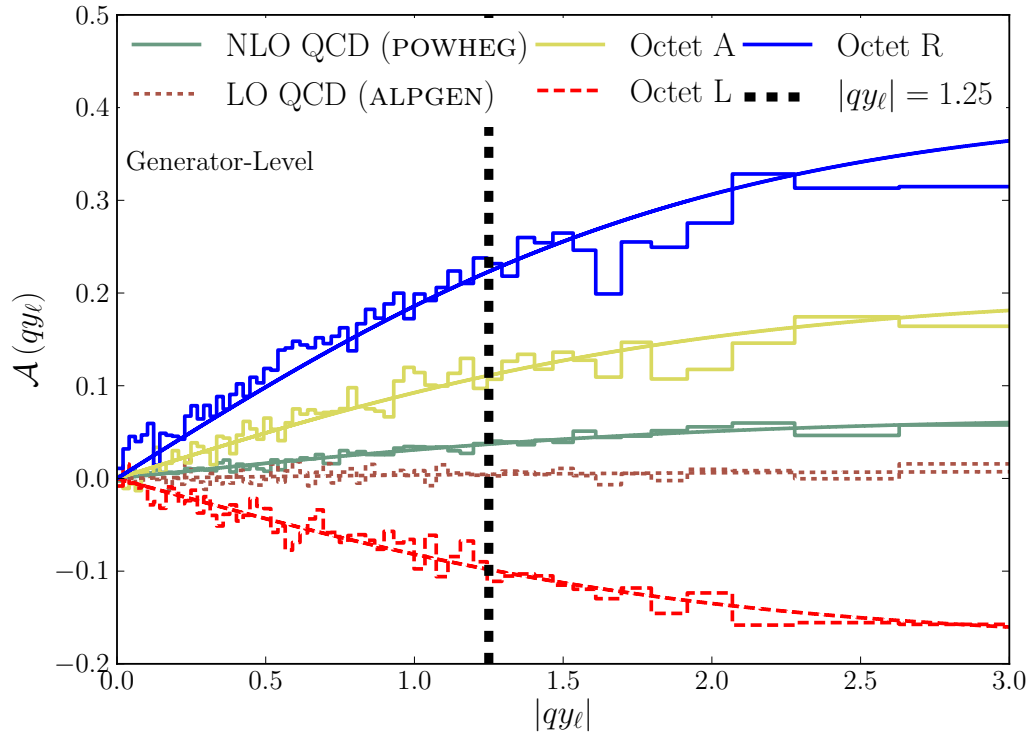
for all of the benchmark models.

Many other functions are also viable parametrizations; some are explored in Ref. [100]. With the choice of Eq. (5.11) as model function, the correction procedure is equivalent to a skew transformation acting on the binned asymmetries measured in data. This is not true of the more general functions explored in Ref. [100].

Table 5.2 shows the values of the fit parameter a at production level for each benchmark model. No parametrization can be expected to be completely model-independent. However, this particular parametrization reproduces the qy_ℓ -dependent asymmetry well for the models considered here. Notably, the dependence predicted by the POWHEG generator is accurately described ($\chi^2/\text{ndf} = 158/119$). It is therefore reasonable to expect this model function to be reliable for any scenario where the kinematic properties of top-quark pair production sufficiently resemble the Standard Model.



(a)



(b)

Figure 5.2. The symmetric part (a) and asymmetric part (b) of the production-level distribution of qy_ℓ for the benchmark models. Shown also are the best fits to Eq.(5.11). The vertical lines at $|qy_\ell| = 1.25$ indicate the limits of the lepton acceptance.

Table 5.2. Best-fit values of the parameter a for the benchmark models (Eq. (5.11); 119 d.f.).

CDF Run II Preliminary $\int \mathcal{L} = 9.4/\text{fb}$		
Model	a	χ^2/ndf
NLO QCD (POWHEG)	+0.067	1.33
LO SM	+0.008	1.06
Octet A	+0.200	1.38
Octet L	-0.177	1.12
Octet R	+0.402	3.37

5.1.4 Summary of the Correction Procedure

The procedure to extract the production-level A_{FB}^ℓ from data (also represented graphically in Figure 5.3) is then the following:

- (1) subtract the expected background contribution in each bin of qy_ℓ ;
- (2) using acceptances derived from POWHEG, perform bin-by-bin acceptance corrections on the background-subtracted data;
- (3) fit the acceptance-corrected $A_{\text{FB}}^\ell(qy_\ell)$ to the functional form $\mathcal{F}(qy_\ell)$ (Eq. (5.11));
- (4) integrate $\mathcal{F}(qy_\ell)$ with the $\mathcal{S}(qy_\ell)$ determined in simulation to recover the inclusive A_{FB}^ℓ .

The binning of qy_ℓ in the data is chosen so that POWHEG's predicted $\mathcal{S}(qy_\ell)$ equally populates each bin. The fit to $\mathcal{A}(qy_\ell)$ uses this binning with $\mathcal{F}(qy_\ell)$ evaluated at the predicted bin centers according to POWHEG, which are calculated as a weighted average of $|qy_\ell|$ in each bin (Tbl. 5.1)). Once the fit parameter a of Eq. (5.11) is obtained from the background-subtracted data using this binning, the integration of Eq. (5.4) is carried out using the 120-bin production-level $\mathcal{S}(qy_\ell)$ values from POWHEG.

To understand the effects of each correction stage, values of A_{FB}^ℓ will be produced at several levels of correction:

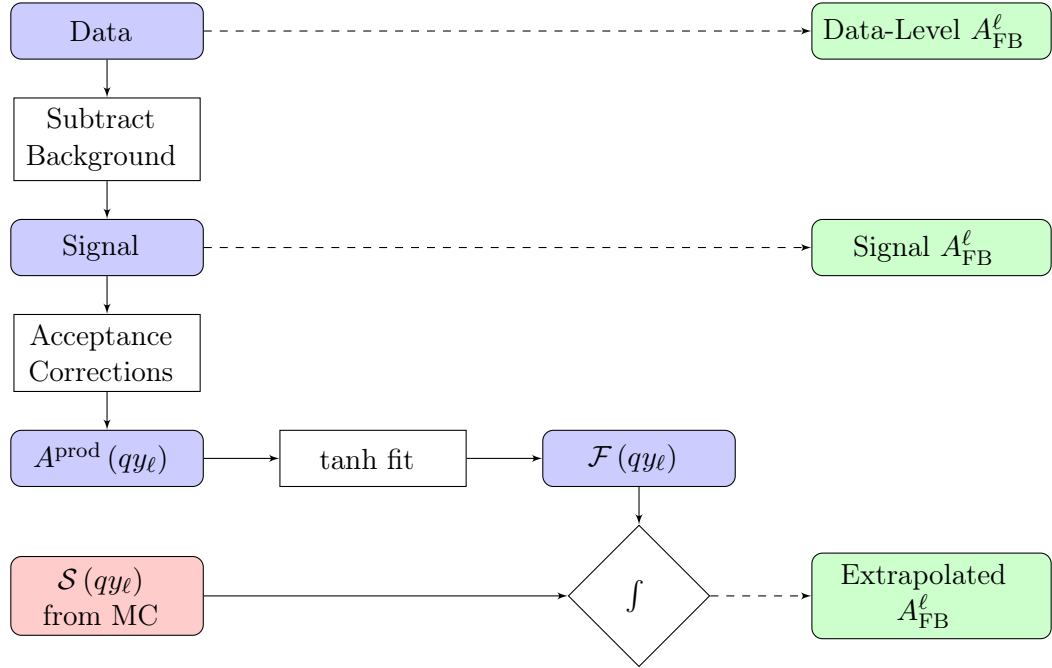


Figure 5.3. A graphical representation of the correction procedure. Blue and red boxes represent distribution derived from data and simulation, respectively. Unfilled boxes represent operations, and green boxes represent observable asymmetries at different correction levels.

- The *raw* or *data-level* measurement represents the complete and uncorrected signal selection. It includes both contributions from top-quark pairs and background processes, and has no corrections for finite detector acceptance.
- The *signal* or *background-subtracted* asymmetry corresponds to a pure sample of top-quark pairs. However, there are no corrections for detector effects.
- The *extrapolated* or *fully-corrected* asymmetry is corrected to production level.

5.1.5 Validation

The efficacy of the correction procedure is tested for each of the benchmark models using 10 000 simulated experiments. Each is generated with the $t\bar{t}$ event yield as in the data. In each experiment, the number of events in each qy_ℓ bin is fluctuated according to Poisson statistics, and the acceptance correction and extrapolation procedure is

Table 5.3. True asymmetries as generated in simulation compared to mean extrapolated results for 10 000 simulated experiments with the yield of the $t\bar{t}$ component as in the data. Uncertainties are negligible.

Signal model	True A_{FB}^ℓ	Extrapolated A_{FB}^ℓ
NLO QCD (POWHEG)	+0.024	+0.026
LO SM (ALPGEN)	+0.003	-0.004
Octet A	+0.070	+0.070
Octet L	-0.062	-0.062
Octet R	+0.149	+0.155

performed to yield a corrected asymmetry that is compared to the known production-level value.

The mean values of the asymmetries in the 10 000 simulated experiments for each model are shown in Table 5.3. The extrapolation procedure is successful at recovering the true asymmetry while introducing only minimal model-dependent biases: absolute deviations of the mean extrapolated result from the true asymmetry are below 0.01. Note, in particular, that the procedure yields the vanishing asymmetry in the LO standard model, and that biases with the NLO standard model and Octet A (which has an A_{FB}^ℓ value similar to that observed in the data) are very small.

5.2 Expected Value of A_{FB}^ℓ

In light of the correlation between A_{FB}^ℓ and $A_{\text{FB}}^{\Delta y}$, it is desirable to have some expectation for A_{FB}^ℓ given the measured value of $A_{\text{FB}}^{\Delta y}$. In general the relationship is model-dependent. However, in the case where the only substantial deviation from the SM predictions is $A_{\text{FB}}^{\Delta y}$, with no polarization and top-quark decays as described by the SM, an estimate is straightforward. This includes the cases of either the unpolarized axigluon model discussed previously or purely-Standard-Model proposals in which unexpectedly large QCD corrections result in an enhanced $A_{\text{FB}}^{\Delta y}$.

One estimate is provided by Octet A, with a top-quark asymmetry of 0.156, which

compares well to the CDF measurement of 0.164 ± 0.047 [35]. Octet A predicts no top-quark polarization, so A_{FB}^ℓ is entirely due to the kinematic correlation with Δy . The predicted asymmetry of Octet A, $A_{\text{FB}}^\ell = 0.070$, therefore provides a possible expectation for the data.

A second estimate is derived from the predicted ratio $A_{\text{FB}}^\ell/A_{\text{FB}}^{\Delta y}$ in conjunction with the observed value of $A_{\text{FB}}^{\Delta y}$. When the top quark is unpolarized and decays as the SM top quark, this ratio is fixed. It may be derived from several sources to confirm the sensibility of this procedure. The ratio from POWHEG is 0.46. The calculation of Ref. [32], yields a ratio of 0.43. Octet A, which has much larger asymmetries than either of these, has a ratio of 0.45. The similarity of these values suggests that a simple ratio is sufficient to capture the kinematic correlation between the two asymmetries. Given the value $A_{\text{FB}}^{\Delta y} = 0.164$ measured by CDF, the expected asymmetry of the lepton calculated with the POWHEG ratio is 0.076. The concordance of Octet A and ratio-based estimates suggests that a reasonable expectation for A_{FB}^ℓ , given no top-quark polarization and the value of $A_{\text{FB}}^{\Delta y}$ measured by CDF, is in the range of 0.070–0.076.

5.3 Measurement of A_{FB}^ℓ

5.3.1 Central Value

We next examine the data during each stage of the analysis as outlined in Sec. 5.1.4. Unless otherwise noted, reported errors include both the statistical uncertainty as well as the systematic uncertainties appropriate to that correction level.

The observed event distribution of qy_ℓ is shown in Figure 5.4a. The inclusive asymmetry observed in the data is 0.067 ± 0.016 , compared to the predicted value of 0.031 from POWHEG and backgrounds. Figure 5.4b shows the distribution of qy_ℓ after backgrounds are subtracted. The inclusive asymmetry is 0.070 ± 0.022 .

The background-subtracted qy_ℓ distribution is next decomposed into the corresponding $S(qy_\ell)$ (Fig. 5.4c) and $A_{\text{FB}}^\ell(qy_\ell)$ (Fig. 5.4d) parts. The distribution of $S(qy_\ell)$ is in good agreement with the POWHEG expectation. The root-mean-square of $S(qy_\ell)$ is 0.580 ± 0.008 , in excellent agreement with the predicted value from POWHEG of 0.581. As per Section 5.1.3, this suggests that the simulated $\mathcal{S}(qy_\ell)$ should be reliable over the full range of qy_ℓ .

The measured $A_{\text{FB}}^\ell(qy_\ell)$ exceeds the predicted value in most bins, but becomes negative near $|qy_\ell| = 0$. As the distribution of qy_ℓ is expected to be continuous, its asymmetric part $\mathcal{A}(qy_\ell)$ must necessarily vanish as $qy_\ell \rightarrow 0$. The finite width of the bin adjacent to $|qy_\ell| = 0$ allows it to have a nonzero value, but this value is generally small in comparison to the inclusive asymmetry. Consequentially, the observed deviation from this behavior is most likely statistical in nature.

Acceptance corrections are then applied to the background-subtracted $A_{\text{FB}}^\ell(qy_\ell)$ value, and the result is fit to Eq. (5.11). The acceptance-corrected data, POWHEG prediction, and fits to both are shown in Figure 5.5. The estimated value of a in the data is 0.266 ± 0.068 (stat.). After performing the integration, the resulting inclusive asymmetry in the data is $A_{\text{FB}}^\ell = 0.094 \pm 0.024$. This uncertainty is statistical only and is taken from the variance of the POWHEG pseudoexperiments of Sec. 5.1.5.

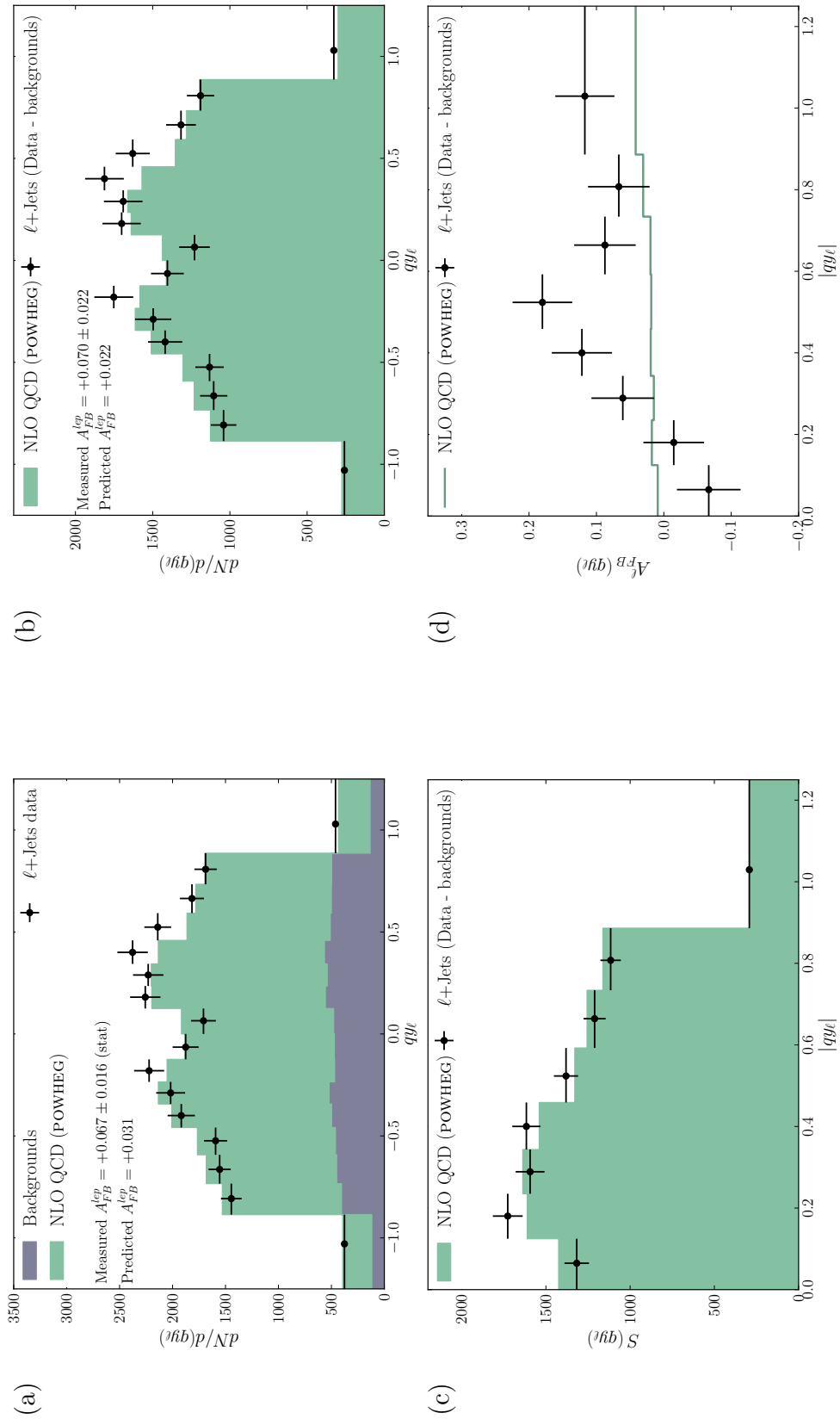


Figure 5.4. Several key distributions in the signal region. Figure (a) shows the distribution of qy_ℓ in the measured data. Figure (b) shows the same distribution after subtracting the most probable background contribution in each bin. Figure (c) and (d) show the symmetry part $S(qy_\ell)$ and the qy_ℓ -dependent asymmetry $A_{FB}^{\ell}(qy_\ell)$ after background-subtraction.

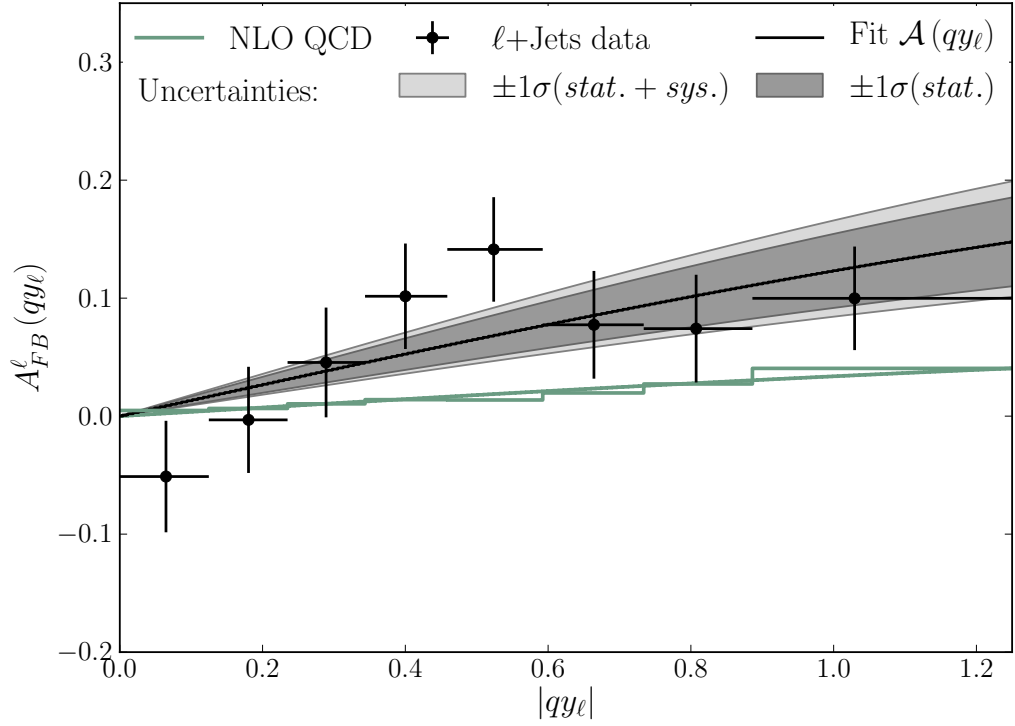


Figure 5.5. The binned asymmetry $A_{\text{FB}}^{\ell}(qy_{\ell})$ after correcting for acceptance, compared to the NLO QCD prediction of POWHEG. The best fit to Eq. (5.11) for each is shown as the smooth curve of the same color. The dark (light) gray bands indicate the statistical (total) uncertainty on the fit curve to the data.

5.3.2 Uncertainties

5.3.2.1 Backgrounds

The largest systematic uncertainty is associated with the background subtraction, where it is assumed that each background component has precisely the normalization reported in Table 4.4 and the statistically asymptotic shape of its prediction. The effects of uncertain normalizations and finite bin population are accommodated by extending the pseudoexperiment technique of Sec. 5.1.5.

For each simulated experiment, a normalization for each signal and background component is randomly generated from a Gaussian distribution, using the expected yield and uncertainty. Then the population of each bin of each normalized component

is randomly varied according to Poisson statistics. The randomized components are then summed. A set of 10 000 simulated experiments is generated using POWHEG as the signal model and subject to the entirety of the correction procedure. This simultaneously incorporates the effects of statistical fluctuations on the bin populations and background shapes as well as the uncertainties on the expected background normalizations.

5.3.2.2 Recoil Modelling

Another large uncertainty stems from the modeling of the $t\bar{t}$ recoil from QCD radiation. The presence of radiated jets is strongly correlated with both $A_{\text{FB}}^{\Delta y}$ and the p_T of the $t\bar{t}$ system, as discussed in Section 1.3. The resulting larger average $p_T^{\bar{t}}$ of backward events promotes them into the signal region with greater probability, inducing a small backward-favoring asymmetry in the acceptance of the lepton.

An uncertainty due to the modeling of this effect is assessed by comparing the result using the nominal POWHEG acceptance model to other models. The harder recoil spectra of PYTHIA and ALPGEN showered with PYTHIA results in larger acceptance corrections, increasing A_{FB}^{ℓ} by up to 0.013. This is included as a one-sided systematic uncertainty to reflect the fact that models other than POWHEG are likely to increase the measured value of the asymmetry.

5.3.2.3 Signal Model

Most uncertainties on the signal model, including the above recoil-modeling uncertainty, enter only through the bin-by-bin acceptance corrections. This class of uncertainties is quantified by performing the correction procedure on the data using acceptances from alternate simulated $t\bar{t}$ samples. Uncertainties are assessed from the effects of varying the color reconnection model, parton showering algorithm, and jet-energy-scale (JES) calibration. All of these are small, as expected since jets are used

Table 5.4. Uncertainties on the fully-extrapolated measurement.

Source of uncertainty	Value
Backgrounds	0.015
Recoil modeling	+0.013 −0.000
Color reconnection	0.0067
Parton showering	0.0027
Parton distribution functions	0.0025
Jet-energy scales	0.0022
Initial and final state radiation	0.0018
Total systematic	+0.022 −0.017
Data sample size	0.024
Total uncertainty	+0.032 −0.029

only to define the signal region. Uncertainties on the PDFs also have minimal impact.

An additional recoil-related bias may arise from the initial-and final- state radiation model (IFSR) of the PYTHIA showering of POWHEG. This is tested by evaluating the effect of reasonable variations in the amount of IFSR. The effect is also very small. Table 5.4 summarizes all of the uncertainties considered. The largest uncertainty is due to the limited sample size. Combining the systematic uncertainties in quadrature, the final result is $A_{\text{FB}}^{\ell} = 0.094 \pm 0.024^{+0.022}_{-0.017}$.

5.3.3 Consistency Checks

To further check the validity of the inclusive measurement of A_{FB}^{ℓ} , the sample is divided into several subsamples which are expected to have the same inclusive asymmetries, summarized in Table 5.5. Additional distributions for each of these subsamples are reproduced in Appendix A.

Two independent subsamples are formed by partitioning according to lepton flavor. The raw asymmetry for decays into muons is 0.081 ± 0.022 while that for decays into electrons is 0.050 ± 0.024 . The difference is consistent with zero at about the 1σ

Table 5.5. Table summarizing the resulting asymmetries when the sample is divided by either charge or lepton type. Also included is the inclusive result.

Sample	Yield	Raw	Background-subtracted	Fully extrapolated
Electrons	1788	0.050 ± 0.024	0.050 ± 0.033	$0.062^{+0.052}_{-0.049}$
Muons	2076	0.081 ± 0.022	0.087 ± 0.029	$0.119^{+0.039}_{-0.037}$
Positive	1884	0.099 ± 0.023	0.110 ± 0.031	$0.125^{+0.043}_{-0.041}$
Negative	1980	0.036 ± 0.022	0.034 ± 0.031	$0.063^{+0.046}_{-0.042}$
$W+4$	2682	0.064 ± 0.019	0.064 ± 0.024	$0.084^{+0.035}_{-0.032}$
$W+3+1$	1182	0.072 ± 0.029	0.092 ± 0.049	$0.115^{+0.067}_{-0.065}$
Inclusive	3864	0.067 ± 0.016	0.070 ± 0.022	$0.094^{+0.032}_{-0.029}$

level. This difference is carried through each stage of correction with similar levels of significance at each, resulting finally in fully-corrected asymmetries of $0.119^{+0.039}_{-0.037}$ in events with a muon and $0.062^{+0.052}_{-0.049}$ in events with an electron (Figures A.5c and A.5d).

The sample is also partitioned according to lepton charge. The difference between the raw asymmetries of the two subsamples is nonzero at 2σ . A similar difference is observed in the background-subtracted asymmetries. This difference is due to negative-asymmetry bins in the negatively-charged leptons near $|qy_\ell| = 0$ (Figure A.2d). As in the inclusive case, this is most likely a statistical fluctuation. The fit, which by construction has $\mathcal{A}(0) = 0$, is insensitive to these bins. This moderates the discrepancy in the extrapolated result to 1σ after the extrapolation procedure is performed (Figures A.5a and A.5b).

Finally, the sample is partitioned according to the E_T of the fourth jet. The $W+4$ sub-sample consists of events having a fourth jet with > 20 GeV. The fully-corrected asymmetry is $0.084^{+0.035}_{-0.032}$. The conjugate subsample, $W+3+1$, is comprised of events with a fourth jet that has transverse energy $20 \text{ GeV} \gg 12 \text{ GeV}$. The fully corrected asymmetry is $0.115^{+0.067}_{-0.065}$, consistent with the measurement in the $W+4$ subsample.

CHAPTER VI

Conclusions

The distribution of the charge-weighted lepton rapidity in semileptonic top quark decays contains information on both the top-quark production asymmetry and the top-quark polarization. A technique is developed to correct for acceptances and extrapolate to unmeasured rapidity regions. This technique is applied to a sample of 3864 top-quark pair candidates recorded with the CDF-II detector at the Fermilab Tevatron. The production-level lepton asymmetry is found to be $A_{\text{FB}}^{\ell} = 0.094_{-0.029}^{+0.032}$.

This result is to be compared with the predicted value of 0.038 ± 0.003 [32], which includes both electroweak and NLO QCD effects. That calculation uses the LO $t\bar{t}$ production cross-section in the denominator of the asymmetry; using the NLO cross-section reduces the predicted asymmetry by $\sim 30\%$. Assuming a Δy asymmetry as indicated by the CDF measurement of 0.164 ± 0.047 [35], and that the top quarks are unpolarized (as in the Standard Model), the expected lepton asymmetry is estimated to lie in the range 0.070–0.076.



Figure 6.1. The chapter headpiece.

APPENDICES

APPENDIX A

Cross-Checks of the Inclusive Lepton Asymmetry

This appendix displays several cross-check distributions, obtained by dividing the signal region into two pairs of mutually-exclusive subsamples. First, the sample is divided into events with a positive lepton (Fig. A.1) and events with a negative lepton (Fig. A.2). The sample is then divided into events with an identified electron (Fig. A.3) and events with an identified muon only (Fig. A.4). The functional fits in these four subsamples are compared in Figure A.5.

Additionally, the data is divided into events with four tight jets (Fig. A.6) and events with three tight jets and one loose jet (Fig. A.7). The functional fit in these two subsamples are compared in Figure A.8.

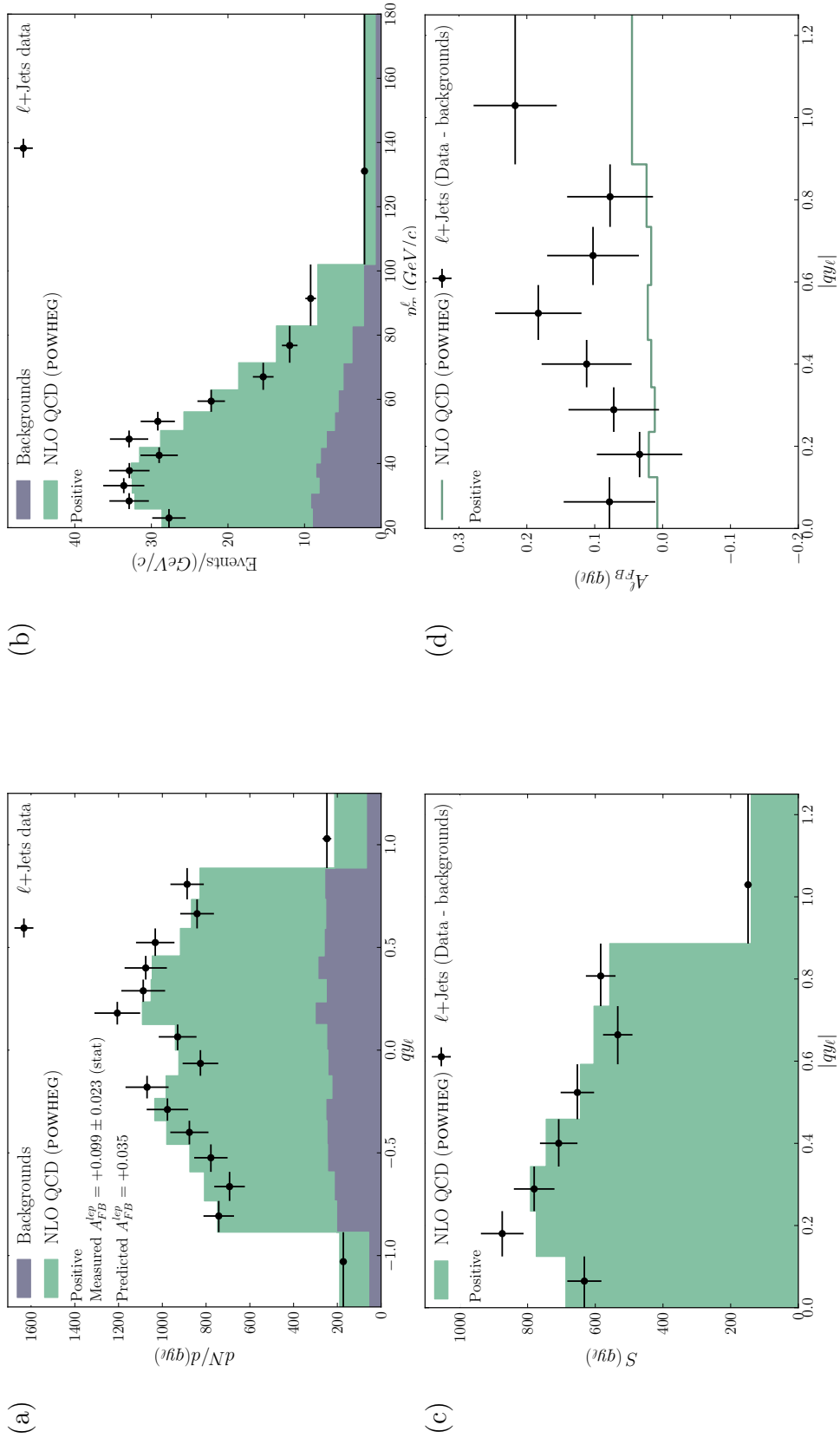


Figure A.1. Several key distributions, reproduced using only events that contain a positive lepton. Shown are qy_ℓ (a) and p_T^ℓ (b) before background subtraction, along with $S(qy_\ell)$ (c) and $A_{FB}^\ell(qy_\ell)$ (d) after background-subtraction.

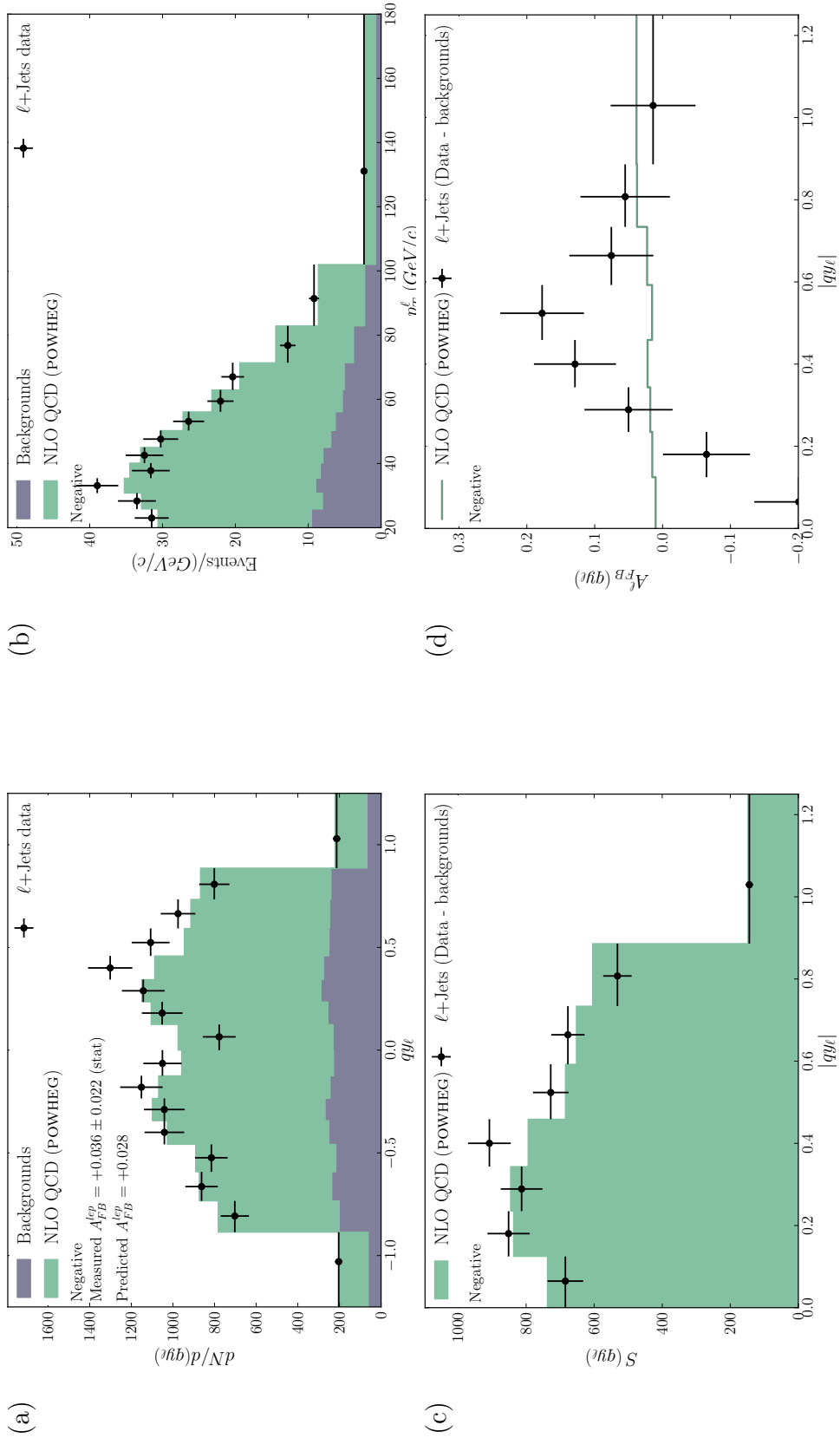


Figure A.2. Several key distributions, reproduced using only events that contain a negative lepton. Shown are qy_ℓ (a) and p_T^ℓ (b) before background subtraction, along with $S(qy_\ell)$ (c) and $A_{FB}^{\ell}(qy_\ell)$ (d) after background-subtraction.

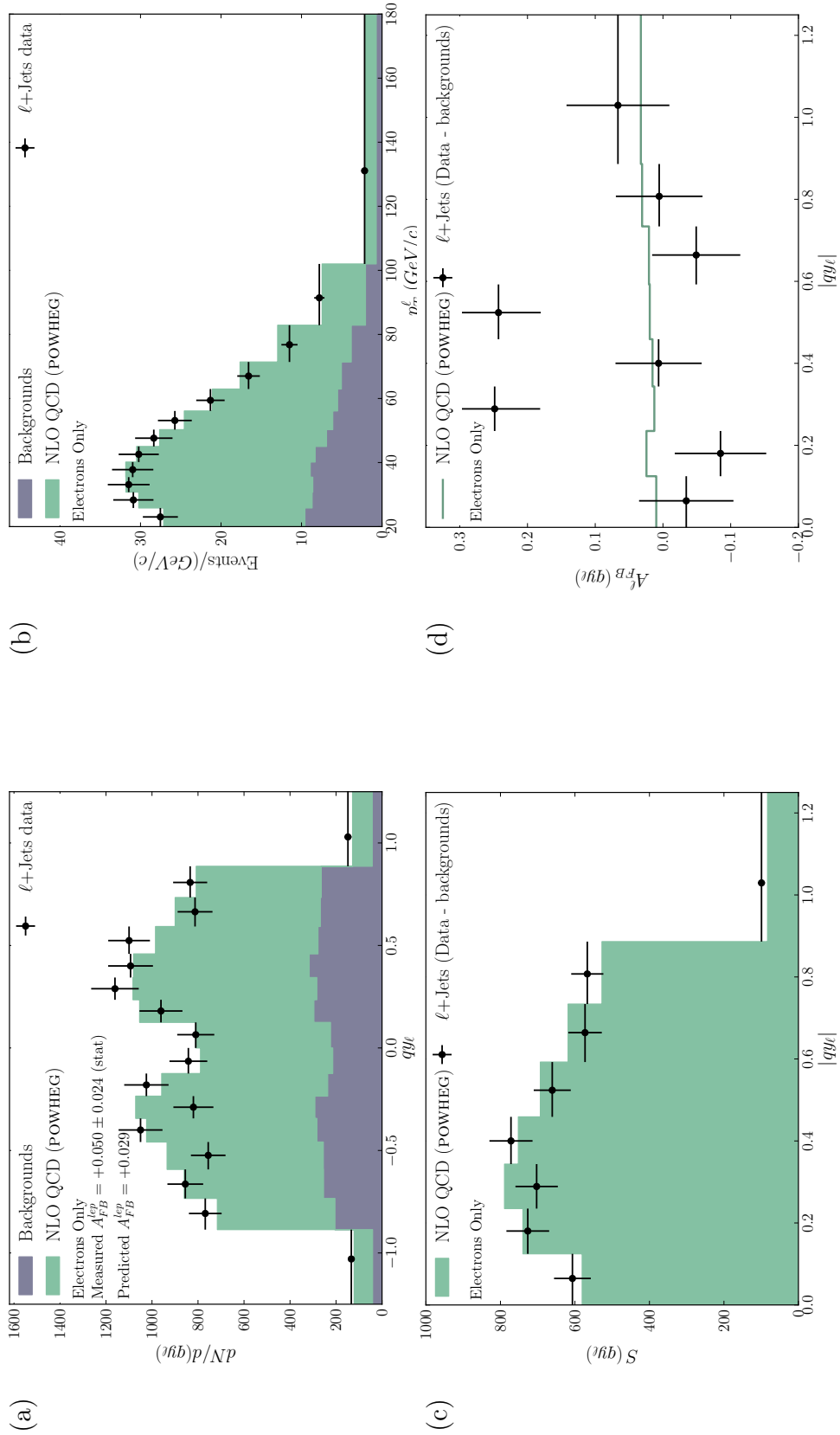


Figure A.3. Several key distributions, reproduced using only events that contain an electron. Shown are qy_ℓ (a) and p_T^ℓ (b) before background subtraction, along with $S(qy_\ell)$ (c) and $A_{FB}^\ell(qy_\ell)$ (d) after background-subtraction.

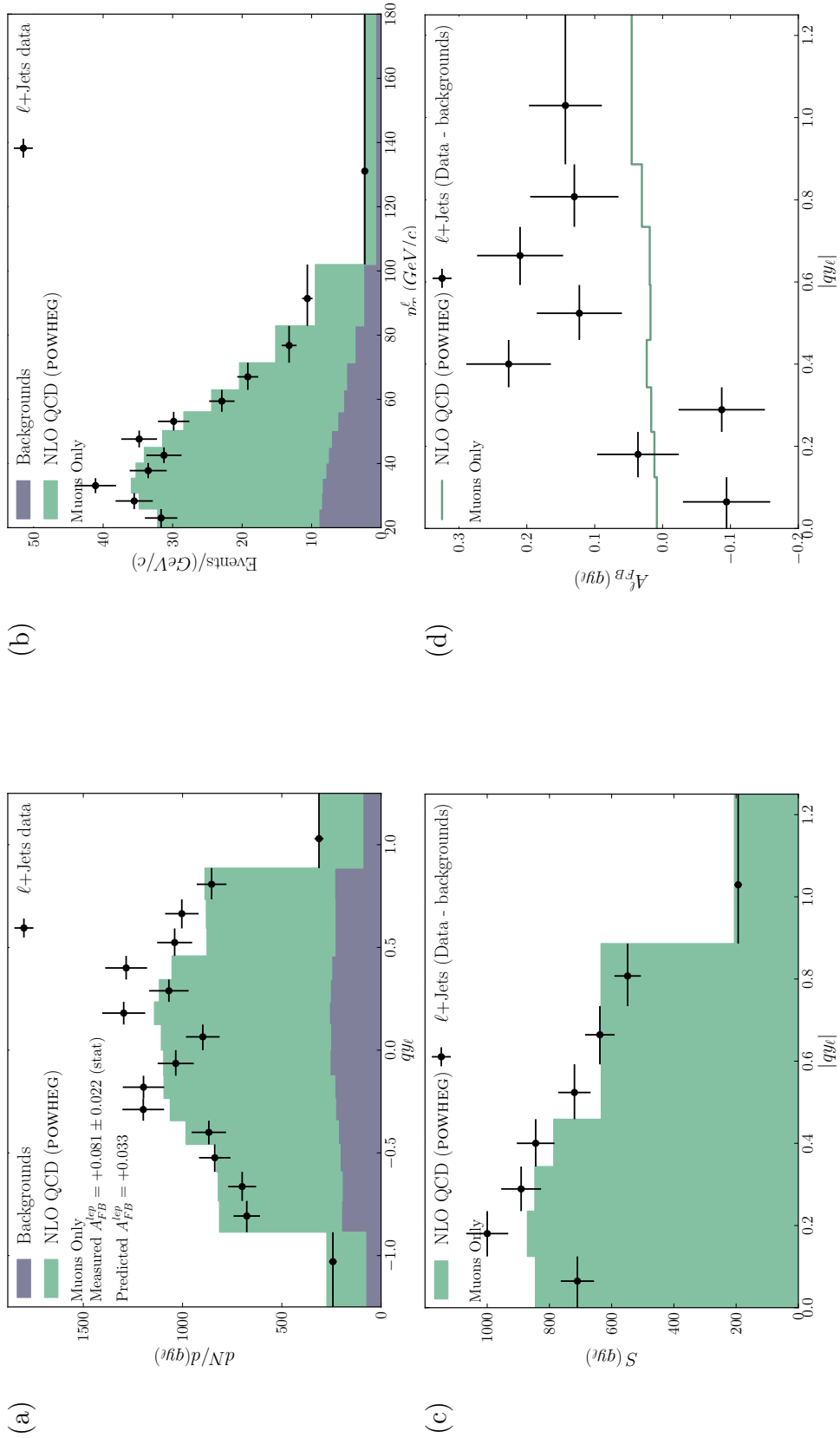


Figure A.4. Several key distributions, reproduced using only events that contain a muon. Shown are $qq\bar{\ell}$ (a) and p_{T}^{ℓ} (b) before background subtraction, along with $S(qq\bar{\ell})$ (c) and $A_{FB}^{\ell}(qq\bar{\ell})$ (d) after background-subtraction.

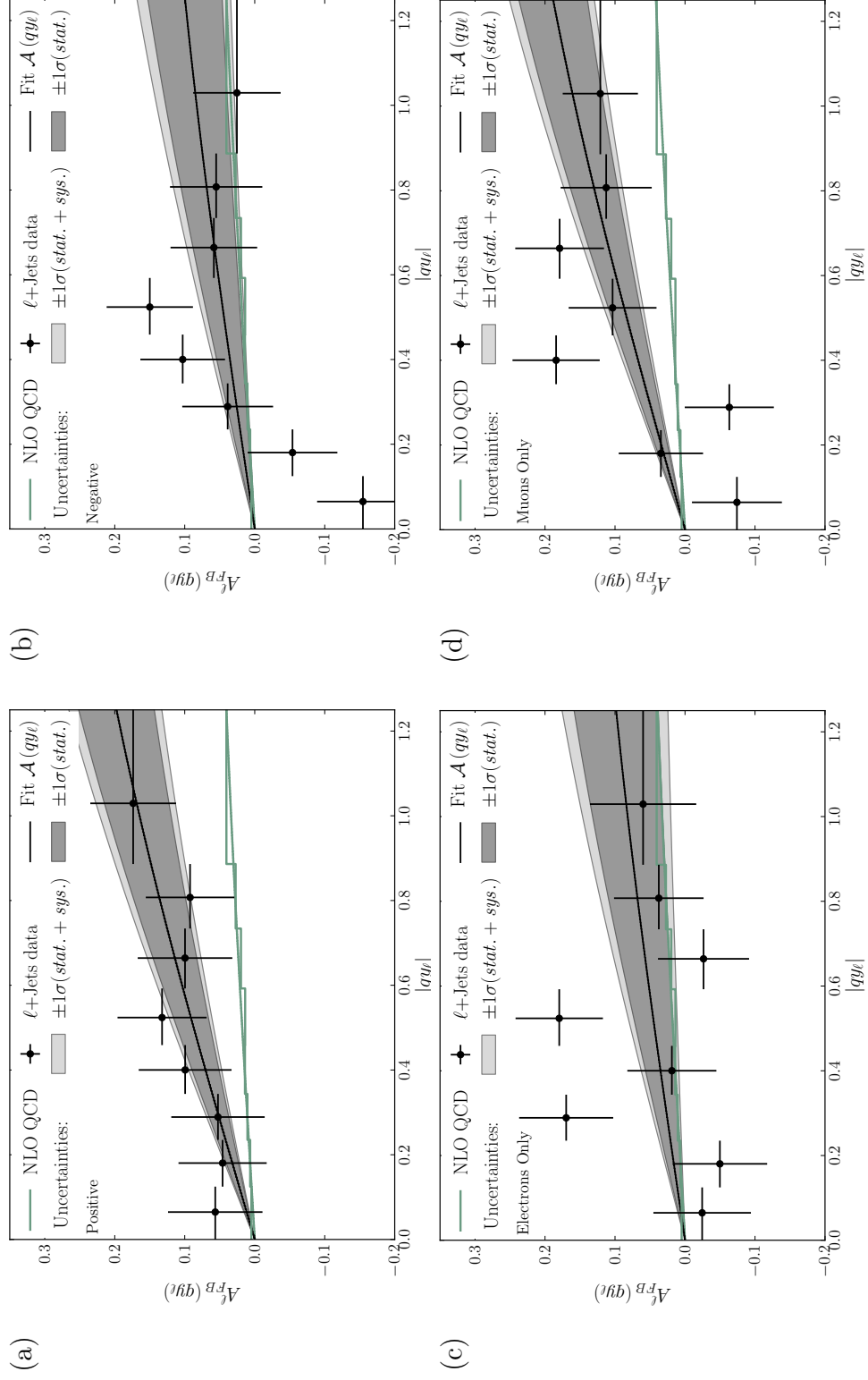


Figure A.5. A comparison of the acceptance-corrected qy_ℓ fits between several subsamples of the signal region. Figures (a) and (b) show the fit for events with positive and negative leptons, respectively. Figures (c) and (d) show the fit for events with an electron and for events with a muon.

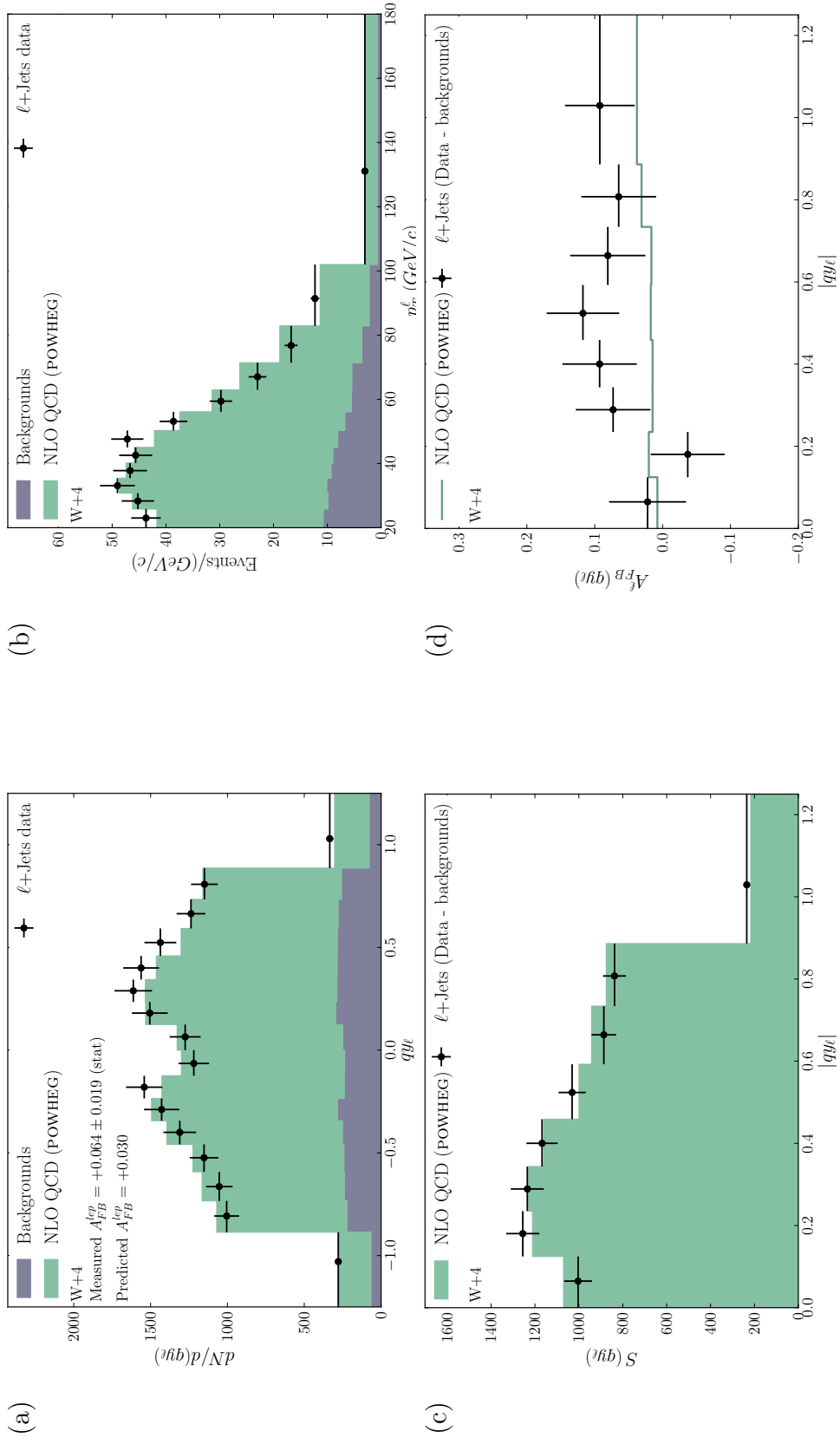


Figure A.6. Several key distributions, reproduced using only events that contain four or more tight jets. Shown are qy_ℓ (a) and p_T^ℓ (b) before background subtraction, along with $S(qy_\ell)$ (c) and $A_{FB}^{\ell}(qy_\ell)$ (d) after background-subtraction.

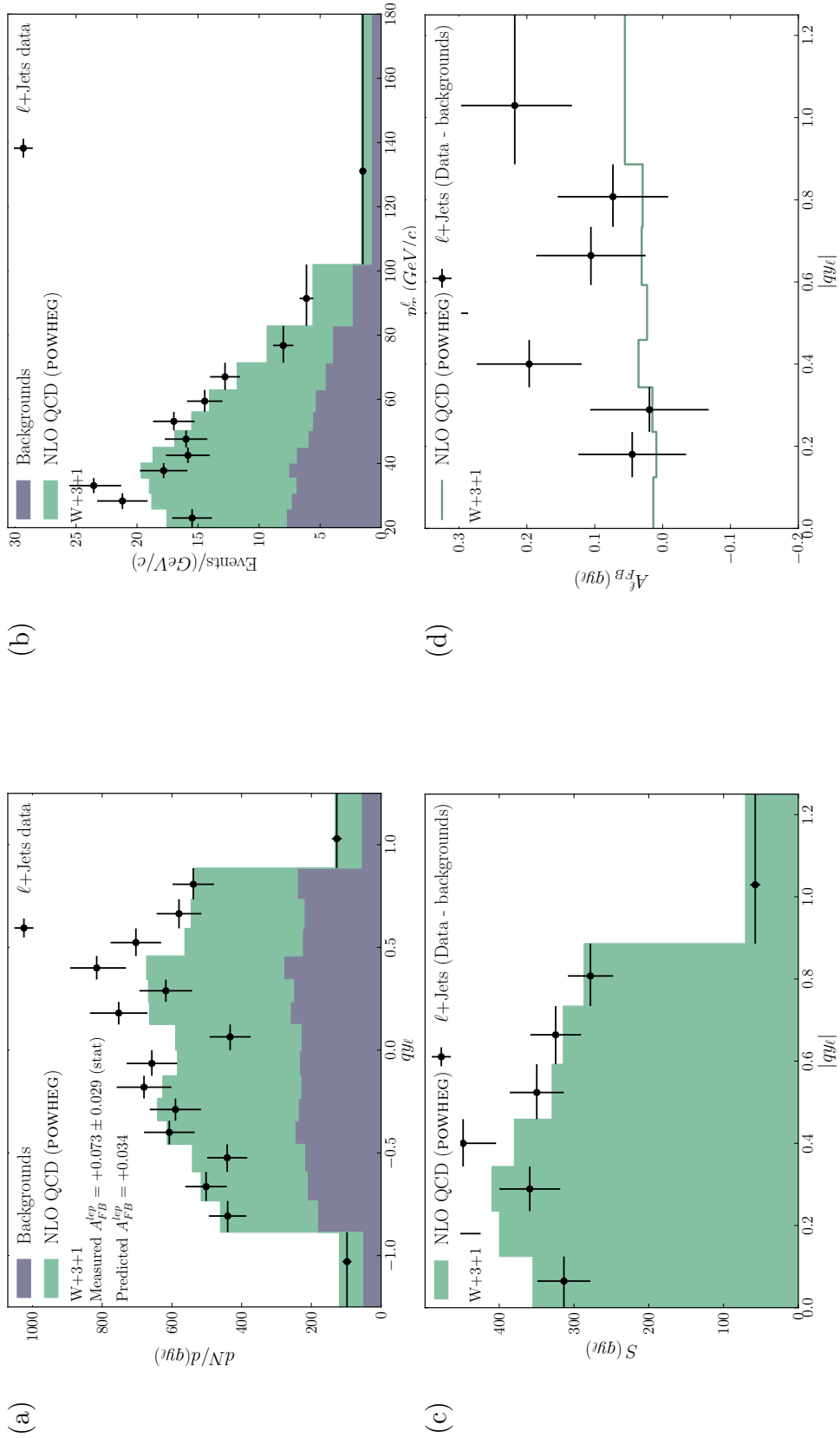


Figure A.7. Several key distributions, reproduced using only events that contain exactly three tight jets and one loose jet. Shown are qy_ℓ (a) and p_T^ℓ (b) before background subtraction, along with $S(qy_\ell)$ (c) and $A_{FB}^\ell(qy_\ell)$ (d) after background-subtraction.

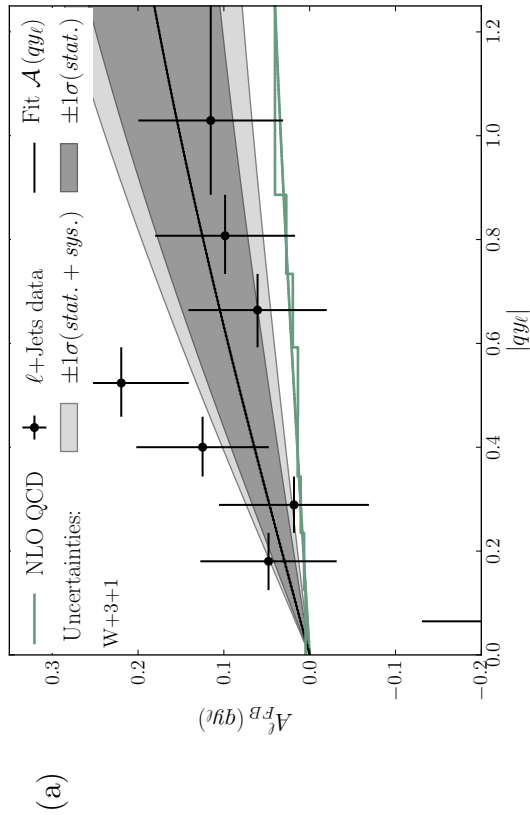
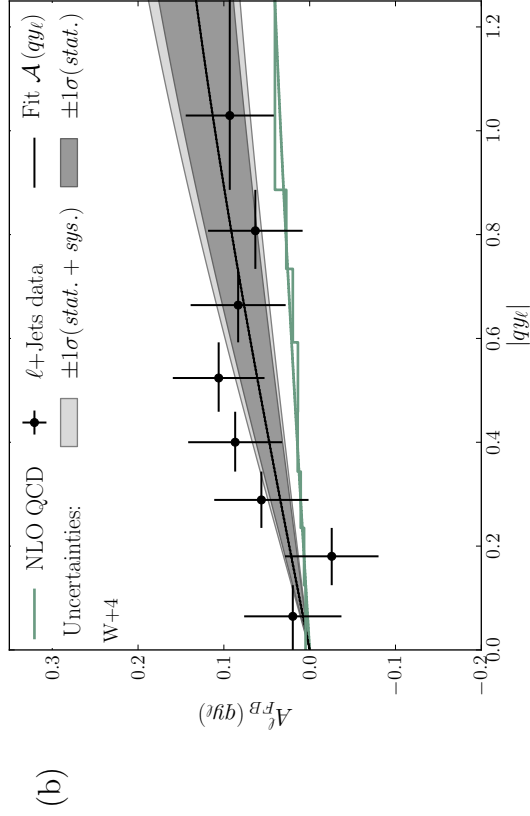


Figure A.8. A comparison of the acceptance-corrected $qy\ell$ fits between events with four or more tight jets (b) and events with exactly three tight jets and one loose jet (a).

APPENDIX B

Bin Contents and Binned Asymmetries in the Signal Region

This appendix reproduces several important values associated with each bin in the signal region. Tables B.1 and B.2 show the measured population of each bin before and after the nominal background contribution has been subtracted. Tables B.3 and B.4 enumerate the symmetric part $S(qy_\ell)$ and binned asymmetry $A_{\text{FB}}^\ell(qy_\ell)$, both after backgrounds have been subtracted.

Table B.1. The measured population of the CDF-II data in each bin in qy_ℓ , compared to the prediction of POWHEG and the nominal background model.

CDF Run II Preliminary $\int \mathcal{L} = 9.4/\text{fb}$		
qy_ℓ	CDF ℓ +Jets Data	POWHEG + Backgrounds
$[-1.50, -0.89)$	231	241.57
$[-0.89, -0.73)$	220	232.97
$[-0.73, -0.59)$	220	237.84
$[-0.59, -0.46)$	213	235.98
$[-0.46, -0.34)$	221	231.39
$[-0.34, -0.24)$	219	231.62
$[-0.24, -0.12)$	245	226.30
$[-0.12, +0.00)$	234	234.86
$[+0.00, +0.12)$	213	238.97
$[+0.12, +0.24)$	249	242.23
$[+0.24, +0.34)$	242	238.83
$[+0.34, +0.46)$	274	246.01
$[+0.46, +0.59)$	286	249.13
$[+0.59, +0.73)$	257	251.94
$[+0.73, +0.89)$	257	258.13
$[+0.89, +1.50]$	283	266.23

Table B.2. The population of each bin in qy_ℓ after the nominal background prediction has been subtracted from the CDF-II data.

CDF Run II Preliminary $\int \mathcal{L} = 9.4/\text{fb}$		
qy_ℓ	CDF ℓ +Jets (Data - Backgrounds)	POWHEG
$[-1.50, -0.89)$	158.6	169.13
$[-0.89, -0.73)$	158.5	171.48
$[-0.73, -0.59)$	156.3	174.16
$[-0.59, -0.46)$	151.3	174.28
$[-0.46, -0.34)$	163.6	173.99
$[-0.34, -0.24)$	162.4	175.06
$[-0.24, -0.12)$	193.2	174.52
$[-0.12, +0.00)$	175.2	176.05
$[+0.00, +0.12)$	153.3	179.26
$[+0.12, +0.24)$	187.6	180.84
$[+0.24, +0.34)$	183.5	180.33
$[+0.34, +0.46)$	208.9	180.89
$[+0.46, +0.59)$	217.8	180.91
$[+0.59, +0.73)$	186.3	181.20
$[+0.73, +0.89)$	181.2	182.32
$[+0.89, +1.50]$	200.7	183.88

Table B.3. The symmetric part $S(qy_\ell)$ of the background-subtracted CDF-II data, compared to the prediction of POWHEG.

CDF Run II Preliminary $\int \mathcal{L} = 9.4/\text{fb}$		
$ qy_\ell $	CDF ℓ +Jets (Data - Backgrounds)	POWHEG
[+0.00, +0.12)	164.2	177.65
[+0.12, +0.24)	190.4	177.68
[+0.24, +0.34)	173.0	177.69
[+0.34, +0.46)	186.2	177.44
[+0.46, +0.59)	184.5	177.59
[+0.59, +0.73)	171.3	177.68
[+0.73, +0.89)	169.8	176.90
[+0.89, +1.50]	179.6	176.50

Table B.4. The binned asymmetry $A_{\text{FB}}^\ell(qy_\ell)$ of the background-subtracted CDF-II data, compared to the prediction of POWHEG.

CDF Run II Preliminary $\int \mathcal{L} = 9.4/\text{fb}$		
$ qy_\ell $	CDF ℓ +Jets (Data - Backgrounds)	POWHEG
[+0.00, +0.12)	-0.067 ± 0.047	+0.009
[+0.12, +0.24)	-0.015 ± 0.045	+0.018
[+0.24, +0.34)	$+0.061 \pm 0.047$	+0.015
[+0.34, +0.46)	$+0.122 \pm 0.045$	+0.019
[+0.46, +0.59)	$+0.180 \pm 0.044$	+0.019
[+0.59, +0.73)	$+0.087 \pm 0.046$	+0.020
[+0.73, +0.89)	$+0.067 \pm 0.046$	+0.031
[+0.89, +1.50]	$+0.117 \pm 0.044$	+0.042

REFERENCES

REFERENCES

- [1] “Wikimedia commons,” http://commons.wikipedia.org/wiki/File:Standard_Model_of_Elementary_Particles.svg.
- [2] “Wikimedia commons,” http://commons.wikimedia.org/wiki/File:Elementary_particle_interactions_in_the_Standard_Model.png.svg.
- [3] “Wikipedia,” http://upload.wikimedia.org/wikipedia/en/4/4b/Weak_Decay_flipped.svg.
- [4] “Summary plots from the atlas top physics group,” <https://atlas.web.cern.ch/Atlas/GROUPS/PHYSICS/CombinedSummaryPlots/TOP/>.
- [5] P. Z. Skands, B. R. Webber, and J. Winter, *J. High Energy Phys.* **07** (2012) 151.
- [6] “Concepts rookie book,” (2010), http://www-bdnew.fnal.gov/operations/rookie_books/concepts.pdf.
- [7] P. T. Lukens *et al.* (CDF Collaboration), “The CDF IIB Detector Technical Design Report,” (2003).
- [8] R. Blair *et al.* (CDF Collaboration), “The CDF-II Detector: Technical Design Report,” (1996).
- [9] T. Aaltonen *et al.* (CDF Collaboration), *Nucl. Instrum. Meth. A* **729**, 153 (2013).
- [10] G. Pauletta (CDF Collaboration), *J. Phys. Conf. Ser.* **160**, 012007 (2009).
- [11] “CDF Run II Level-3 Specifications,” (2004), http://www-cdf.fnal.gov/upgrades/daq_trig/trigger.html.
- [12] “The CDF Experiment,” (2014), <http://www-cdf.fnal.gov/>.
- [13] A. Bhatti *et al.* (CDF Collaboration), *Nucl. Instrum. Meth. A* **566**, 375 (2006).
- [14] J. Beringer *et al.* (Particle Data Group), *Phys. Rev. D* **86**, 010001 (2012).
- [15] T. Stelzer and S. Willenbrock, *Phys. Lett. B* **374**, 169 (1996).
- [16] G. Mahlon and S. J. Parke, *Phys. Rev. D* **53**, 4886 (1996).

- [17] A. Abulencia *et al.* (CDF Collaboration), J. Phys. **G34**, 2457 (2007).
- [18] D. Acosta *et al.* (CDF Collaboration), Phys. Rev. D **71**, 052003 (2005).
- [19] J. Adelman, S. Budd, D. P., R. Erbacher, S. Grinstein, D. Hare, K. Lannon, E. Palencia, C. Plager, J. Slaunwhite, D. Sherman, T. Schwarz, V. Sorin, and B. Stelzer (CDF Collaboration), “Method II For You,” CDF Internal Note 9185 (unpublished) (2008).
- [20] M. Czakon, P. Fiedler, and A. Mitov, Phys. Rev. Lett. **110**, 252004 (2013).
- [21] T. A. Aaltonen *et al.* (CDF Collaboration, D0 Collaboration), Phys. Rev. D **89**, 072001 (2014).
- [22] M. Muether and CDF (Tevatron Electroweak Working Group, CDF Collaboration, D0 Collaboration), (2013), arXiv:1305.3929 [hep-ex] .
- [23] S. Chatrchyan *et al.* (CMS Collaboration), “Combination of ATLAS and CMS results on the mass of the top quark using up to 4.9 inverse femtobarns of data,” (2013).
- [24] M. Jezabek and J. H. Kuhn, Nucl. Phys. B **314**, 1 (1989).
- [25] T. A. Aaltonen *et al.* (CDF Collaboration), Phys. Rev. Lett. **111**, 202001 (2013).
- [26] V. M. Abazov *et al.* (D0 Collaboration), Phys. Rev. D **85**, 091104 (2012).
- [27] “Measurement of $t\bar{t}$ Helicity Fractions and Spin Correlation Using Reconstructed Lepton+Jets Events,” CDF Public Note 10211 (unpublished) (2010).
- [28] “Measurement of $t\bar{t}$ Spin Correlation Coefficients in $5.1fb^{-1}$ in Dilepton Candidates,” CDF Public Note 10719 (unpublished) (2011).
- [29] V. M. Abazov *et al.* (D0 Collaboration), Phys. Rev. Lett. **108**, 032004 (2012).
- [30] G. Aad *et al.* (ATLAS Collaboration), Phys. Rev. Lett. **108**, 212001 (2012).
- [31] S. Chatrchyan *et al.* (CMS Collaboration), Phys. Rev. Lett. **112**, 182001 (2014).
- [32] W. Bernreuther and Z.-G. Si, Phys. Rev. D **86**, 034026 (2012).
- [33] J. Winter, P. Z. Skands, and B. R. Webber, EPJ Web Conf. **49**, 17001 (2013).
- [34] V. M. Abazov *et al.* (D0 Collaboration), Phys. Rev. D **84**, 112005 (2011).
- [35] T. Aaltonen *et al.* (CDF Collaboration), Phys. Rev. D **87**, 092002 (2013).
- [36] T. Aaltonen *et al.* (CDF Collaboration), Phys. Rev. D **83**, 112003 (2011).
- [37] X.-D. Guo, Y.-J. Zhang, S.-M. Zhao, T.-F. Feng, X.-H. Yuan, *et al.*, (2013), arXiv:1309.5419 [hep-ph] .

- [38] A. Kumar, J. N. Ng, A. Spray, and P. T. Winslow, Phys. Rev. D **88**, 075012 (2013).
- [39] S. Jung, H. Murayama, A. Pierce, and J. D. Wells, Phys. Rev. D **81**, 015004 (2010).
- [40] K. Cheung, W.-Y. Keung, and T.-C. Yuan, Phys. Lett. B **682**, 287 (2009).
- [41] A. E. Nelson, T. Okui, and T. S. Roy, Phys. Rev. D **84**, 094007 (2011).
- [42] J. Shu, T. M. P. Tait, and K. Wang, Phys. Rev. D **81**, 034012 (2010).
- [43] J. Aguilar-Saavedra and M. Perez-Victoria, J. High Energy Phys. 1109 (2011) 097.
- [44] E. Álvarez and E. C. Leskow, Phys. Rev. D **86**, 114034 (2012).
- [45] J. Shelton and K. M. Zurek, Phys. Rev. D **83**, 091701 (2011).
- [46] M. Duraisamy, A. Rashed, and A. Datta, Phys. Rev. D **84**, 054018 (2011).
- [47] G. M. Tavares and M. Schmaltz, Phys. Rev. D **84**, 054008 (2011).
- [48] S. Jung, A. Pierce, and J. D. Wells, Phys. Rev. D **84**, 091502 (2011).
- [49] T. Aaltonen *et al.* (CDF Collaboration), Phys. Rev. Lett. **111**, 182002 (2013), arXiv:1306.2357 [hep-ex] .
- [50] Y. Takeuchi *et al.* (CDF Collaboration), “Measurement of the Forward-Backward Asymmetry in Top Pair Production in the Dilepton Decay Channel using 5.1fb^{-1} ,” CDF Internal Note 10436 (unpublished) (2011).
- [51] V. M. Abazov *et al.* (D0 Collaboration), (2014), arXiv:1403.1294 [hep-ex] .
- [52] G. Aad *et al.* (ATLAS Collaboration), J. High Energy Phys. 1402 (2014) 107.
- [53] S. Chatrchyan *et al.* (CMS Collaboration), Phys. Lett. B **717**, 129 (2012).
- [54] J. Aguilar-Saavedra and M. Perez-Victoria, (2011), arXiv:1105.4606 .
- [55] J. Aguilar-Saavedra and A. Juste, Phys. Rev. Lett. **109**, 211804 (2012).
- [56] J. Drobnak, J. F. Kamenik, and J. Zupan, Phys. Rev. D **86**, 054022 (2012).
- [57] J. Drobnak, A. L. Kagan, J. F. Kamenik, G. Perez, and J. Zupan, Phys. Rev. D **86**, 094040 (2012).
- [58] E. L. Berger, Q.-H. Cao, C.-R. Chen, and H. Zhang, (2012), arXiv:1209.4899 [hep-ph] .
- [59] A. Falkowski, M. L. Mangano, A. Martin, G. Perez, and J. Winter, Phys. Rev. D **87**, 034039 (2013).

- [60] E. L. Berger, (2013), arXiv:1301.5053 .
- [61] T. A. Aaltonen *et al.* (CDF Collaboration), Phys. Rev. D **88**, 072003 (2013).
- [62] T. A. Aaltonen *et al.* (CDF Collaboration), (2014), arXiv:1404.3698 [hep-ex] .
- [63] V. M. Abazov *et al.* (D0 Collaboration), Phys. Rev. D **88**, 112002 (2013).
- [64] “Linac rookie book,” (2012, v2.3), http://www-bdnew.fnal.gov/operations/rookie_books/LINAC_RB_v2_3.pdf.
- [65] “Booster rookie book,” (2009, v4.1), http://www-bdnew.fnal.gov/operations/rookie_books/Booster_V4.1.pdf.
- [66] “Main injector rookie book,” (2010, v1.1), http://www-bdnew.fnal.gov/operations/rookie_books/Main_Injector_v1.1.pdf.
- [67] “Antiproton rookie book,” (2011, v2.2), http://www-bdnew.fnal.gov/operations/rookie_books/Pbar_v2.2.pdf.
- [68] “Recycler rookie book,” (2010, v1.42), http://www-bdnew.fnal.gov/operations/rookie_books/Recycler_RB_v1.42.pdf.
- [69] “Tevatron rookie book,” (2009, v2.3), http://www-bdnew.fnal.gov/operations/rookie_books/Tevatron_v2.3.pdf.
- [70] F. Abe *et al.* (CDF Collaboration), Nucl. Instrum. Meth. A **271**, 387 (1988).
- [71] A. A. Affolder *et al.* (CDF Collaboration), Nucl. Instrum. Meth. A **526**, 249 (2004).
- [72] T. Nelson (CDF Collaboration), Int. J. Mod. Phys. **A16S1C**, 1091 (2001).
- [73] T. Akimoto, M. Aoki, P. Azzi, N. Bacchetta, S. Behari, *et al.*, Nucl. Instrum. Meth. A **556**, 459 (2006).
- [74] T. Shaw, C. Nelson, and T. Wesson, IEEE Trans. Nucl. Sci. **47**, 1834 (2000).
- [75] A. Artikov, J. Boudagov, D. Chokheli, G. Drake, M. Gallinaro, *et al.*, (2007), arXiv:0706.3922 [physics.ins-det] .
- [76] K. Byrum *et al.* (CDF Collaboration, CDF Collaboration.), (1994), arXiv:hep-ex/9410004 [hep-ex] .
- [77] S. Bertolucci *et al.* (CDF Collaboration), Nucl. Instrum. Meth. A **267**, 301 (1988).
- [78] D. Cox, (2008), arXiv:0808.0677 [physics.ins-det] .
- [79] J. A. Adelman *et al.* (CDF Collaboration), Nucl. Instrum. Meth. A **572**, 361 (2007).

- [80] A. Bhatti *et al.* (CDF Collaboration), Nucl. Instrum. Meth. A **598**, 331 (2009).
- [81] K. Anikeev, M. Bogdan, R. DeMaat, W. Fedorko, H. J. Frisch, *et al.*, IEEE Trans. Nucl. Sci. **53**, 653 (2006).
- [82] Y. Chung *et al.* (CDF Collaboration), IEEE Trans. Nucl. Sci. **52**, 1212 (2005).
- [83] C. Hayes *et al.* (CDF Collaboration), “Introduction to PadTrack,” CDF Internal Note 6044 (unpublished) (2002).
- [84] C. Hayes *et al.* (CDF Collaboration), “The PAD Track Collection in 5.3,” CDF Internal Note 7304 (unpublished) (2004).
- [85] C. P. Hays, Y. Huang, A. Kotwal, H. Gerberich, S. Menzemer, *et al.*, Nucl. Instrum. Meth. A **538**, 249 (2005).
- [86] J. F. Arguin and B. Heinemann (CDF Collaboration), “Underlying Event Corrections for Run II,” CDF Internal Note 6239 (unpublished) (2003).
- [87] R. Wagner (CDF Collaboration), “Electron Identification for Run II: Algorithms,” CDF Internal Note 5456 (unpublished) (2003).
- [88] R. Wagner (CDF Collaboration), “Electron Identification for Run II: Understanding and Using Lshr,” CDF Internal Note 6249 (unpublished) (2003).
- [89] W. Johnson and T. Junk (CDF Collaboration), “SECVTX Mistag Matrices for 5.6fb^{-1} of Data Up to P28,” CDF Internal Note 10179 (unpublished) (2010).
- [90] J. Freeman (CDF Collaboration), “Summer 2009 SecVtx Mistag Asymmetry Corrections through Period 22,” CDF Internal Note 9847 (unpublished) (2009).
- [91] S. Budd, T. Junk, T. Liss, and C. Neu (CDF Collaboration), “Tight, Loose and Ultratight SECVTX Tag Rate Matrix with 1.2fb^{-1} ,” CDF Internal Note 8519 (unpublished) (2006).
- [92] C. Neu (CDF Collaboration), (2006).
- [93] S. Budd, M. Buhler, C. Ciobanu, P. Dong, T. Junk, J. Luck, S. Richter, B. Stelzer, W. Wagner, and R. Wallny (CDF Collaboration), “Estimation and modeling of non- W background for single-top searches,” CDF Internal Note 8489 (unpublished) (2006).
- [94] S. Frixione, P. Nason, and G. Ridolfi, J. High Energy Phys. 09 (2007) 126.
- [95] M. L. Mangano, M. Moretti, F. Piccinini, R. Pittau, and A. D. Polosa, J. High Energy Phys. 07 (2003) 001.
- [96] J. Alwall, P. Demin, S. de Visscher, R. Frederix, M. Herquet, F. Maltoni, T. Plehn, D. L. Rainwater, and T. Stelzer, J. High Energy Phys. 09 (2007) 028.

- [97] T. Sjostrand, S. Mrenna, and P. Z. Skands, J. High Energy Phys. 05 (2006) 026.
- [98] "Wikipedia entry: Kolmogorov–Smirnov test," http://en.wikipedia.org/wiki/Kolmogorov-Smirnov_test".
- [99] $\mathcal{S}(qy_\ell)$ and $\mathcal{A}(qy_\ell)$ represent the continuous symmetric part and asymmetry. $A_{\text{FB}}^\ell(qy_\ell)$ and $S(qy_\ell)$ are the binned equivalents of these continuous distributions. Simulated samples have very high statistics and may be binned finely enough to be treated as essentially continuous, and so are represented with $\mathcal{A}(qy_\ell)$ and $\mathcal{S}(qy_\ell)$.
- [100] Z. Hong, R. Edgar, S. Henry, D. Toback, J. S. Wilson, and D. Amidei, (2014), arXiv:1403.7565 [hep-ph] .